Photon Assisted Quasiparticle Poisoning and Single Flux Quantum-Based Digital Control of Superconducting Qubits

by

Chuan-Hong Liu

A dissertation submitted in partial fulfillment

of the requirements for the degree of

Doctor of Philosophy

(Physics)

at the

UNIVERSITY OF WISCONSIN-MADISON

2023

Date of Final Oral Exam: 02/21/2023

Robert McDermott, Professor, Physics

Peter T. Timbie, Professor, Physics

Maxim G. Vavilov, Professor, Physics

Jennifer T. Choy, Assistant Professor, Engineering Physics

Abstract

Superconducting quantum bits (qubits) are a leading platform in the race to realize quantum computing, benefiting from the long coherence and high-fidelity operation and measurement. However, to realize fault-tolerant quantum computing, one still needs to push the superconducting qubit to have longer coherent times and find a practical road map for system scaling up. This thesis discusses two main topics: nonequilibrium quasiparticles, one dominant decoherence channel, and single flux quantum (SFQ)-based digital control, a potentially scalable quantum-classical interface.

The huge discrepancy between the measured density of quasiparticle excitations in superconductors and the density predicted by the Bardeen–Cooper–Schrieffer theory is a longstanding mystery in condensed matter physics. This mystery has taken new importance in recent years as researchers work to implement quantum processors based on superconducting quantum circuits, for which nonequilibrium quasiparticles represent a significant coherence channel. It has been proposed that the qubit structure itself acts as a resonant antenna for millimeter-wave radiation so that the broadband blackbody emission from higher temperature stages of the cryostat will efficiently generate quasiparticles at the Josephson junction of the qubit device. In this thesis, we describe the experimental validation of this model. We develop an innovative experimental protocol to y dose our qubit devices with millimeter-wave radiation, and we employ a quantum interferometric gate sequence to map out the detailed spectral response of the qubits. Furthermore, we show that the qubit initialization errors, a significant contributor to the quantum processor infidelity, are dominated by the resonant absorption of pair-breaking radiation.

Another open question we explore in this thesis is how to control large-scale qubit arrays that aspire to fault tolerance. The SFQ logic family can be leveraged

for superconducting qubits to achieve digital qubit control with a compact, proximal classical co-processor. Here, we implement a quantum-classical multi-chip module involving an SFQ pulse driver flip-chip coupled to a qubit chip. We demonstrate an order-of-magnitude reduction in gate infidelity compared to prior SFQ control implementation. The SFQ control scheme can yield significant reductions in the footprint of large-scale quantum processors, removing a major obstacle to practical quantum error correction.

Acknowledgements

Completing a Ph. D. is the most significant achievement thus far in my life. This would be absolutely impossible without the encouragement and kindness of people around me, to whom I extend my gratitude and appreciation.

First and foremost, I would like to thank my advisor, Professor Robert McDermott, for his guidance, support, and trust over the last four and half years in the McDermott Lab. Robert's constant enthusiasm toward physics and desire to realize a quantum computer is inspirational. From big pictures and minute details, Robert is always there to guide me and answer all the questions, even during the most challenging time of the pandemic and when he was fighting for his life. Under him, I grew up from a rookie in the area of superconducting quantum circuits to an independent researcher with my taste in the field while staying sharp and grounded.

Beyond Robert, I want to acknowledge many members of the McDermott Lab. I want to thank Dr. Edward M. Leonard and Dr. Matthew A. Beck for handing me the SFQ-Qubit project. At the beginning of my research life, I want to thank Dr. Shaojiang Zhu for mentoring me to do an HF dip, Dr. Bradley Christensen for helping me set up qubit measurement, Dr. Andrey R. Klots to explaining virtual photons to me, and Dr. Nathan Holman (our dot brother) to show me how to wire up an ADR. Dr. Alexander Opremcak (op-amp) taught me the fundamentals of circuit quantum electrodynamics. Alex's exercises on transmons are still used to test our new graduate students. I still remember the days Alex and I spent together debugging and upgrading our Leiden dilution refrigerator. Dr. Christopher D. Wilen taught me how to write and evaporate Josephson junctions and tirelessly explained quasiparticles and American culture. Dr. David C. Harrison, our productive postdoc hired during the pandemic, made my life much easier for the antenna experiment. Dave also set a great example of how to convey knowledge to others

and patiently help the lab's younger generation. I want to take a moment to thank Abigail Shearrow for maintaining a scalable lab. It is also good to see Abigail and Sohair Abdullah become competent researchers. The lab groundwork done by Francisco (Paco) Schlenker and Gabe Bernhardt is also highly appreciated. In addition to the lab members, I want to thank several people from the department staff where their work is not always seen: Ann R Austin, who makes the purchase experience smooth; Chad W Seys, who can set up the SMB maintenance during the Christmas to save graduate students' time; Douglas E Dummer who provides cheap and reliable customized sample boxes; and last but not least Billy James Gates who fixed one of our 20+ years old RF generator.

Furthermore, many parts of this thesis could not have been completed without our productive and supportive collaborators: Professor Britton L.T. Plourde and his group at Syracuse University, Dr. Samuel P. Benz and Dr. Pete F. Hopkins and their colleagues at the National Institute of Standards and Technology, and Dr. Jonathan L. DuBois at the Lawrence Livermore National Lab.

I am very grateful for my family. My grandpa, Tiancheng Ma, taught me mathematics as a kid. I wouldn't be able to pursue a Ph.D. degree without the efforts my grandpa has put into me. My parents, Hongyu Ma and Jun Yang, are always there to support me during the rougest times. The time I spent with my grandma Yuru Liu and aunt Jin Ma during my childhood is always memorable. I wish my father, Xu Liu, had the chance to see that I have gone so far.

Finally, I feel fortunate to thank my best friend and partner, Dr. Yanhe Huang. After many years of a long-distance relationship, it is time for us to write a new chapter of our story.

Contents

Chapter 1

Introduction

1.1 Quantum Bit

What is a quantum bit or qubit? Similar as a classic bit, qubit has a state, either $|0\rangle$ or $|1\rangle$. The critical difference between classic and quantum bits is that qubit can be in superposition of two states:

$$|\psi\rangle = \alpha|0\rangle + \beta|1\rangle, \tag{1.1}$$

where α and β are complex numbers, satisfying $|\alpha|^2 + |\beta|^2 = 1$. In other words, the state of a qubit can be seen as a vector in a two-dimensional complex space vector space. $|0\rangle$ or $|1\rangle$ are the computational basis states, and form an orthonormal basis for this two-dimensional space.

One useful way to picture qubits is the following Bloch sphere representation. Because the amplitude of the qubit vector is 1, Eq. 1.1 can be rewritten as

$$|\psi\rangle = e^{i\gamma}\left(\cos\frac{\theta}{2}|0\rangle + e^{i\phi}\sin\frac{\theta}{2}|1\rangle\right). \tag{1.2}$$

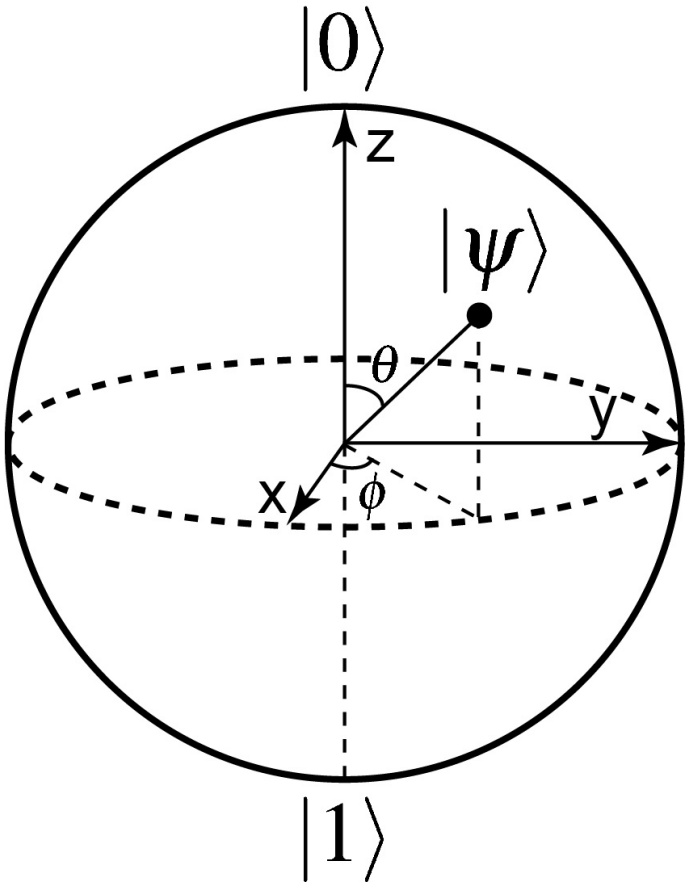

Figure 1.1: **Bloch sphere representation of a qubit**

where γ, θ, and ϕ are real numbers. We can ignore the the global phase factor $e^{i\gamma}$, since it has no observable effects. The qubit state vector can be effectively expressed as

$$|\psi\rangle = \cos\frac{\theta}{2}|0\rangle + e^{i\phi}\sin\frac{\theta}{2}|1\rangle, \tag{1.3}$$

The real number θ and ϕ define a point on the unit three-dimensional sphere, as shown in Fig. 1.1. This sphere is often called the *Bloch sphere*. It provides an intuitive visualization of the state of a single qubit.

1.2 Quantum Computing Platform

In the last two decades, tremendous efforts have been made to realize quantum computing hardware with the potential to tackle challenges that are intractable on classical computers. Various hardware platforms for quantum information science are under active and rapid development. To build large-scale quantum systems based on these technologies, one must achieve error rates much lower than the state-of-the-art devices, or explore new platform. Here we identify several promising quantum hardware platforms in the race of quantum computing.

1.2.1 Superconducting Circuits

Superconducting quantum computing is one leading candidate in the quantum information science field. In 2019, the Martinis group at Google demonstrated quantum supremacy [1] with a 53-qubit chip. This thesis will further discuss quantum computing based on superconducting electronic circuits as the main topic.

1.2.2 Silicon-Based Quantum Dots

Quantum dots are one quantum computing platform based on semiconductor particles. Their size is typical of a few nanometers. Thus they have optical and electronic properties well described by quantum mechanics. Owing to quantum dots' quantum behavior, they can be used as an artificial atom to achieve gate-based quantum computing [2].

1.2.3 Nitrogen-Vacancy Color Centers

A defect in diamond, known as the nitrogen-vacancy (NV) center, is identified and designed for use as qubits [3]. The NV center stand out for its robustness at room

temperature. The quantum state can be initialized, operated, and readout with high fidelity.

1.2.4 Trapped Ions

Ions, charged atomic particles, are one promising approach to a scalable quantum system. The single trapped ions can be well isolated and protected from the noisy environment, representing stable elementary quantum systems [4]. Laser cooling can bring ions nearly to the rest; at the same time, both the internal electronic states and external motion can be coupled to and manipulated by electromagnetic fields. Under such well-controlled conditions, trapped ions serve as an excellent candidate for studying quantum optical behavior.

1.2.5 Rydberg Atoms

A Rydberg atom is an excited atom with one or more electrons that are far away from the nucleus or equivalently have principal quantum number $n \gg 1$. Such atoms have exaggerated atomic characteristics such as dipole-dipole interaction that scale as n^4 and radiative lifetimes that scale as n^3 [5]. As a result, one can take advantage of these properties to realize quantum gates operation between neutral atom qubits.

1.2.6 Photonic Systems

Optical quantum computing is another paradigm of quantum computing. The optical system uses photons as information carriers. In 2020, the Pan group at USTC demonstrated quantum computational advantage using a prototype machine *Jiuzhang* [6], where they performed Gaussian boson sampling.

Chapter 2

Superconducting Devices

Instigating and controlling the behavior of electrons is key to most of the condensed matter physics research. Among all the platforms, superconductors are one of the most well-studied materials; and numerous superconducting devices serve as ideal quantum systems to understand the fascinating properties of superconductors.

In terms of quantum information science and this thesis, the superconductor-insulator-superconductor weak links (tunnel junction) based on the Josephson effect is the heart of all the superconducting devices. In this chapter, we will review the Josephson relations. Then we will discuss two important Josephson junction-based technologies used in this thesis: superconducting qubit and single flux quantum digital logic. Finally, we will introduce quasiparticle excitations of superconductors, which make ideal superconductors dissipative.

2.1 Josephson Junction

Superconductivity allows one to add nonlinearity into quantum electrical circuits without introducing dissipation. The Josephson junction is an element that is both a high-quality factor and operational at millikelvin temperatures.

A Josephson junction is a type of superconducting tunnel junction that consists of two superconducting electrodes separated by a thin insulating barrier, which allows the flow of current without resistance. The Josephson effect, discovered by physicist Brian Josephson in 1962 [7], is the phenomenon where a supercurrent flows through the junction due to the quantum mechanical tunneling of Cooper pairs, the pairs of electrons responsible for superconductivity, through the insulating barrier.

Josephson shows that this zero voltage supercurrent is given by

$$I = I_c \sin \phi, \tag{2.1}$$

where the critical current I_c is the maximum supercurrent that the junction can support, and ϕ is the difference in the phase of the Ginzburg-Landau wavefunction in the two electrodes. The critical current is determined by the junction area, material parameters, and temperatures. Once surpassing this current, Cooper pairs will be broken and dissipation kicks in. The junction switches from the superconducting branch into the normal state branch, accompanied with a finite voltage across the junction. We are going to see various important Josephson junction-based applications operating in different regime later in this thesis.

Josephson further predicted that if a voltage difference V were maintained across the junction, the phase difference ϕ would evolve according to

$$\frac{d\phi}{dt} = \frac{2\pi}{\Phi_0} V, \tag{2.2}$$

where $\Phi_0 = h/2e$ is the flux quantum. In this situation, an alternating current of amplitude I_c and frequency $f = V/\Phi_0$. As a result, the quantum energy hf equals the energy change of a Cooper pair transferred across the junction. The two relations, Eqs. 2.1 and 2.2, are known as the dc and ac Josephson effects,

respectively.

It is important to note that the critical current I_c scales with dimensions of the junction exactly as the inverse of its resistance R_n in the normal state. Thus, $I_c R_\mathrm{n}$ has an invariant value, which only depends on the materiel and the temperature. Ambegaokar and Baratoff [8] worked out the analytic result for this invariant for the full temperature

$$I_c R_\mathrm{n} = \frac{\pi\Delta}{2e} \tanh \frac{\Delta}{2kT}, \tag{2.3}$$

where Δ is the superconducting energy gap of the material, k is the Boltzmann constant. At temperature $T = 0$, the Ambegaokar-Baratoff formula reduces to

$$I_c R_\mathrm{n} = \frac{\pi\Delta_{T=0}}{2e}. \tag{2.4}$$

This allows experimentalists to know the critical current of the Josephson junction at room temperature by probing the junction's normal state resistance.

2.2 Superconducting Qubit

Although Josephson junction-based superconducting circuits are macroscopic in size, they have the most critical quantum properties needed for quantum computing: quantized energy levels, superposition of states, and entanglement [9]. Superconducting quantum bits are the fundamental building blocks of these electric circuits. Based on the way of controlling, there are three primary types of superconducting qubits: the flux qubit, the charge qubit, and the phase qubit. There also exist many hybridizations of these archetypes.

For the flux qubit, the Josephson energy to charging energy ratio is on the order of magnitude 10. It consists of a superconducting loop interrupted by one or three

Josephson junctions. The magnetic flux is the loop is the relevant quantum variable. The charge qubit is also known as the Cooper pair box (CPB). It has Josephson energy to charging energy ratio smaller than 1. Given that the CPB's connection to the environment is weak, the number of Cooper pairs on the qubit island is a discrete number. The phase qubit consists of a single current-biased Josephson junction. The Josephson energy to charing enery ratio of a phase qubit is on the order of magnitude of one million.

For hybridizations superconducting qubits, let's show the two most famous ones.

- Transmons [10]. Transmons are based on the charge qubit, where the Josephson junction is capacitively shunted by a large capacitor. The Josephson energy to charging energy ratio is relatively large. This is to reduce its sensitivity to the charge nose.

- Fluxonium [11]. Fluxonium qubits are a special type of flux qubits operating at low frequency. This makes fluxonium benefit from long coherence times.

2.3 Single Flux Quantum

Single Flux Quantum (SFQ) is a technology used in superconducting digital electronics. In SFQ, the flow of electrical current is quantized into discrete units called flux quanta. This allows the creation of superconducting digital circuits that can operate at very high speeds and consume very little power. SFQ technology has been used in various applications, including high-speed digital signal processing and quantum computing.

The essential physical phenomena underlying the operation of superconducting logic circuits are the superconductivity effects, the quantization of magnetic flux, and the Josephson effect. The flux quantization enables ballistic signal transfer not

limited by the power necessary to charge the capacitance of interconnect lines. The most significant advantage of SFQ digital logic is energy efficiency over conventional CMOS technology [12].

The magnetic flux quantization introduces the fundamental distinction between the operation of CMOS and SFQ circuits. The magnetic flux in a superconducting loop can only take values are integer multiples of the flux quantum

$$\Phi_0 = \frac{h}{2e} \approx 2.07 \times 10^{-15} \text{ Wb}, \tag{2.5}$$

where h is the Planck constant, and e is the electron charge. The logic "1" and "0" is based on the quantization of the magnetic flux. Typically, the presence or absence of an SFQ in the superconducting loop is regarded as the logical unity or zero.

The nonlinear superconducting element-Josephson junction-is the most critical component of the SFQ circuit. One of the essential characteristics of a Josephson junction is the critical current I_c. I_c is the maximum superconducting current allowed through the junction. The digital logic operation relies on the junction transition from the superconducting branch to the normal state branch. A Josephson junction can be switched from the superconducting to the normal resistive state by surpassing the critical current. This transition allows a change of the magnetic flux in the superconducting loop.

The most common Josephson junction is realized by a superconductor-insulator-superconductor (SIS) sandwich structure. The dynamics of a SIS junction can be described by the resistively shunted junction model with capacitance [13]. The ac Josephson effect connects the voltage at the Josephson junction in the resistive state. According to this relation, an increase of 2π in the phase of the Josephson junction

is accompanied by a voltage pulse $V(t)$ across the junction satisfying

$$\int V(t)dt = \Phi_0. \tag{2.6}$$

As a result, a switch of the Josephson junction from superconducting branch to normal resistive branch yields the transmission of an SFQ pulse through the junction.

For typical SFQ logic circuits based on niobium, we provide the critical parameters here. The critical current I_c is of order 100 μA; the energy dissipated in one switching event is $E \approx I_c\Phi_0 \approx 2 \times 10^{-19}$ J. Another important parameter is the characteristic frequency of the Josephson junction switching process, ω_c. This is determined by the parameters of the Josephson junction

$$\omega_c = \frac{2\pi}{\Phi_0} I_c R_n, \tag{2.7}$$

where R_n is the normal state resistance of the Josephson junction. For niobium-based junctions, $\omega_c/2\pi \approx 100 - 350$ GHz.

2.4 Quasiparticles

According the BCS theory of superconductivity, the ground state of superconductors is formed of Cooper pairs of electrons with equal and opposite momentum and spin. Broken Cooper pairs, also known as quasiparticles, are excitations from the BCS ground state of superconductors. The energies of such single-particle excitations from this state are

$$\epsilon_k = \sqrt{\xi_k^2 + \Delta^2}. \tag{2.8}$$

Here, ξ_k is the kinetic energy of an electron

$$\xi_k^2 = \frac{\hbar^2 k^2}{2m_e} - \epsilon_{\mathrm{F}}, \tag{2.9}$$

where m_e is the mass of the electron, k is the momentum of the electron with respect to the Fermi energy ϵ_{F}; Δ is superconducting energy gap. The pairing interaction is much weaker compared to the Fermi energy

$$\Delta \ll \epsilon_{\mathrm{F}}. \tag{2.10}$$

The gap energy is closely related to the critical temperature T_{c}

$$\Delta = 1.74 k_{\mathrm{B}} T_{\mathrm{c}}, \tag{2.11}$$

where k_{B} is the Boltzmann constant. For relevant materials commonly used in superconducting quantum circuits, such as aluminum, tantalum, niobium, 2Δ are of order hundreds to thousands of μeV.

One key prediction of BCS theory was that a minimum energy 2Δ should be required to break a Cooper pair, generating two quasiparticles. At temperature $T = 0$, no quasiparticles should exist. For temperature $T \ll T_{\mathrm{c}}$, the quasiparticle density should be greatly suppressed. However, in a dilution refrigerator where $T \sim 10 - 20$ mK, large amount of non-equilibrium quasiparticles are observed in superconducting quantum devices. The abundance of such quasiparticles not only limit the state-of-the art superconducting qubit performance, but also limit the sensitivity of quasiparticle-based superconducting detectors, e.g., microwave kinetic inductance detectors and superconducting photon detectors.

A deep understanding of the quasiparticle generation mechanism and how it

interacts with superconducting quantum devices is critical to engineer future generation of qubits and detectors with robustness against quasiparticle-induced error. We will focus on discussing on generation mechanism, pair-breaking photon absorption, in Chapter 5 and Chapter 6. Related quasiparticle suppression techniques such as gap engineering and acoustic mismatch will be discussed in Chapter 8.

Chapter 3

Circuit Quantum Electrodynamics

In this chapter, we give a brief introduction to the field of circuit quantum electrodynamics and discuss the fundamental building blocks of our experiment, the LC resonator and superconducting transmon qubit. We start with the quantum electric LC resonator, then apply similar concepts to quantize the superconducting transmon qubit. We then show several ways of finding the (fundamental) modes of the transmon qubit. Finally, we describe how to control and readout the information of the transmon qubit. The primary sources for this chapter were [14, 15].

3.1 The LC Resonator

To understand the quantum characteristics of an electrical circuit, we start with the well-known oscillating LC resonator. Shown in Fig. 3.1**a**, an LC resonator is characterized by its inductance L and capacitance C. One can equivalently describe the resonator by its angular frequency $\omega_r = 1/\sqrt{LC}$ and its characteristic impedance $Z_r = \sqrt{L/C}$. Summing the electrical energy and magnetic energy, we can write the

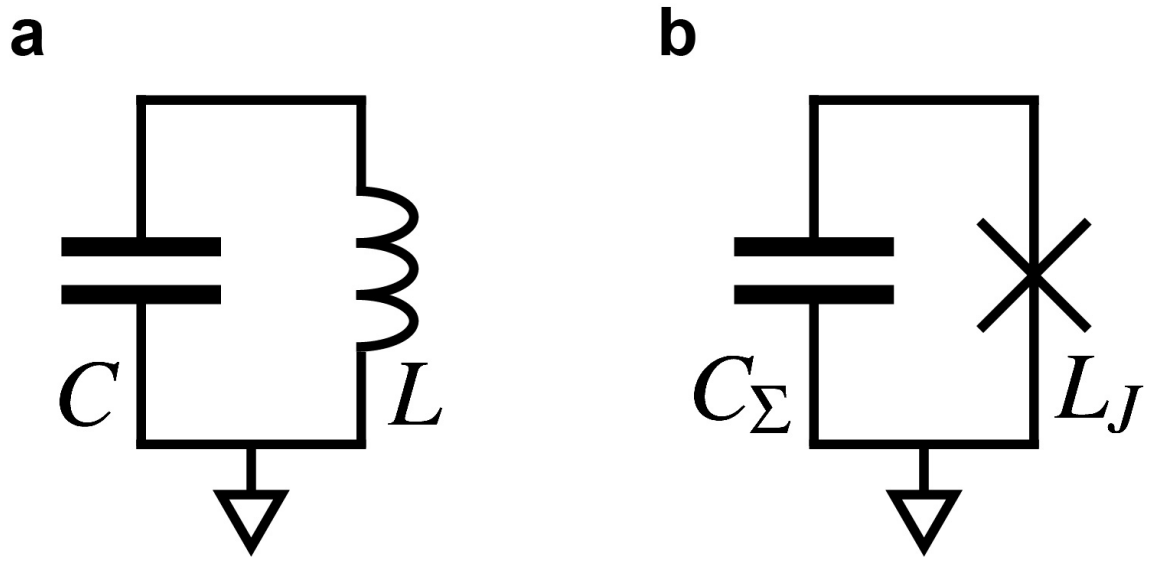

Figure 3.1: **Circuit diagram of LC resonator (a) and capacitively-shunted Josephson junction (b).** In **b**, the total capacitance C_Σ is the sum of shunt capacitance and the self capacitance of the Josephson junction; L_J is the Josephson inductance.

Hamiltonian for the LC resonator

$$H_{LC} = \frac{Q^2}{2C} + \frac{\Phi^2}{2L}, \tag{3.1}$$

where Q is the charge on the capacitor and Φ is the flux threading the inductor.

The electrical circuit resonator inherits all the properties of a harmonic oscillator. The charge and flux variables are two conjugate coordinates satisfying the canonical commutation relation

$$[\hat{\Phi}, \hat{Q}] = i\hbar. \tag{3.2}$$

Following the standard treatment of harmonic oscillator, we introduce the anni-

hilation and creation operators

$$\hat{a} = \sqrt{\frac{1}{2\hbar Z_r}}(\Phi + iZ_r Q) \tag{3.3}$$

$$\hat{a}^\dagger = \sqrt{\frac{1}{2\hbar Z_r}}(\Phi - iZ_r Q). \tag{3.4}$$

Then the flux and charge operators can be expressed as

$$\hat{\Phi} = \sqrt{\frac{\hbar Z_r}{2}}(\hat{a}^\dagger + \hat{a}) \tag{3.5}$$

$$= \Phi_{\text{zpf}}(\hat{a}^\dagger + \hat{a}) \tag{3.6}$$

$$\hat{Q} = i\sqrt{\frac{\hbar}{2Z_r}}(\hat{a}^\dagger - \hat{a}) \tag{3.7}$$

$$= iQ_{\text{zpf}}(\hat{a}^\dagger - \hat{a}), \tag{3.8}$$

where Φ_{zpf} and Q_{zpf} are the magnitude of the zero-point fluctuations of the flux and charge.

With the definitions above, the Hamiltonian Eq. 3.1 takes the familiar form

$$\hat{H}_{LC} = \hbar\omega_r(\hat{a}^\dagger\hat{a} + \frac{1}{2}). \tag{3.9}$$

3.2 The Superconducting Transmon Qubit

Until now, we show that the electric LC resonator can be prepared in their quantum-mechanical ground state and the energy levels are evenly spaced with $\hbar\omega_r$. However, to perform quantum computation, one needs to address each transition individually, so it is challenging to use such a linear resonator to realize quantum computing. Some degree of nonlinearity is therefore needed to make the harmonic oscillator anharmonic. Fortunately, as discussed in Sec 2.1, the Josephson junction is a non-

linear circuit element with high quality factor. The Josephson junction is essentially a non-linear inductor. We rewrite energy associated with the coherent tunneling of Cooper pairs across the junction

$$E = -E_J \cos\phi, \tag{3.10}$$

where the Josephson energy is $E_J = I_c\Phi_0/2\pi$ and the branch flux is $\phi = 2\pi\Phi/\Phi_0$. The Josephson energy can also be expressed with the Josephson inductance

$$E_J = L_J I_c^2 = \frac{\Phi_0^2}{4\pi^2 L_J^2}, \tag{3.11}$$

where $L_J = \Phi_0/(2\pi I_c)$.

We replace the linear inductor with the nonlinear Josephson junction (in Fig. 3.1**b**), similar to Eq. 3.1, the quantized Hamiltonian of the capactively shunted Josephson junction can be written as

$$\hat{H}_T = 4E_C(\hat{n} - n_g)^2 - E_J \cos\hat{\phi}. \tag{3.12}$$

In Eq. 3.12, $E_C = e^2/2C_\Sigma$ is the charging energy, where C_Σ is the total capacitance of the shunting capacitor and the self-capacitance of the Josephson junction; $\hat{n} = \hat{Q}/2e$ is the charge number operator; $n_g = Q_g/2e$ is charge offset of an external electric gate bias; $\hat{\phi}$ is the phase operator. The two operators satisfy the commutation relation $[\hat{\phi}, \hat{n}] = i$.

The ratio E_J/E_C controls the spectrum of Eq. 3.12. In the transmon regime, this ratio is large, with typical values being $E_J/E_C \sim 20 - 80$ ([10]). In this limit, we can find out the transmon frequency with various methods discussed in Sec. 3.3.

3.3 Four Different Ways to Find the Transmon Frequency

In this section, we show how to find the fundamental mode of the transmon Hamiltonian with different methods of different precision.

3.3.1 The Linear Part

In the next few sections, we understand the transmon is a *weakly*-anharmonic oscillator, the Hamiltonian Eq. 3.12 is still dominated by the linear term. Under this reasonable approximation, we show that

$$\hat{H}_T \approx 4E_C\hat{n}^2 + \frac{1}{2}E_J\hat{\phi}^2. \tag{3.13}$$

One can find the transmon frequency by classical treatment of this Hamiltonian

$$\omega_T = \sqrt{8E_CE_J}/\hbar \tag{3.14}$$

3.3.2 First-Order Perturbation

In addition to the linear part, we keep the first dominant nonlinear term of the Josephson energy

$$\hat{H}_T \approx 4E_C\hat{n}^2 + \frac{1}{2}E_J\hat{\phi}^2 - \frac{1}{4!}E_J\hat{\phi}^4. \tag{3.15}$$

Following Sec. 3.1, we introduce the creation and annihilation operators chosen to diagonalize the linear terms of Eq. 3.15, we have

$$\hat{\phi} = \left(\frac{2E_C}{E_J}\right)^{1/4} (\hat{b}^\dagger + \hat{b}), \tag{3.16}$$

$$\hat{n} = \frac{i}{2}\left(\frac{E_J}{E_C}\right)^{1/4} (\hat{b}^\dagger - \hat{b}). \tag{3.17}$$

Plugging these expressions in Eq. 3.15, we arrive at

$$\hat{H}_T \approx \sqrt{8E_C E_J}\hat{b}^\dagger\hat{b} - \frac{E_C}{12}(\hat{b}^\dagger + \hat{b})^4, \tag{3.18}$$

$$= \hat{H}_0 + \Delta\hat{H}. \tag{3.19}$$

From here, we can use the time-independent non-degenerate first-order perturbation theory. The unperturbed Hamiltonian is just the harmonic oscillator with eigenvalues $E_n^{(0)} = n\sqrt{8E_C E_J}$ (ignoring the constant 1/2) and eigenstates $|n\rangle$, the first order correction to the energy is

$$E_n^{(1)} = \langle n|\Delta\hat{H}|n\rangle. \tag{3.20}$$

Plugging the creation and annihilation operators, we have

$$E_n^{(1)} = -\frac{E_C}{12}(6n^2 + 6n + 3). \tag{3.21}$$

Here, we can find the energy level difference is

$$E_{n,n-1} = E_n - E_{n-1} = \sqrt{8E_C E_J} - nE_C. \tag{3.22}$$

With all the analysis above, we show the frequencies for the lowest two modes

$$\omega_{T,10} = (\sqrt{8E_C E_J} - E_C)/\hbar, \tag{3.23}$$

$$\omega_{T,21} = (\sqrt{8E_C E_J} - 2E_C)/\hbar. \tag{3.24}$$

Compared with the linear result from Eq. 3.14, we notice two things. First, the linear result is very close to the Eq. 3.23, the correction provided by E_C is $5-10\%$ for typical parameters. Second, the perturbation theory tells us how anharmonic our transmon qubit is. Between each transition frequency, the anharmonicity is determined by the charging energy E_C.

3.3.3 Matrix Diagonalization

In the two methods discussed above, we have made appropriate assumptions and approximations. Here, let's solve the Hamiltonian of the transmon without any approximations with matrix diagonalization. This method can be applied into different basis and be generalized into other superconducting qubit system with different forms of Hamiltonian.

We want to solve this problem in the charge basis where it has more physical meaning. In the charge basis, we can easily reveal one critical property of the Transmon qubit, the charge sensitivity. Since the Transmon qubit is based on the ordinary Cooper pair box (CPB), the effective offset charge n_g of the transmon can also be controlled by voltage gate capacitively coupled to the superconducting island. At the same time, n_g is also sensitive to the environment induced charge noise. The charge dispersion of the Transmon qubit is due to the energy levels' dependence on the offset charge.

It is critical to write $\cos\hat{\phi}$ in terms of $\hat{n}$. Note that $\hat{n}$ is the number of Cooper

pairs on the qubit island. In the following proof, we will show that

$$e^{\pm i\hat{\phi}}|n\rangle = |n \pm 1\rangle. \tag{3.25}$$

Recall the commutation relations

$$[\hat{\phi}, \hat{n}] = i, \tag{3.26}$$

and

$$[A^m, B] = mA^{m-1}\,[A, B] \;\text{ if }\; [[A, B], A] = 0. \tag{3.27}$$

We have

$$\left[e^{i\hat{\phi}}, \hat{n}\right]|n\rangle = (n - \hat{n})e^{i\hat{\phi}}|n\rangle, \tag{3.28}$$

and

$$\left[e^{i\hat{\phi}}, \hat{n}\right] = \sum_{m=0}^{\infty}\left[\frac{(i\phi)^m}{m!}, \hat{n}\right] \tag{3.29}$$

$$= \sum_{m=1}^{\infty}\left(\frac{(i\phi)^{m-1}}{(m-1)!}\left[i\hat{\phi}, \hat{n}\right]\right) \tag{3.30}$$

$$= \sum_{m=1}^{\infty}\left(\frac{(i\phi)^{m-1}}{(m-1)!}(-1)\right) \tag{3.31}$$

$$= -e^{i\hat{\phi}}. \tag{3.32}$$

Comparing the two equations above, we arrive

$$-e^{i\hat{\phi}}|n\rangle = (n - \hat{n})e^{i\hat{\phi}}|n\rangle, \tag{3.33}$$

$$\hat{n}e^{i\hat{\phi}}|n\rangle = (n + 1)|n\rangle. \tag{3.34}$$

The negative term $e^{-i\hat{\phi}}$ can be proven in the same way, so we recover the Eq. 3.25.

Now, with $\cos\hat{\phi} = \frac{1}{2}(e^{i\hat{\phi}} + e^{-i\hat{\phi}})$, we write the Hamiltion of the transmon in charge basis

$$\hat{H}_T = 4E_C\hat{n}^2 - E_J\frac{1}{2}(e^{i\hat{\phi}} + e^{-i\hat{\phi}}) \tag{3.35}$$

$$= \sum_{n=-\infty}^{\infty}\left(4E_C\hat{n}^2(|n\rangle\langle n|) - \frac{E_J}{2}(e^{i\hat{\phi}} + e^{-i\hat{\phi}})(|n\rangle\langle n|)\right) \tag{3.36}$$

$$= \sum_{n=-\infty}^{\infty}\left(4E_Cn^2|n\rangle\langle n| - \frac{E_J}{2}\left(|n+1\rangle\langle n| + |n-1\rangle\langle n|\right)\right). \tag{3.37}$$

This is the well-known Hamiltonian of Cooper pair box in charge basis. Let's explicitly write out the matrix form of $\hat{H}_T/\hbar$ for $-3 \leq n \leq 3$

$$\begin{array}{c} \\ n=-3 \\ n=-2 \\ n=-1 \\ n=0 \\ n=1 \\ n=2 \\ n=3 \end{array}\begin{array}{c} \begin{array}{ccccccc} n=-3 & n=-2 & n=-1 & n=0 & n=1 & n=2 & n=3 \end{array} \\ \begin{pmatrix} 4E_C(-3)^2 & -E_J/2 & 0 & 0 & 0 & 0 & 0 \\ -E_J/2 & 4E_C(-2)^2 & -E_J/2 & 0 & 0 & 0 & 0 \\ 0 & -E_J/2 & 4E_C(-1)^2 & -E_J/2 & 0 & 0 & 0 \\ 0 & 0 & -E_J/2 & 4E_C0^2 & -E_J/2 & 0 & 0 \\ 0 & 0 & 0 & -E_J/2 & 4E_C(1)^2 & -E_J/2 & 0 \\ 0 & 0 & 0 & 0 & -E_J/2 & 4E_C(2)^2 & -E_J/2 \\ 0 & 0 & 0 & 0 & 0 & -E_J/2 & 4E_C(3)^2 \end{pmatrix} \end{array}. \tag{3.38}$$

This matrix can be solved numerically. When we have offset charge, the n^2 can be replaced with $(n-n_g)^2$. This can achieve very high precision with $n > 10$ and with physical meaning. The matrix diagonalization does not need any assumption and will show the charge dispersion of the spectrum. Note this form is very similar to Toeplitz matrix. The difference is that the diagonal element is not constant here. This does not have a analytic solution. To get a better understanding of the charge dispersion, please see the discussion in Sec. 3.4 and Fig. 3.2 for more details.

3.3.4 Mathieu Function

Now we finally reach the analytic solution in the phase basis. This solution is exact; however, it cannot easily be generalized to other qubit systems with different forms of Hamiltonians and it does little to build physical intuition. Based on the commutation relation

$$\hat{n} = \frac{1}{i}\frac{\partial}{\partial\hat{\phi}}. \tag{3.39}$$

The transmon Hamiltonian can be rewritten as

$$\hat{H} = 4E_C(\frac{1}{i}\frac{\partial}{\partial\hat{\phi}})^2 - E_J\cos\hat{\phi}. \tag{3.40}$$

The Schrodinger equation takes the form

$$-4E_C\frac{\partial^2\Psi(\phi)}{\partial\hat{\phi}^2} - E_J\cos\hat{\phi}\Psi(\phi) = E\Psi(\phi), \tag{3.41}$$

with the periodic boundary condition $\Psi_k(\phi) = \Psi_k(\phi + 2\pi)$. This equation has analytic solution based on Mathieu equation.

3.3.5 Four Methods Summary

See Table 3.1 for comparison between all the four methods discussed above.

3.3.6 Transmon Hamiltonian Revisit

Let's revisit the transmon Hamiltonian (Eq. 3.12). This can be understood as the quantum rotor model introduced in the Koch paper [10]. In the limit of $E_J/E_C \gg 1$, we treat the E_J term as the potential energy term and E_C as the kinetic energy term. This is because the $E_J\cos\phi$ looks at a gravity potential term. Now, with this in

Table 3.1: **Comparison of four different methods finding qubit fundamental mode frequency.**

Method	Result	Anharm	Charge dispersion	Note
LC oscillator	$\sqrt{8E_JE_C}$	✗	✗	Fast, classical treatment
First-order perturbation	$\sqrt{8E_JE_C} - E_C$	✓	✗	Accurate enough
Matrix diagonalization	Numerical	✓	✓	Physical meaning, charge base, can be generalized into other bases and qubit systems
Mathieu function	$E_C a_{2[n_g+k(m,n_g)]}(-E_J/2E_C)$	✓	✓	Analytical, phase base

mind, C the capacitance is acting like a mass term in $\frac{p^2}{2m}$. Also, earlier we expanded the cos term and only keep the first order term, and why can we do that? This is because the E_J is so large, it is like a pendulum which oscillates at the lowest point where ϕ is very small. There will never be a 2π rotation of this quantum rotor. If there is, then the qubit is driven out of its cos potential, which is no longer a qubit. Also, due to the fact that Φ_{zpf} is small, so the expansion is valid.

3.4 Charge-Sensitive and Flux-Tunable Transmon Qubits

There are two types of transmon qubits studied extensively in the field based on their sensitivity of charge [10] and flux tunability [16, 17]. Sometimes, qubits with

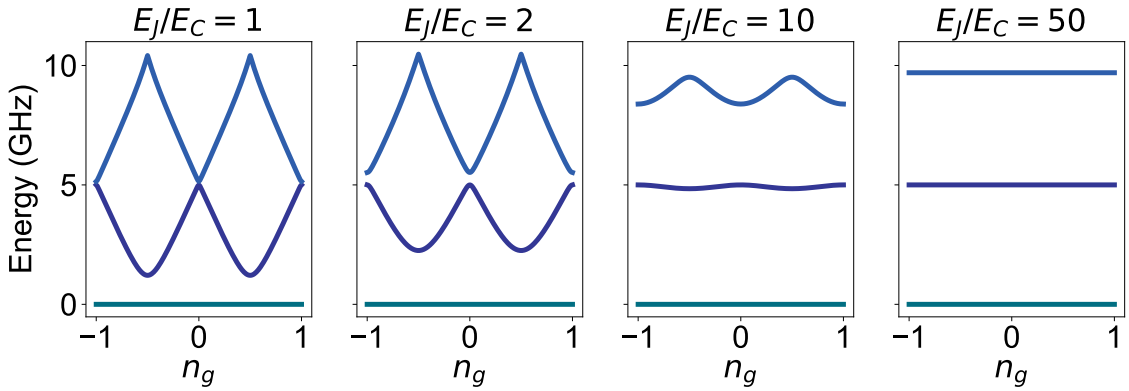

Figure 3.2: **Frequency difference $(E_n - E_0)/h$ of the first three energy levels of the transmon Hamiltonian.** The energy levels are obtained from the numerical diagonalization of Eq. 3.38 in the charge basis for a range of Josephson to charging energy ratio E_J/E_C for a fixed fundamental mode frequency $\omega_{T,10}/\hbar = 5$ GHz.

both charge sensitivity and flux tunability is used to explore the flux-dependent quasiparticle dynamics of superconducting qubit [18].

3.4.1 The Charge-Sensitive Transmon

In a charge-sensitive transmon, the charging energy is made large enough so that the energy levels of the transmon change noticeably with small changes in the charge on the qubit island. For typical charge-sensitive transmons, the ratio of Josephson energy to the charging energy E_J/E_C is around ~ 20; thus the maximum charge dispersion of the lowest energy levels is of order $\sim 1 - 10$ MHz. The sensitivity to charge makes this type of transmon an ideal platform to study the quasiparticles poisoning and detect single electron tunneling events.

3.4.2 The Flux-Tunable Transmon

The other useful type of qubit is the flux-tunable transmon. One single junction is replaced with a superconducting quantum interference device (SQUID) as shown in

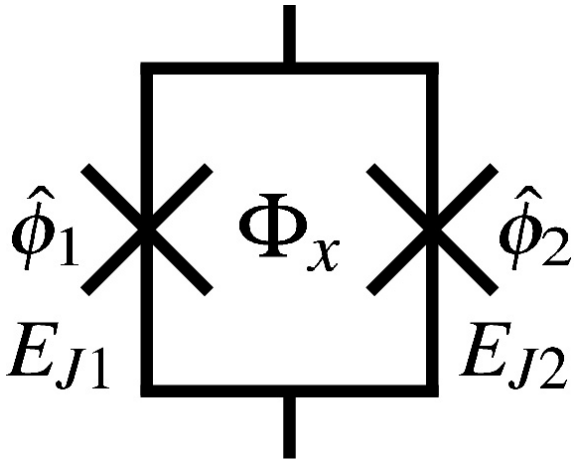

Figure 3.3: **Circuit diagram of superconducting quantum interference device (SQUID).**

Fig. 3.3. Since the Josephson energy of the SQUID can be tuned with an external magnetic field, the qubit energy levels can also be tuned. The coupling between frequency-tunable transmon qubits can be easily turned on and off [19]. The tunable range for typical device is several GHz.

Though the compact form of the SQUID's Josephson energy can be easily found, the detailed derivation is not obvious, as least to myself. We first re-express some parameters here

$$E_{J\Sigma} = E_{J1} + E_{J2} \text{ (total Josephson energy)}, \tag{3.42}$$

$$d = \frac{E_{J2} - E_{J1}}{E_{J2} + E_{J1}} \text{ (asmmetry of the SQUID)}, \tag{3.43}$$

$$\hat{\phi}_1 - \hat{\phi}_2 = 2\pi\Phi_x/\Phi_0 \ (\text{mod}2\pi) \tag{3.44}$$

where E_{J1} and E_{J1} are the Josephson energy of junction 1 and 2, $\hat{\phi}_1$ and $\hat{\phi}_2$ are phase difference across junction 1 and 2, and Φ_x is external flux through the SQUID as shown in Fig. 3.3. Let me show the derivation of the compact form of SQUID's Josephson energy. With $A = \frac{1}{2}(\hat{\phi}_1 - \hat{\phi}_2)$ and $B = \frac{1}{2}(\hat{\phi}_1 + \hat{\phi}_2)$, let us write down the

Josephson energy of a SQUID with asymmetric junctions

$$E_{J1}\cos\hat{\phi}_1 + E_{J2}\cos\hat{\phi}_2 = \frac{E_{J\Sigma}(1-d)}{2}\cos(A+B) + \frac{E_{J\Sigma}(1+d)}{2}\cos(A-B), \tag{3.45}$$

$$= \frac{E_{J\Sigma}}{2}\left((1-d)\cos(A+B) + (1+d)\cos(A-B)\right), \tag{3.46}$$

$$= E_{J\Sigma}\left(\cos A\cos B + d\sin A\sin B\right), \tag{3.47}$$

$$= E_{J\Sigma}\cos A\left(\cos B + d\tan A\sin B\right), \tag{3.48}$$

$$= E_{J\Sigma}\cos A\sqrt{1+d^2\tan^2 A}$$
$$\left(\frac{1}{\sqrt{1+d^2\tan^2 A}}\cos B + \frac{d\tan A}{\sqrt{1+d^2\tan^2 A}}\sin B\right), \tag{3.49}$$

$$= E_{J\Sigma}\cos A\sqrt{1+d^2\tan^2 A}\cos(B-B_0), \tag{3.50}$$

where $\cos B_0 = 1/\sqrt{1+d^2\tan^2 A}$, and $\sin B_0 = d\tan A/\sqrt{1+d^2\tan^2 A}$. Now this can be reduced to the original form:

$$E_{J1}\cos\hat{\phi}_1 + E_{J2}\cos\hat{\phi}_2 = E_{J\Sigma}\cos\left(\frac{\pi\Phi_x}{\Phi_0}\right)\sqrt{1+d^2\tan^2\left(\frac{\pi\Phi_x}{\Phi_0}\right)}\cos(\hat{\phi}-\phi_0) \tag{3.51}$$

, where $\tan\phi_0 = d\tan(\pi\Phi_x/\Phi_0)$.

Notice that, this can also be written as

$$= E_{J\Sigma}\cos B\sqrt{1+d^2\tan^2 B}\cos(A-A_0) \tag{3.52}$$

$$= E_{J\Sigma}\cos\hat{\phi}\sqrt{1+d^2\tan^2\hat{\phi}}\cos(\frac{\pi\Phi_x}{\Phi_0}-\Phi'), \tag{3.53}$$

where $\tan\Phi' = d\tan\hat{\phi}$. However, it is better to write the operator by itself with a simpler form.

3.5 Light-Matter Interaction: the Jaynes-Cummings Hamiltonian

The quantum harmonic oscillator and the superconducting transmon qubit are the two main blocks of the circuit quantum electrodynamics. In this section, we investigate the interaction between the two systems as shown in Fig. 3.4.

Due to the physical size required for the charging energy E_C, the transmon qubit can be capacitively coupled to 2D/3D microwave resonators. Similar to the transmon Hamiltonian, in the rotating-wave approximation, one can write out the Hamiltonian for the resonator-qubit system

$$\hat{H} \approx \hbar\omega_r \hat{a}^\dagger \hat{a} + \hbar\omega_q \hat{b}^\dagger \hat{b} - \frac{E_C}{2}\hat{b}^\dagger \hat{b}^\dagger \hat{b}\hat{b} + \hbar g(\hat{b}^\dagger \hat{a} + \hat{b}\hat{a}^\dagger), \tag{3.54}$$

where $\omega_q = (\sqrt{8E_C E_J} - E_C)/\hbar$. The electric-dipole interaction strength g can be expressed as

$$g = \omega_r \frac{C_g}{C_\Sigma}\left(\frac{E_J}{2E_C}\right)^{1/4}\frac{Z_r}{Z_{\text{vac}}}\sqrt{2\pi\alpha}, \tag{3.55}$$

where $\alpha = Z_{\text{vac}}/(2h/e^2)$ is the fine-structure constant and $Z_{\text{vac}} = \sqrt{\mu_0/\epsilon_0} \sim 377\Omega$ is the impedance of vacuum. The interaction strength g can be made large, much larger than the natural atoms in cavity QED [20].

If we strict the description of the transmon qubit to its lowest two levels (two-level system approximation), we can make the replacements

$$\hat{b}^\dagger \to \hat{\sigma}_+ = |e\rangle\langle g|, \tag{3.56}$$

$$\hat{b} \to \hat{\sigma}_- = |g\rangle\langle e|. \tag{3.57}$$

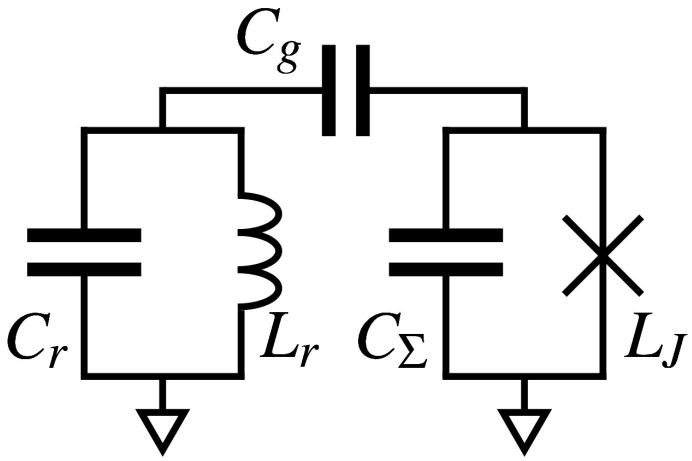

Figure 3.4: **Circuit diagram of capacitively coupled LC resonator and transmon qubit.**

With these approximation, we obtain the famous Jaynes-Cummings Hamiltonian

$$\hat{H}_{\mathrm{JC}} = \hbar\omega_r \hat{a}^\dagger \hat{a} + \frac{\hbar\omega_q}{2}\hat{\sigma}_z + \hbar g(\hat{a}^\dagger \hat{\sigma}_- + \hat{a}\hat{\sigma}_+) + \text{Constant}, \tag{3.58}$$

where $\hat{\sigma}_z = |e\rangle\langle e| - |g\rangle\langle g|$. The third term describes the coherent interaction of a single quantum energy through the light-matter (electromagnetic wave-transmon qubit) interaction. Please note, compared to Eq. 3.54, we have dropped out the anharmonicity term $-E_C/2$ here.

3.5.1 Dispersive Regime

For superconducting quantum computing, it is practical to work in the weak coupling regime $g/|\omega_q - \omega_r| \ll 1$, also known as the dispersive regime, where the coupling strength is much smaller than the detuning between the resonator and the qubit $\Delta = \omega_q - \omega_r$. There are two approaches to find an approximated Hamiltonian in this regime, Schrieffer-Wolff approach and Bogoliubov approach. Detailes can be

found in [21, 10]. Here we write down the result

$$\hat{H}_{\text{disp}} \approx \hbar\omega_r'\hat{a}^\dagger\hat{a} + \frac{\hbar\omega_q'}{2}\hat{\sigma}_z + \hbar\chi\hat{a}^\dagger\hat{a}\hat{\sigma}_z, \tag{3.59}$$

where χ is the dispersive cavity shift based on the qubit's state, with

$$\omega_r' = \omega_r - \frac{g^2}{\Delta - E_c/\hbar}, \tag{3.60}$$

$$\omega_q' = \omega_q + \frac{g^2}{\Delta}, \tag{3.61}$$

$$\chi = -\frac{g^2 E_C/\hbar}{\Delta(\Delta - E_C/\hbar)}. \tag{3.62}$$

The last term of the dispersion Hamiltonian Eq. 3.59 can be either understood with the resonator term or the qubit term. If it is combined with the resonator term, then we are going to see a qubit-state dependent resonator state, which is used for readout; it coupled to the qubit, then qubit frequency will be dependent on the photon number in the resonator, which is called ac Stark shift.

Chapter 4

A Quantum Engineer's Guide to Quasiparticles

In the discussion of this chapter, we focus on the experimental side of quasiparticles. Please see recent papers [22, 23] for theory studies.

4.1 Generation Mechanisms

In this section, we summarize several quasiparticle generation mechanisms known to the field; they are from the ambient device environment, not generated on purpose. With better understanding of the background quasiparticle generation mechanisms, proper mitigation and suppression methods can be applied and engineered to reduce the quasiparticle poisoning level of the superconducting device.

We define several quantities used in the literature that describe how many quasiparticles there are in a device. The total number of quasiparticles and Cooper pairs in the device N_{qp} and N_{cp}; the number of quasiparticles and Cooper pairs volume

density $n_{\rm qp}$ and $n_{\rm cp}$; and the normalized quasiparticle density

$$x_{\rm qp} \equiv \frac{n_{\rm qp}}{n_{\rm cp}} = \frac{N_{\rm qp}}{N_{\rm cp}} \tag{4.1}$$

4.1.1 Thermal Quasiparticles

The first obvious source is the ambient temperature of the superconducting quantum device. To present a concise and analytical expression for thermally-generated quasiparticles, there are two approximations need to be made: all quasiparticles obey Fermi-Dirac distribution in energy; there are few quasiparticles that are localized very near the gap edge to avoid divergence. With these two reasonable assumptions, we arrive the expression for thermal-equilibrium quasiparticle density [24]

$$x_{\rm qp}^{\rm th} \approx \sqrt{2\pi k_{\rm B}T/\Delta}e^{-\Delta/k_{\rm B}T}. \tag{4.2}$$

Ideally, at temperature $T = 0$, the probability that quasiparticles will be excited above the energy gap is 0. The realistic temperature of a well-thermalized device is close to the base temperature of its environment, i.e. the mix chamber of a dilution refrigerator. For $T \approx 20$mK, $x_{\rm qp}^{\rm th} \approx 10^{-50}$. However, experiments show that the inferred quasiparticle densities have been in the range of $10^{-10} - 10^{-5}$, much higher than the thermal equilibrium.

The huge discrepancy indicates that there are other quasiparticle generation mechanisms other than thermally activated.

4.1.2 High Energy Impacts

Recent studies show that ionizing radiation from high energy particles, e.g., cosmic rays and radioactive sources, lead to an elevated quasiparticle density [25, 26, 27].

These events cause qubit relaxation errors and charge jumps. Without explicit introducing radioactive materials to the device background, the cosmic-ray muons and γ-rays from the background radioactivity induce burst of quasiparticle poisoning events on the multi-qubit array, which lead to correlated error at a rate of $\sim 0.01 - 0.1$ s. While the high-energy-particle-induced correlated errors is a potential showstopper of superconducting quantum computing, it cannot well explain the steady state quasiparticle density way above the thermal equilibrium seen in superconducting devices [28, 29, 30, 31, 32, 33].

4.1.3 Pair-breaking Photon Absorption

Pair-breaking photon-absorption [34, 35, 36, 37] is another quasiparticle generation source. Contrary to the burst high energy impacts, photon-absorption of millimeter waves is a steady state scenario. In cryostats, blackbody photons from higher temperature stages can leak into the device located at millikelvin stage. These stray photons provide a steady pair-breaking energy source. The millimeter wave photons are absorbed by the spurious antenna modes of superconducting qubit [35, 37]. Details of the antenna modes will be discussed in chapter 5 and chapter 6. Here we follow [34] to discuss the photon-absorption on qubit's state transition.

Using Fermi's golden rule, we can find the photon-assisted transition rate Γ_{if}^{ph} describe the following process

$$\gamma_{E>2\Delta} + \text{Cooper pair} + |i\rangle \rightarrow \text{broken Cooper pair} + |f\rangle, \tag{4.3}$$

where $\gamma_{E>2\Delta}$ is the pair-breaking photon, and $|i\rangle \rightarrow$ and $|f\rangle \rightarrow$ are the initial and final state of the qubit, respectively. When one pair-breaking photon is absorbed by the qubit, it will induce qubit state transition and generate two quasiparticles. The

transition rate between the initial and final state can be found as

$$\Gamma_{if}^{\mathrm{ph}} = \Gamma_\nu \left[\left| \langle f | \cos \frac{\phi}{2} | i \rangle \right|^2 S_- \left(\frac{\hbar\omega_\nu + \hbar\omega_{if}}{\Delta} \right) + \left| \langle f | \sin \frac{\phi}{2} | i \rangle \right|^2 S_+ \left(\frac{\hbar\omega_\nu + \hbar\omega_{if}}{\Delta} \right) \right], \tag{4.4}$$

where Γ_ν is the common characteristic scale for photon absorption, and the structure factor $S_\pm$ takes the form in the limit of $\hbar\omega_\nu \gg \hbar\omega_{if}$:

$$S_\pm(\hbar\omega_\nu/\Delta) = \int_1^{\hbar\omega_\nu/\Delta - 1} dx \frac{x(\hbar\omega_\nu/\Delta - x) \pm 1}{\sqrt{x^2-1}\sqrt{(\hbar\omega_\nu/\Delta - x)^2 - 1}}. \tag{4.5}$$

where ω_ν is the frequency of the photon.

4.1.4 Stress-induced Quasiparticles

In addition to the pair-breaking energy introduced by the environment, e.g., high energy particle impacts and millimeter photons, one recent work argued that relaxation of thermally induced stress between the glue (thermal anchoring between the device and cold finger) and crystal (device substrate) is one possible source of phonon bursts which contributes to quasiparticle poisoning in superconducting quantum circuits [38].

4.1.5 Summary of Generation Mechanisms

Here, we summarize different origins of quasiparticle generation in Table 4.1.

4.2 Experimental Guides

In this section, we discuss, as a experimentalist, how to measure, inject, and suppress quasiparticles. At the end, we show the initial experiment of thermalization's effect

Table 4.1: **Quasiparticle generation mechanisms.**

Mechanisms	Notes	Reference
Thermal	$x_{\mathrm{qp}}^{\mathrm{th}} \approx \sqrt{2\pi k_{\mathrm{B}} T/\Delta} e^{-\Delta/k_{\mathrm{B}}T}$	[24]
High energy impacts	cosmic muon-rays and background radioactive source; burst events lead to correlated errors	[25, 26, 27]
Photon absorption	steady state quasiparticle poisoning; one dominant source for background quasiparticle density and qubit excitation error	[34, 35, 36, 37]
Stress-induced	relaxation of the stress	[38]

on quasiparticle poisoning.

4.2.1 Measure Quasiparticles

While quasiparticle poisoning is deleterious to the performance of superconducting quantum circuits, resonators and qubits are great quasiparticle sensors due to their sensitivity.

Resonators or microwave kinetic inductance detector (MKID) are developed for astronomy applications. This include high-sensitivity millimeter and sub-millimeter wave detection [39]. Pair-breaking photons are injected to MKIDs, breaking Cooper pairs and generating excess quasiparticles. The generated quasiparticles increase the kinetic inductance of the MKIDs, which can be measured from the microwave-based readout.

For the superconducting qubits, quasiparticles can induce qubit state transition, qubit frequency shift due to inductance shift, and charge parity jumps. There is also the famous Josephson cosine term [22]. The electrical properties of a junction can be modelled as a complex admittance that is both frequency- and phase-dependent

Table 4.2: **Quasiparticle measurement methods summary.**

Resonator	Notes	Ref
Frequency/phase shift	QP will shift resonator	[39, 44]
Quality factor decay	QP will decay resonator	[39]
Qubit	**Notes**	**Ref**
Energy relaxation		[30, 32]
Energy relaxation	phase dependence	[40]
Frequency shift	imaginary part of the junction admittance	[45, 46]
One state excitation	hot quasiparticles and photon-assisted	[43, 37]
Charge parity	charge sensitive transmon	[47]
Charge parity	charge insensitive transmon; use higher transitions with enough charge dispersion	[48, 49]
Charge parity	state transition dependence	[43]
Charge parity	phase dependence	[18]
Charge parity	$E_J/E_C < 20$; dispersive readout	[50, 36]

[40, 41]

$$Y(\omega,\phi) = Y_{qp}(\omega)\frac{1+\epsilon\cos\phi}{2} - i\frac{\cos\phi}{\omega L_J}(1-2x_{qp}^A), \tag{4.6}$$

where $Y_{qp}(\omega)$ is the quasiparticle admittance, ϵ is a prefactor close to 1 when $T \to 0$, L_J is the Josephson inductance, x_{qp}^A is the occupation of the Andreev bound states. At the qubit frequency, the quasiparticle leads to qubit relaxation, resulting in a reduced T_1 [30, 42]; the imaginary part of the admittance causes a the inductance shift of the junction, leading to a frequency shift of the qubit.

Hot non-equilibrium quasiparticles, not around the energy gap, can also excite the qubit, leading to excitation error and excess steady excited state occupation [43, 34, 37].

The charge sensitivity of transmon qubits are also utilized to measure quasiparticle induced charge-parity jumps of the qubit island.

All the above qubit's response to quasiparticle are summarized in the Table 4.2.

Table 4.3: **Quasiparticle suppression methods summary.**

Methods	Notes	Ref
Lead shield	reduce radiation	[51, 52]
Underground	reduce radiation	[51]
Eccosorb filters	inline IR filtering	[43, 36, 53, 54]
Dielectric low-pass filters	inline IR filtering	[55]
TE modes of coaxial cables	inline IR filtering	[54]
Qubit antenna mode design	reduce quasiparticle generation efficiency	[36, 37]
High-energy-gap-material-based junction	reduce quasiparticle generation efficiency	Future direction
Back-side normal metallization	phonon downversion	[56, 53]
Groundplane gap engineering	phonon/quasiparticle traps	[57, 58, 59]
Junction gap engineering	suppress quasiparticle tunneling	[60, 18]
Multi-chip module	phonon acoustic mismatch	[59]

4.2.2 Suppression of Quasiparticle Poisoning

After understanding the generation mechanisms and armed with various measurement methods, we explore the next important sub-field: suppressing quasiparticle poisoning of superconducting quantum devices. There are three main directions of quasiparticle poisoning mitigation. First, reduce the pair-breaking energy, e.g., high energy particles and pair-breaking photons, to reach the device. Second, suppress the superconducting circuits sensitivity to the environment noise, i.e., the conversion efficiency of pair-breaking energy to quasiparticles. Third, speed up quasiparticles relaxation and trapping once they are generated at the device level. Various quasiparticle suppression methods with physical implementation are summarized in Table 4.3.

Table 4.4: **Quasiparticle injection methods summary.**

Method	Notes	Ref
Thermal	elevate the temperature of the sample	[43, 36]
Broadband photon radiation	heat a blackbody close to the sample	[61, 18]
Narrowband photon radiation	ac Josephson oscillation through the antenna mode of the qubit	[37]
Normal branch of junction	bias NIS or SIS junction to normal branch	[62, 53]
Strong resonator drive	introduce ac voltage larger than energy gap	[63]
C_{64}	radioactive source	[52]

4.2.3 Inject Quasiparticles

To test the efficiency of the quasiparticle suppression implementation, we sometimes need to inject quasiparticles on purpose. We summarize the experimental methods in Table 4.4.

4.3 Sample Thermalisation

It is a mystery that how well our sample is thermalized to the sample holder and how long it takes for the sample to be thermalized to the base temperature once the dilution refrigerator reaches base.

We show some preliminary data about the thermalisation time. The data is taken from the Xmon qubit device used in [37] with single Al sample box mounted on Oxygen-free copper plate located at the mix chamber. The silicon chip is thermalized with Dow corning high vacuum grease at the sample box at the four corners. Three qubits' data is shown in Fig. 4.1. It is clear that the charge parity switch rate decreases to baseline level in order of 10 days. Between day 4 and 14, no data is acquired for this device.

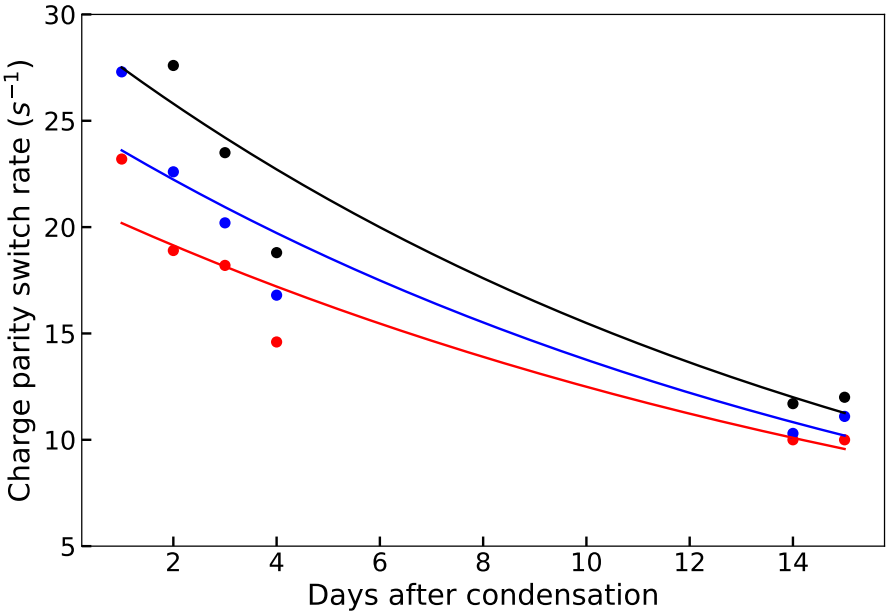

Figure 4.1: **Charge parity switch rate of three qubits after condensation (preliminary data).** The red, black, and blue dots are data for Q_1, Q_2, and Q_3, respectively. The lines are naive exponential fit to the data.

We have also tried using GE varnish to thermalize the same chip in the same sample holder. In this case, the charge parity switch rate saturates to a similar value $\sim 10\ s^{-1}$ in two days after condensation. It is notoriously known that thermalisation debugging is not trivial, so unfortunately we cannot make any conclusive argument here. It could be the materials we use for thermalisation matters; or in one cooldown, the fridge cooldown is significantly better or worse compared to the other due to thermal cycling.

Chapter 5

Quasiparticle Poisoning of Superconducting Qubits from Resonant Absorption of Pair-breaking Photons

The ideal superconductor provides a pristine environment for the delicate states of a quantum computer: because there is an energy gap to excitations, there are no spurious modes with which the qubits can interact, causing irreversible decay of the quantum state. As a practical matter, however, there exists a high density of excitations out of the superconducting ground state even at ultralow temperature; these are known as quasiparticles [24, 22]. Observed quasiparticle densities are of order 1 μm^{-3}, tens of orders of magnitude greater than the equilibrium density expected from theory [28, 29, 30, 31, 32, 33]. Nonequilibrium quasiparticles extract energy from the qubit mode and can induce dephasing. Here we show that a dominant mechanism for quasiparticle poisoning is direct absorption of high-energy photons

at the qubit junction [34, 35]. We use a Josephson junction-based photon source to controllably dose qubit circuits with millimeter-wave radiation, and we use an interferometric quantum gate sequence to reconstruct the charge parity of the qubit [47]. We find that the structure of the qubit itself acts as a resonant antenna for millimeter-wave radiation, providing an efficient path for photons to generate quasiparticles [35]. A deep understanding of this physics will pave the way to realization of next-generation superconducting qubits that are robust against quasiparticle poisoning. Part of this chapter and Chapter 6 have been submitted for publication in journal Physical Review Letters.

5.1 Introduction

In equilibrium, the ratio of thermally generated quasiparticles to Cooper pairs in a superconducting device is of order 10^{-50} at the millikelvin temperatures that are relevant for quantum computing and sensing applications. This is due to the exponential suppression of quasiparticle density with respect to Δ/T, where Δ is the superconducting gap energy and T is temperature. Experimentally, however, the ratio of quasiparticles to Cooper pairs is found to be between $\sim 10^{-6}$ and 10^{-10}, more than 40 orders of magnitude larger than expected from the equilibrium calculation. Nonequilibrium quasiparticles limit the sensitivity of superconducting devices for charge sensing [28, 64], metrology [65], and astrophysical observation [39, 66]. In the context of superconducting qubits, nonequilibrium quasiparticles represent a significant decoherence channel [30, 24, 31, 32, 33, 67, 43]. Recent experiments have demonstrated that quasiparticles liberated by particle impacts in the qubit substrate give rise to correlated relaxation errors in multiqubit arrays [25, 26, 27, 53]. While such errors are especially damaging for quantum error correction, the particle impact

rate is too low and the rate of removal of pair-breaking energy in the aftermath of an impact too high to account for the large baseline density of quasiparticles in superconducting quantum circuits.

Another potential source of quasiparticles is the absorption of pair-breaking photons. It has been shown that improvements in filtering and shielding can lead to enhanced energy relaxation times for superconducting resonators [68] and qubits [69]. Recently, Houzet *et al.* explained the observed ratio of the rate of charge-parity switches on the qubit island to the rate of qubit state transitions in terms of photon-assisted pair breaking at the Josephson junction [34]. In the Houzet model, coupling of the pair-breaking photon to the qubit junction is mediated by higher-order modes of the bulk 3D cavity in which the qubit is embedded. Our group has put forth an alternate model for the resonant absorption of photons by spurious antenna modes of the qubit that allows detailed calculation of the spectral response of the qubit to pair-breaking radiation [35]. The crucial insight is that the qubit structure itself exhibits a parasitic resonance at a frequency of order 100 GHz, set by the round-trip distance around the qubit island. This resonance is the aperture dual of the resonant wire loop antenna [70]. For typical qubit parameters, the qubit junction is well matched to free space impedance via this antenna mode, so that the qubit is an efficient absorber of pair-breaking radiation. Fig. 5.1a summarizes relevant quasiparticle generation and conversion mechanisms in superconducting qubits, while Fig. 5.1b depicts the dual mapping of aperture antenna to wire antenna.

In this article, we describe the experimental validation of our model for the antenna coupling of qubits to pair-breaking radiation. The experiments involve two separate chips that are housed in a single enclosure; one chip incorporates voltage-biased Josephson junctions that act as transmitters of coherent mm-wave photons, while the second chip supports multiple superconducting qubits that act as receivers.

We use a Ramsey-based interferometric gate sequence to monitor the charge-parity state of the qubits [47]; resonant absorption of pair-breaking photons induces parity switches on the qubit which we detect with near unit fidelity. By scanning the voltage bias of the transmitter junction, we map out the spectral response of the qubits up to ∼500 GHz. We find that the detailed absorption spectrum of the qubits agrees well with the predictions of our model. In addition, we find that the baseline quasiparticle poisoning rate (in the absence of mm-wave injection) can be explained in terms of the resonant absorption of blackbody photons from higher temperature stages of the cryostat. Finally, we show that spurious transitions of the qubit out of the ground state are dominated by the resonant absorption of pair-breaking photons. This detailed understanding of the physical mechanism for quasiparticle poisoning will allow realization of new qubit designs that are robust against pair-breaking radiation; additionally, it could form the basis for a new class of quantum sensors based on the transduction of photons to quasiparticles followed by subsequent qubit-based detection. We note that a recent experimental study explains the scaling of quasiparticle poisoning rate with qubit size in terms of our model, without direct validation of the detailed spectral response of the qubit devices [36].

5.2 Spurious Antenna Modes of the Qubit and Experiment Setup

The experimental setup is shown in Fig. 5.1c. Two separate device chips are integrated in a single light-tight enclosure made from 6061 aluminum: the transmitter chip (red) is mounted face to face with the receiver chip (blue) with a separation of 9.6 mm. For all devices described here, the chip is nearly completely covered by a niobium groundplane, and all Josephson elements are realized as Al-AlO_x-Al tunnel

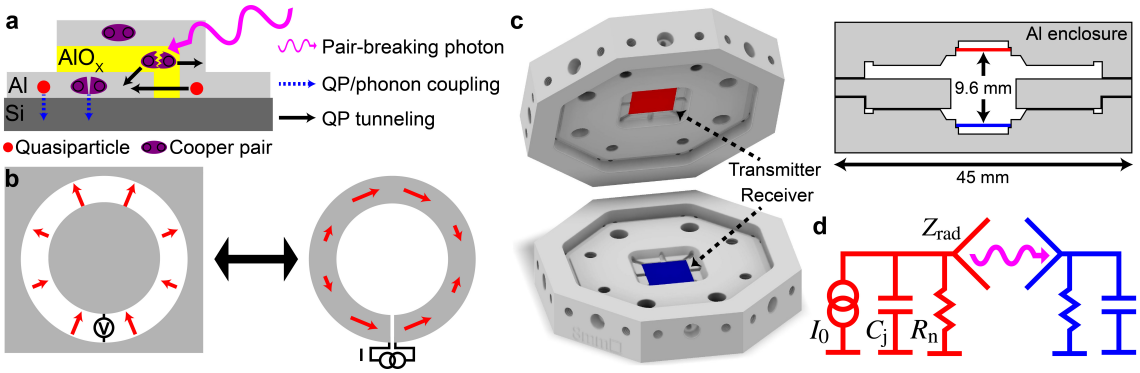

Figure 5.1: **Photon-assisted quasiparticle poisoning mediated by spurious antenna modes of the qubit.** **a**, Quasiparticle generation and conversion processes. Pair-breaking radiation is absorbed at a Josephson junction. Photon absorption changes the charge parity of the qubit island and can induce a qubit state transition. Quasiparticles couple to phonons through scattering and recombination. **b**, The single-ended circular transmon (left) is the aperture dual of the resonant wire loop antenna (right). Red arrows show the amplitude and direction of electric fields. In the aperture antenna, signal is coupled via a high-impedance source at the voltage antinode, while in the dual wire antenna signal is coupled via a low-impedance source at the current antinode [35]. **c**, Two-chip transmit/receive geometry used to probe the spectral response of the qubits to mm-wave radiation. Cutaway drawing to the right is a scale illustration of the aluminum sample enclosure. **d**, Circuit diagram for the transmit/receive experiment, with mm-wave Josephson transmitter depicted in red and receiver qubit depicted in blue.

junctions. We use a high-bandwidth 50 Ω line to bias the transmitter junction in the finite-voltage state; since the normal-state resistance of the junction is of order 10 kΩ, the bias line represents a stiff voltage source. Bias of the transmitter junction at voltage V induces coherent oscillations in the phase difference across the junction at the Josephson frequency $f_J = V/\Phi_0$, where $\Phi_0 \equiv h/2e$ is the magnetic flux quantum; for a 1 mV bias, the Josephson frequency is 484 GHz [71]. A circuit diagram of the experiment is shown in Fig. 5.1d. The voltage-biased junction can be modeled as a Norton equivalent current source I_0 in parallel with shunt admittance $Y_j \equiv 1/Z_j = 1/R_n + j\omega C_j$, where I_0 is the junction critical current, R_n is the junction normal-state resistance, and C_j is the self-capacitance of the junction. The Josephson oscillator acts as a source that drives the antenna formed by the junction pads

embedded in the circuit groundplane, with radiation impedance Z_{rad}. Following the analysis of [35], the power radiated to free space is given by

$$P_{\mathrm{rad}} = \frac{e_{\mathrm{c,tr}}}{8} I_0^2 R_{\mathrm{n}}, \tag{5.1}$$

where I_0 and R_{n} are the transmitter junction critical current and normal-state resistance, respectively, and where the coupling efficiency $e_{\mathrm{c,tr}}$ of the junction to free space is given by

$$e_{\mathrm{c,tr}} = 1 - \left| \frac{Z_{\mathrm{rad}} - Z_{\mathrm{j}}^*}{Z_{\mathrm{rad}} + Z_{\mathrm{j}}} \right|^2 . \tag{5.2}$$

Power emitted into the shared cavity will populate the enclosure with coherent mm-wave radiation; due to multiple reflections from the enclosure walls, we expect the distribution of energy in the enclosure to be isotropic with random polarization (see Sec. 6.5 for additional details).

We now consider the effect of the radiation on the transmon qubits of the receiver chip. The devices were designed with ratio $E_{\mathrm{J}}/E_{\mathrm{c}}$ of Josephson energy to single-electron charging energy around 25, so that the qubit 01 transition frequency is weakly sensitive to offset charge on the qubit island, with peak-to-peak charge dispersion $2\delta f$ of order 1 MHz.

This makes it possible to monitor quasiparticle poisoning events in real time by using a Ramsey gate sequence that maps charge parity to qubit state occupation (see Sec. 6.4 for more details). As acoustic coupling between the transmitter and receiver chips is negligible, the transfer of energy from chip to chip proceeds via the emission and absorption of photons. Photons with frequency $f > 2\Delta_{\mathrm{Al}}/h = 92$ GHz couple to the Josephson junction of the receiver qubit with efficiency $e_{\mathrm{c,rec}}$ defined as in Eq. 5.2. Photon absorption breaks a Cooper pair: two quasiparticles are generated, one on either side of the junction, resulting in a change in the charge parity of the

qubit island.

5.3 Spectral Response of the Xmon Qubit

In a first series of experiments, we employ two nominally identical chips as transmitter and receiver. Witness junctions arrayed around the perimeter of the chip are used as mm-wave transmitters; the geometry is shown in Fig. 5.2a. One pad of the transmitter is connected to the chip groundplane via a short wirebond, while the opposite pad is bonded to the 50 Ω bias line [1]. The chip incorporates six Xmon qubits, each with a local readout resonator coupled to a common feedline; the qubit geometry is shown in Fig. 5.2b. As we vary the voltage bias on the transmitter junction and thus the frequency of the emitted Josephson radiation, we use the parity-sensitive Ramsey sequence to probe the charge parity of the receiver qubit at a sampling rate of 20 kHz. In the following, we present data on a single transmitter/receiver pair, although all three of the receiver qubits studied on this chip displayed a similar spectral response (see Sec. 6.6 for more details). All experiments were conducted at the 16 mK base temperature of a closed-cycle dilution refrigerator.

In Fig. 5.2c, we show the calculated coupling efficiencies e_c for the transmitter (red) and receiver (blue) structures; see Sec. 6.5 for details of the calculation. The purple trace, obtained as the product of the transmitter and receiver efficiencies, represents the frequency-dependent transfer function of the two-chip experiment in the absence of loss and additional nonidealities. In Fig. 5.2d, we plot the measured parity switching rate Γ_p of the receiver qubit versus transmitter Josephson frequency (black points). We observe clear peaks in the spectral response of the receiver

[1] Detailed modeling of the chip geometry using CST Microwave reveals that loading of the transmitter antenna with the wirebond and 50 Ω drive line only slightly modifies the radiation impedance of the structure.

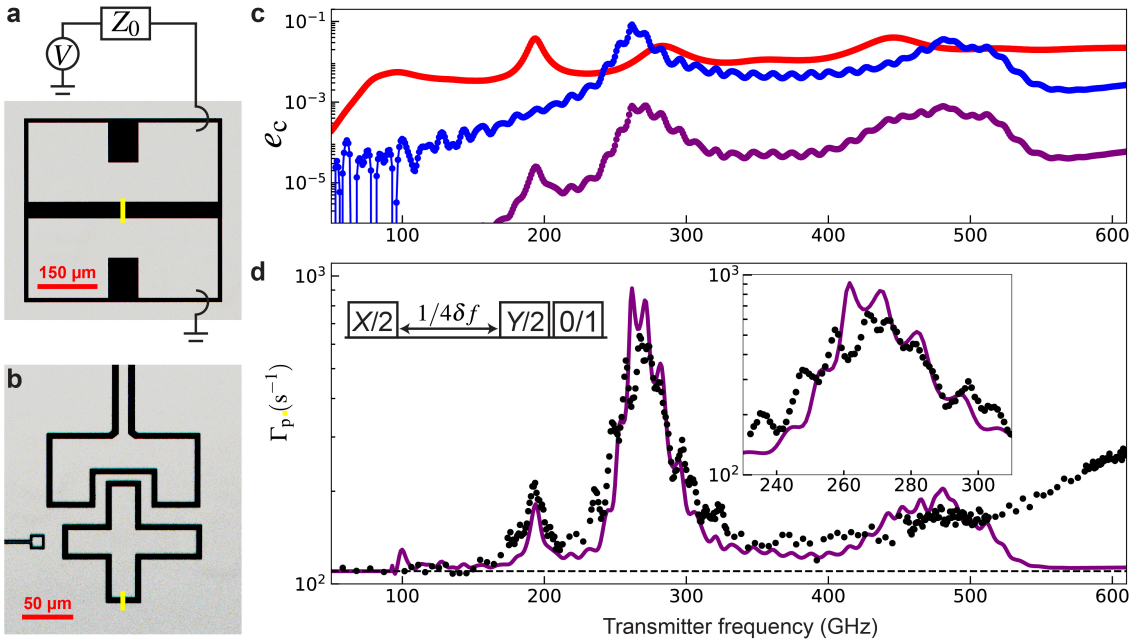

Figure 5.2: **Spectral response of the Xmon qubit.** **a**, Optical micrograph of the Josephson transmitter. Voltage bias is provided by a high-bandwidth line with impedance $Z_0 = 50\,\Omega$. **b**, Optical micrograph of the Xmon receiver qubit. Local charge gate is shown at left and coupling capacitor to the readout resonator is shown at top. In both (a) and (b), junction leads are shown in yellow. **c**, Frequency-dependent coupling efficiency calculated for the transmitter junction (red) and receiver qubit (blue). The purple trace, obtained as the product of these coupling efficiencies, represents the overall transfer efficiency from transmitter to receiver in the absence of losses and other nonidealities. See Sec. 6.5 for details of the calculation. **d**, Quasiparticle poisoning rate as a function of transmitter frequency. Left inset shows the parity-sensitive Ramsey sequence. Black points are the measured poisoning rates; the black dashed line is the baseline rate $\Gamma_0 = 110\ \mathrm{s}^{-1}$ (in the absence of explicit photon injection); and the purple trace is the contribution from Josephson radiation calculated from the coupling efficiencies of (c), with an overall scaling of 0.07 to account for photon losses. The right inset shows a detailed view of the resonant features around 270 GHz. Oscillations in the spectral response of the qubit arise from the mutual coupling of the qubit antenna mode to a spurious slotline mode of the qubit readout resonator.

qubit at 190 GHz and 270 GHz, with Γ_p a factor of 2 and 6 times larger than the baseline rate of 110 s^{-1}, respectively. We ascribe these features to antenna resonances in our Josephson transmitter and receiver qubit, which provide enhanced transfer of Josephson energy between the two chips. The solid purple trace represents

the expected parity switching rate calculated from the device coupling efficiencies. Detailed modeling of the two-chip experiment incorporates several effects, including quasiparticle-induced suppression of the critical current of the transmitter junction and randomization of the direction and polarization of the emitted radiation due to multiple reflections from the walls of the cavity enclosure; for a detailed discussion, see Sec. 6.5. The model clearly captures the dominant resonant features of the parity spectrum; however, to obtain good agreement between the measured and expected parity switching rates, we must scale the expected rates by a factor of 0.07. The discrepancy in the absolute rates could be due to dielectric losses or to enhanced loss of photons that are initially emitted into the silicon substrate of the transmitter, as the near-continuous superconducting Nb groundplane of the transmitter chip will act as a barrier to transport of photons into the shared space of the two-chip enclosure.

In the inset of Fig. 5.2d, we plot on an expanded scale the measured and calculated parity switching rates. We observe clear fine structure in both the measured and calculated spectra, with a modulation of the receiver response at a period of 11 GHz. We understand this modulation to be due to the mutual coupling between the receiver qubit and its local readout resonator, which involves a spurious $\lambda/2$ slotline mode at a frequency that is roughly twice that of the $\lambda/4$ coplanar waveguide resonance at 6.058 GHz. We take the excellent agreement between the measured and calculated fine structure of the parity spectra as clear validation of our antenna model for coupling of the qubit to pair-breaking radiation.

For transmitter bias above 1 mV, corresponding to Josephson frequency above 500 GHz, we observe an upturn in the measured parity switching rate that is not captured by our modeling. We ascribe this feature to the exchange of energy between the chips due to the incoherent emission of photons from the recombination of quasiparticles in the leads of the transmitter junction; detailed modeling of this

physics is the subject of ongoing work.

Two additional qubits on the receiver chip were examined during the same cooldown (see Sec. 6.6). Both of these devices displayed baseline parity switching rates and spectral responses within 10% of those measured on the device described here, despite different separation and relative orientation with respect to the transmitter junction. This observation lends support to our assumption that the experiment can be modeled in terms of an isotropic distribution of radiation in the shared cavity with random polarization.

5.4 Dependence of Resonant Response and Baseline Parity Switching Rate on Device Scale

In a second series of experiments, we examined the resonant response of receiver qubits with circular island geometry spanning a range of sizes; the geometries of the transmitter junction and the three receiver qubits (Q_1, Q_2, and Q_3) are shown in Fig. 5.3a. The devices are designed with the same nominal charging energy $E_c/h = 360$ MHz and ratio $E_J/E_c = 28$; however, the different island radii 90, 70, and 50 μm yield different dominant dipole antenna resonances at frequencies 130, 240, and 360 GHz, as confirmed by numerical modeling of the chip (Fig. 5.3b).

With the Josephson radiator turned off, we first measure the baseline parity switching rates on the three devices (dashed lines in Fig. 5.3c), finding $\Gamma_0(Q_1) = 1060$ s^{-1}, $\Gamma_0(Q_2) = 190$ s^{-1}, and $\Gamma_0(Q_3) = 12.8$ s^{-1}. The two orders of magnitude discrepancy in the baseline parity switching rates across these devices indicates clearly that nonequilibrium quasiparticles are not uniformly distributed on the receiver chip, and that device geometry plays a critical role in the generation of quasiparticles. If we take the radiative environment of the qubit to be a blackbody at effective tempera-

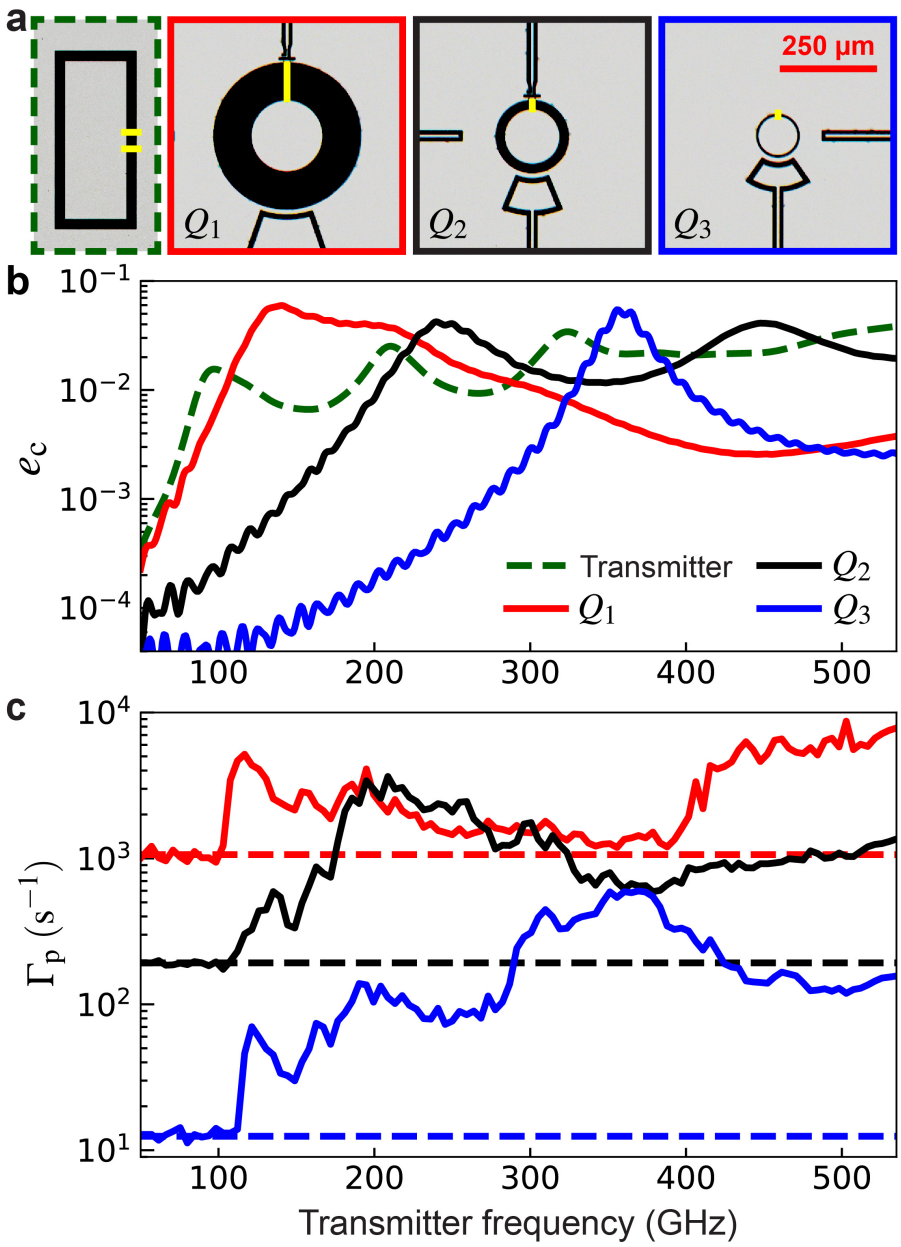

Figure 5.3: **Dependence of resonant response and baseline parity switching rate on device scale. a**, Optical micrographs of the rectangular transmitter device (green) and the large (red), intermediate (black), and small (blue) circmon qubits used for these experiments. Yellow traces indicate the junction leads. **b**, Calculated coupling efficiencies of the transmitter and the three circmon receiver qubits. **c**, Measured quasiparticle poisoning rates for the three qubits of as a function of transmitter frequency. Dashed lines indicate the baseline parity switching rates measured in the absence of photon injection.

ture T and assume coupling of the qubit antenna to a single mode and polarization of the radiation field, we find a rate of absorption of pair-breaking photons given by

$$\Gamma_0 = \int \frac{e_c}{e^{hf/k_B T} - 1}\, df. \tag{5.3}$$

From the measured parity switching rates on the three devices, we infer effective blackbody temperatures $T(Q_1) = 410$ mK, $T(Q_2) = 490$ mK, and $T(Q_3) = 460$ mK. We believe that the broadband pair-breaking photons giving rise to the observed parity jumps are not due to a single radiator at a physical temperature of 400-500 mK, but rather due to light leakage from higher temperature stages of the refrigerator (most likely via the coaxial wiring) that is insufficiently attenuated by the in-line Eccosorb filters [72, 50]. There is no reason to expect the spectrum of leakage radiation to follow that of an ideal blackbody; the discrepancy in the effective temperatures inferred for the three qubit antenna modes could reflect structure in the environmental spectrum.

With the transmitter junction biased in the voltage state, we map out the resonant response of these three devices using the parity spectroscopy technique described above; the data are shown in Fig. 5.3c. The complex resonant structure of the transmitter mode leads to rich structure in the resonant response of the three qubits; however, the measured parity switching rates are in qualitative agreement with our antenna model, with the resonant response shifting to higher frequency as the radius of the qubit island decreases.

5.5 Photon-Assisted Parity Switches and Qubit Transitions

Finally, using Q_2 as a testbed, we examine spurious transitions out of the qubit $|0\rangle$ state induced by the absorption of pair-breaking photons. We measure the transition rate directly, using a $measure - idle - measure$ sequence (inset in Fig. 5.4a), with the pre-measurement providing a high-fidelity initialization in the qubit $|0\rangle$ state. In Fig. 5.4a we show representative data for the conditional probability $P_1 \equiv P(1|0)$ of finding the qubit in state $|1\rangle$ in the second measurement given that the initial measurement prepared state $|0\rangle$. A linear fit to the plot of P_1 versus idle time Δt yields the upward transition rate $\Gamma_\uparrow$. In Fig. 5.4b, the solid traces show the measured parity switching rate Γ_p and upward transition rate $\Gamma_\uparrow$ versus Josephson frequency of the transmitter junction. We see that Γ_p and $\Gamma_\uparrow$ display a similar resonant response centered at a Josephson frequency around 240 GHz, where the transfer function from transmitter to receiver device is expected to peak. Moreover, the ratio $\Gamma_\mathrm{p}/\Gamma_\uparrow$ is roughly constant over the full frequency range, indicating that qubit transitions out of the ground state are dominated by resonant absorption of pair-breaking photons. Houzet *et al.* have previously analyzed the rate of qubit transitions conditioned on the absorption of a pair-breaking photon [34]. Their analysis predicts a contribution to $\Gamma_\uparrow$ given by the dashed blue trace in Fig. 5.4b (see Sec. 6.7). However, the absorption of a pair-breaking photon will also generate a steady-state population of nonequilibrium quasiparticles that can tunnel across the qubit junction, inducing additional qubit transitions following the primary poisoning event. It is possible that this secondary poisoning process accounts for the enhanced rate of upward transitions measured here. While we expect a small contribution to qubit relaxation from the absorption of pair-breaking photons, this contribution is

not possible to access experimentally against the baseline relaxation rate of order 10^5 s^{-1}.

5.6 Conclusion

In summary, we have used controlled irradiation of superconducting qubits with mm-wave photons derived from the ac Josephson effect to validate a model for photon-assisted quasiparticle poisoning through the spurious antenna modes of the transmon qubit. The observed baseline parity switching rates are well explained by absorption of broadband thermal photons from higher temperature stages of the cryostat. Additionally, the correlation between qubit state transitions and charge parity switches indicates that resonant absorption of pair-breaking photons is the dominant contributor to qubit initialization errors in our devices.

An understanding of the physical origin of quasiparticle poisoning will allow the development of improved qubit designs and measurement configurations that protect against absorption of pair-breaking radiation. At the same time, the resonant transduction of pair-breaking photons to quasiparticles followed by qubit-based parity detection could form the basis for a new class of quantum sensors; potential applications include high-resolution spectroscopy of the cosmic microwave background [73] or detection of dark-matter axions [74, 75] or dark energy [76] in the frequency range from 100 GHz to 1 THz, where established detection techniques are limited.

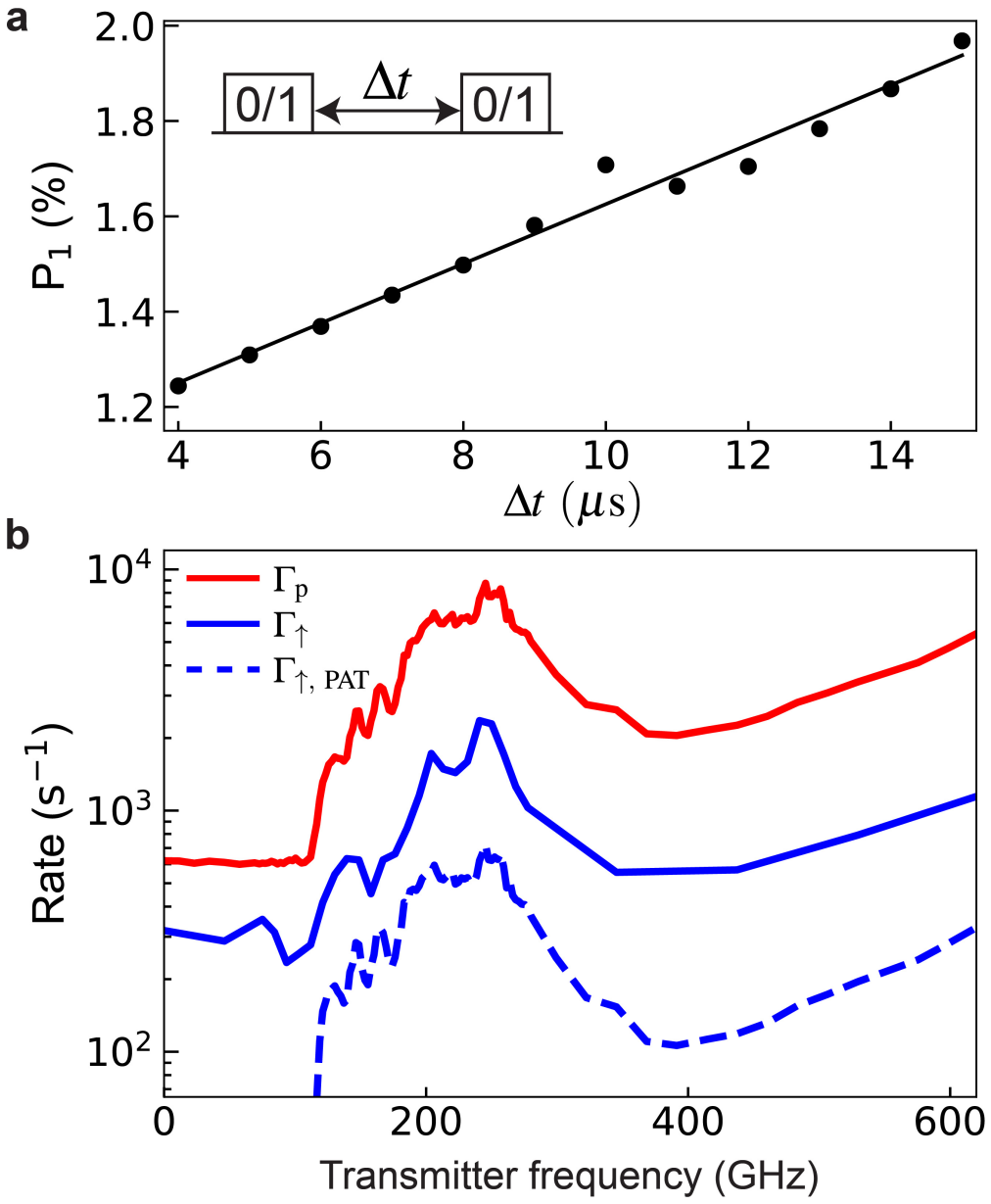

Figure 5.4: **Photon-assisted parity switches and qubit transitions. a**, Representative measurement of qubit excitation rate. Here we use circmon qubit Q_2 as a testbed. Inset shows the *measure* − *idle* − *measure* sequence. A linear fit (black line) is used to extract the upward transition rate. **b**, Measured quasiparticle poisoning rate (red) and upward transition rate (blue solid trace) as a function of transmitter frequency. The dashed curve shows the predicted photon-assisted qubit transition rate calculated from the measured rate of parity switches, after [34]. See Sec. 6.7 for the details of the transmitter used in these experiments.

Chapter 6

Supplemental Information for "Quasiparticle Poisoning of Superconducting Qubits from Resonant Absorption of Pair-breaking Photons"

6.1 Device Fabrication

The devices were fabricated in a single-layer process on a high-resistivity silicon substrate (>10 kΩ-cm) with 100 crystal orientation. Following a strip of the native SiO_x in dilute (2%) hydrofluoric acid for 1 minute, we sputter a 100-nm thick Nb film at a rate of 50 nm/minute. (In the case of the Xmon qubits, the Nb film thickness is 70 nm). We use an i-line stepper to define the qubit islands, resonators, and control wiring. Next, we etch the Nb using Cl_2/BCl_3 chemistry in an inductively coupled

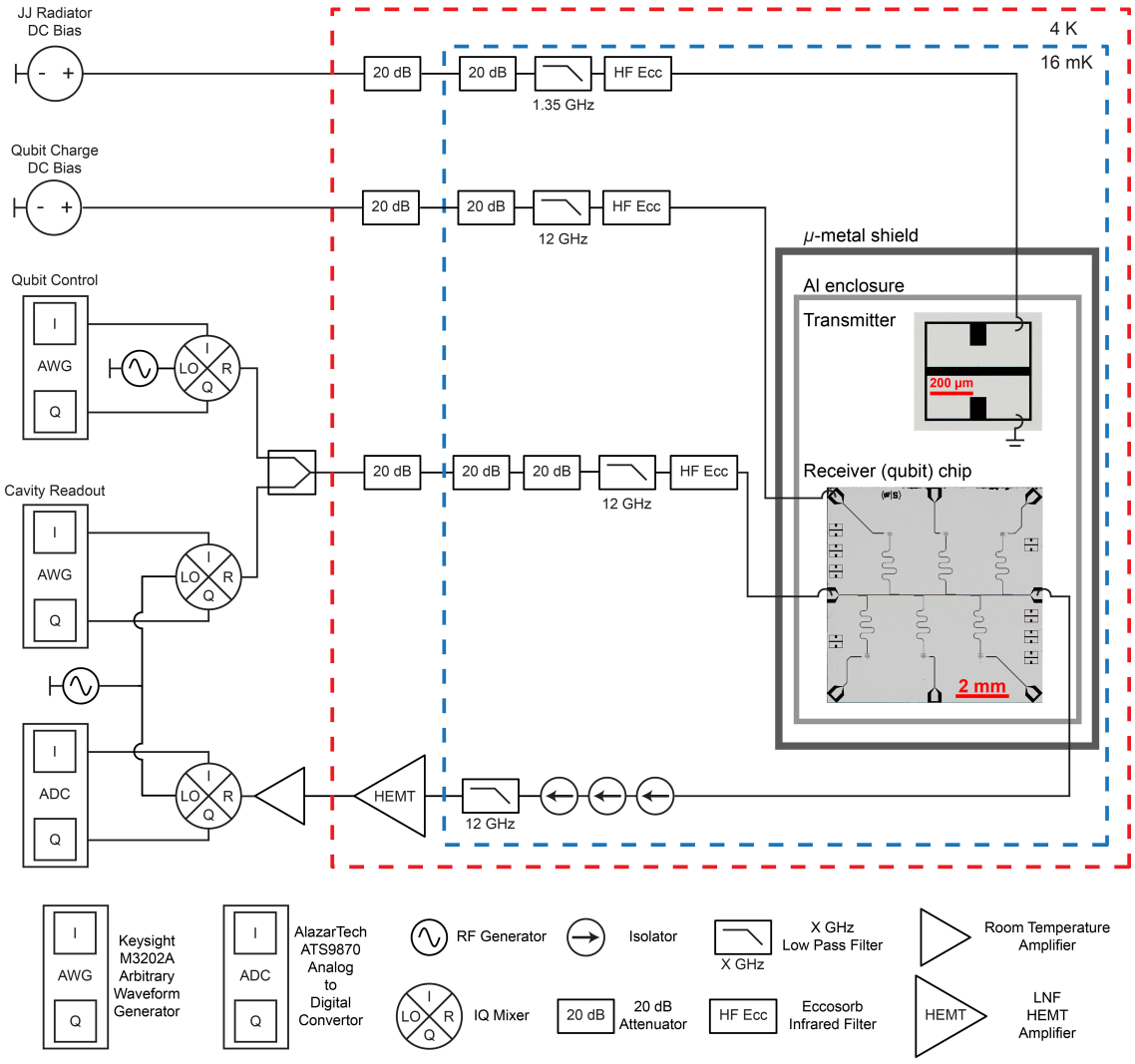

Figure 6.1: **Wiring diagram of the experiments.**

plasma reactive ion etch tool.

6.2 Experimental Setup

The experimental wiring configuration is shown in Fig. 6.1.

Table 6.1: **Parameters of qubits used in the experiments.** Qubit frequency f_{01} and peak-to-peak charge dispersion $2\delta f$ are measured by qubit spectroscopy. Ratio E_J/E_c of Josephson energy to charging energy ratio is calculated from the measured qubit transition frequency and charge dispersion. The junction normal state resistance R_n is calculated from the extracted Josephson energy. The junction self-capacitance is obtained from the junction area measured from SEM and a nominal junction specific capacitance of 75 fF/μm^2. The frequency f_{ant} of the fundamental antenna resonance of the qubit is determined from the qubit antenna impedance calculated using a finite element solver and from the frequency-dependent junction impedance. The baseline quasiparticle poisoning rate Γ_0 is measured in the absence of explicit photon injection.

Xmon	f_{01} (GHz)	$2\delta f$ (MHz)	E_J/E_c	R_n (kΩ)	C_j (fF)	f_{ant} (GHz)	Γ_0 (s^{-1})
Q_1	4.828	4.6	22	17.1	4.6	280	85
Q_2	4.782	2.7	24	16.6	4.6	270	110
Q_3	4.829	2.1	25	16.1	4.6	270	103
Circmon	f_{01} (GHz)	$2\delta f$ (MHz)	E_J/E_c	R_n (kΩ)	C_j (fF)	f_{ant} (GHz)	Γ_0 (s^{-1})
Q_1	4.595	1.5	26	16.6	3.5	130	1060
Q_2	4.949	1.1	28	15.0	3.2	240	190
Q_3	4.443	0.8	29	13.2	3.4	360	12.8

6.3 Qubit Parameters

In Table 9.1, we list the measured and extracted parameters of the qubits used in these experiments.

6.4 Charge Parity Measurement

We use the weakly charge-sensitive transmon to probe charge parity fluctuations. The devices are designed with $E_J/E_c = 20-30$, where E_J is the Josephson energy of the qubit junction and E_c is the single-electron charging energy of the qubit island, yielding a peak-to-peak charge dispersion of the qubit 01 transition around 1 MHz. In the following, we present data from circmon qubit Q_2 (described in Figs. 5.3 and 5.4 of the main text) as an example. For this device, $E_J/E_c = 28$.

In Fig. 6.2a, we show qubit spectroscopy versus applied gate charge. We observe

two clear charge parity bands that oscillate sinusoidally with gate charge, with a maximum dispersion $2\delta f = 1.1$ MHz. To probe charge parity, we perform a series of charge-sensitive Ramsey scans at different applied charge biases in order to determine the offset charge on the qubit island; we then dynamically set the qubit charge bias to the point of maximum charge dispersion. We next apply a parity-sensitive $X/2 - idle - Y/2$ Ramsey sequence to map charge parity to qubit population (Fig. 6.2b inset). We repeat the parity measurement sequence 5000 times with a duty cycle $\Delta t = 50$ μs to obtain a time series of charge parity. We repeat this experiment (including charge reset) 9 times, and from the separate time series we compute an average power spectral density S_{P} of charge parity fluctuations; representative data is shown in Fig. 6.2b. The power spectrum is fit using the Lorentzian form:

$$S_{\mathrm{P}}(f) = \frac{4F^2\Gamma_{\mathrm{p}}}{(2\Gamma_{\mathrm{p}})^2 + (2\pi f)^2} + (1 - F^2)\Delta t, \tag{6.1}$$

where F is the sequence mapping fidelity. From the fit, we extract the average parity switching rate Γ_{p}.

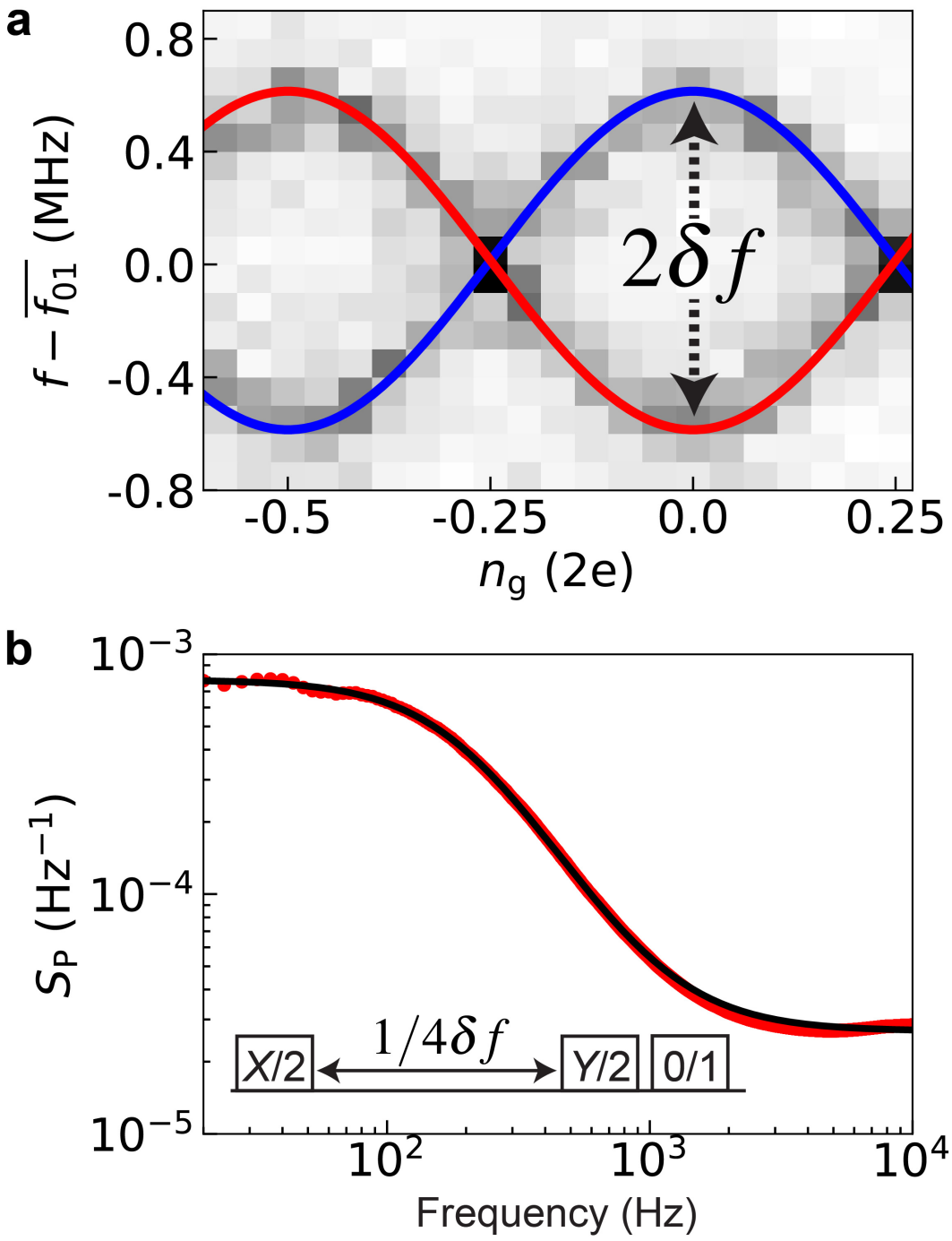

Figure 6.2: **Charge parity switching measurement.** **a**, Spectroscopy of the charge-sensitive transmon versus applied offset charge n_g. Solid traces correspond to even and odd charge parity bands. Here we have maximum charge dispersion $2\delta f$ =1.1 MHz. **b**, Power spectral density of charge-parity switches (red dots). The Lorentzian fit (black trace) corresponds to a parity switching rate $\Gamma_p = 612$ s^{-1}. Inset shows the Ramsey sequence used to map charge parity to qubit population.

6.5 Analysis of Transmit/Receive Experiment

Here we analyze the efficiency with which our transmitter and receiver devices are coupled to free space, and we put forth a simple model for estimating the circulating power in the shared cavity of the two chips. The analysis is focused on the transmit/receive experiment described in Fig. 5.2 of the main text.

6.5.1 Coupling Efficiency

The single-ended planar qubit can be viewed as an aperture antenna loaded with a Josephson junction; see Fig. 6.3a. The junction is modeled as the parallel combination of tunnel resistance R_{n} and junction self-capacitance C_{j}; see Fig. 6.3b. The frequency-dependent impedance of the junction is given by

$$Z_{\mathrm{j}} = \frac{1 - j\omega\tau}{1 + \omega^2\tau^2} R_{\mathrm{n}}, \tag{6.2}$$

where $\tau \equiv R_{\mathrm{n}} C_{\mathrm{j}}$. The impedance of the aperture antenna Z_{rad} is obtained from the finite element software CST Studio Suite [1]. Here we use the design of Q_2 from the Xmon experiment as an example. In Fig. 6.3c-d, we plot the real and imaginary parts of Z_{rad} and Z_{j}^*. The coupling efficiency e_c is given as

$$e_{\mathrm{c}} = 1 - \left| \frac{Z_{\mathrm{rad}} - Z_{\mathrm{j}}^*}{Z_{\mathrm{rad}} + Z_{\mathrm{j}}} \right|^2. \tag{6.3}$$

Optimal power transfer is achieved when the conjugate matching condition is satisfied: $Z_{\mathrm{rad}} = Z_j^*$. The coupling efficiency of Q_2 is shown in Fig. 6.3e. For our transmit/receive experiments, the coupling efficiency of the transmitter junction $e_{\mathrm{c,tr}}$ is calculated in the same way.

[1] CST Studio Suite, www.3ds.com.

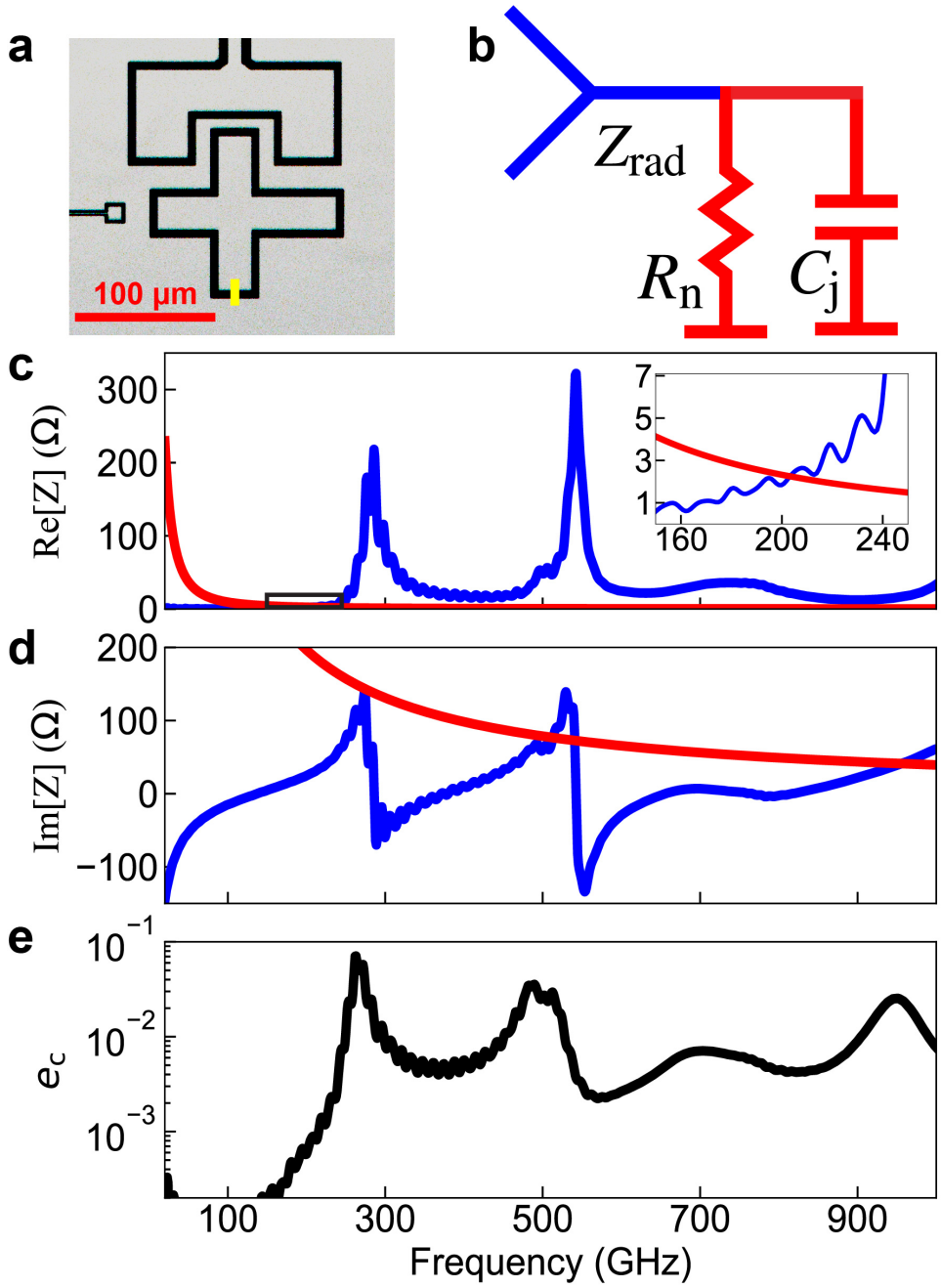

Figure 6.3: **Power match to the qubit antenna mode.** **a**, Single-ended Xmon from Fig. 5.2b of the main text. The X-shaped qubit island is connected to ground by a Josephson junction (junction leads indicated in yellow). **b**, Equivalent circuit diagram for qubit junction (modeled as a parallel RC circuit, red) embedded in an aperture antenna (blue). **c**, Real and **d**, imaginary parts of the conjugate of the junction impedance Z_j^* (red) and antenna impedance Z_{rad} (blue). Z_j is calculated from Eq. 6.2, while Z_{rad} is calculated using CST Studio Suite, www.3ds.com. The inset in **c** shows an expanded view of the real part of the impedance from 160 to 240 GHz. **e**, Frequency-dependent coupling efficiency e_c calculated from Eq. 5.2.

6.5.2 Radiation from the Transmitter

The power emitted from the transmitter junction due to Josephson oscillations is given by

$$P_{\mathrm{rad}} = P_{\mathrm{in,tr}} e_{\mathrm{c,tr}}, \tag{6.4}$$

where $e_{\mathrm{c,tr}}$ is calculated as in Eq. 5.2 from the main text, and where

$$P_{\mathrm{in,tr}} = \frac{1}{8} I_0^2 R_{\mathrm{n}} \tag{6.5}$$

is the maximum available power. Here, one factor of 1/2 comes from averaging over the full period of the Josephson oscillation, and a factor of 1/4 comes from the 1:1 current division between the Josephson source and a matched load. Bias of the transmitter junction above the gap leads to injection of quasiparticles in the junction leads; in the presence of reduced quasiparticle density x_{qp}, we have

$$I_0(x_{\mathrm{qp}}) = I_0(0)(1 - x_{\mathrm{qp}}), \tag{6.6}$$

where $I_0(0)$ is the junction critical current in the absence of quasiparticle poisoning [45]. For the bias regime studied here, we find that quasiparticle poisoning leads to a suppression of transmitter junction critical current of order 10%, with a weak dependence on bias voltage out to a Josephson frequency of ∼500 GHz.

At higher bias voltage, the quasiparticle density in the junction leads increases sharply and eventually saturates due to quasiparticle-induced suppression of the energy gap. For bias of the transmitter junction at Josephson frequency > 500 GHz, we observe an upturn in measured quasiparticle poisoning rate that is not captured by our antenna model. One potential explanation for this upturn is emission of thermal radiation due to Joule heating in the transmitter junction electrodes. However,

a naive quantitative analysis suggests that this mechanism is insufficient to account for the observed behavior. To model this possibility, we make the extreme assumption that the Al leads of the transmitter junction are driven into the normal state and dissipate the entire input power from the junction $P = V^2/R_n$. The electron temperature T_e can then be computed from the hot electron model described in [77]: $T_e = \left(P/\Sigma\Omega + T_p^5\right)^{1/5}$, where $\Sigma = 0.2$ nW/K^5/μm^3 is the electron-phonon coupling parameter [78], $\Omega = 2.8$ μm^3 is the volume of the junction leads, and $T_p = 20$ mK is the phonon reservoir temperature, resulting in

$$T_e \approx 580 \text{ mK}. \tag{6.7}$$

If we then apply T_e as the temperature in the usual Stefan-Boltzmann law, using 24 μm^2 as the surface area of the junction leads and taking unit emissivity, the radiated power from the junction electrodes is

$$P_{\text{bb}} \approx 1.5 \times 10^{-19} \text{ W}. \tag{6.8}$$

Of course, this power is emitted across a broad bandwidth, over which the receiver antenna coupling efficiency e_c varies considerably from its peak value at 270 GHz. We can take as a point of reference the $\sim$600 s^{-1} increase in charge-parity rate induced by Josephson radiation from the transmitter junction for bias at the peak of the resonant response of the qubit. From Eq. 6.4, we find:

$$P_{\text{J}}(270 \text{ GHz}) \approx 3 \times 10^{-16} \text{ W}. \tag{6.9}$$

Even under the assumption that the receiver coupling efficiency is maintained at its peak value across the entire bandwidth of the blackbody emission from the transmit-

ter, we see that thermal emission from the transmitter leads will result in an increase in charge-parity rate given by $[P_{\mathrm{bb}}/P_{\mathrm{J}}(270\ \mathrm{GHz})] \times 600\ \mathrm{s}^{-1} = 0.3\ \mathrm{s}^{-1}$. However, the measured increase in charge-parity rate at high transmitter bias is 100 to 200 s^{-1} above the baseline. This discrepancy of nearly three orders of magnitude underscores the implausibility of the blackbody radiation mechanism.

An alternate explanation involves the incoherent emission of pair-breaking photons from quasiparticle recombination in the transmitter junction leads. The reverse process, namely quasiparticle generation via absorption of pair-breaking photons, is well studied; moreover, we expect the resonant antenna mode of the transmitter junction to lead to enhanced photon emission at mm-wave frequencies [42]. Detailed modeling of this physics is the subject of ongoing work.

6.5.3 Absorption by Receiving Antenna

To calculate the rate of absorption of pair-breaking photons by the qubit, we need to know the circulating power in the shared aluminum enclosure of the transmit/receive experiment for a given applied bias (see Fig. 5.1c). To perform a naive estimate, we consider the case where absorption of Josephson radiation in the aluminum walls of the shared enclosure is the dominant source of photon loss. The circulating power can then be obtained from a simple power balance: the power radiated by the transmitter (Eq. 6.4 above) must equal the power absorbed by the aluminum. We assume that photons from the transmitter will reflect many times within the enclosure prior to absorption and that these reflections randomize the direction and polarization of the Josephson radiation, creating an isotropic distribution of radiation with random polarization. The fact that the measured quasiparticle poisoning rate does not depend on separation and relative orientation of the transmitter and receiver devices lends support to this assumption (see Fig. 6.4).

Table 6.2: **Parameters used for calculation of the expected rate $\Gamma_{\mathrm{J,theo}}$ of parity switches in the experiment of Fig. 5.2d.** The critical current without quasiparticle suppression is calculated from R_{n} using the Ambegaokar-Baratoff relation [80]; the suppression of I_0 due to local quasiparticle injection is extracted from a simple rate equation [32] using the reduced quasiparticle recombination rate (438 ns)$^{-1}$ [81].

Parameter	value	source
Al conductivity σ_{Al}	7.2×10^7 S/m	[79]
Enclosure inner area A_{enc}	3.2×10^{-3} m^2	design
Transmitter junction R_{n}	33.0 kΩ	RT 4-wire probe
Transmitter junction I_0	8.3 nA	see caption

The power P_{enc} absorbed by the aluminum enclosure is given by

$$P_{\mathrm{enc}} = \pi \eta S A_{\mathrm{enc}}, \tag{6.10}$$

where $\eta = 1 - \left|\frac{Z_{\mathrm{Al}} - Z_{\mathrm{fs}}}{Z_{\mathrm{Al}} + Z_{\mathrm{fs}}}\right|^2$ is the efficiency with which photons are absorbed by the aluminum enclosure, S is the incident power per unit solid angle per unit area, and A_{enc} is the inner area of the enclosure (the factor π comes from integrating the cosine of the polar angle over the half-space). Here, $Z_{\mathrm{fs}} = 377\ \Omega$ is the impedance of free space and Z_{Al} is the surface impedance of aluminum:

$$Z_{\mathrm{Al}} = (1 + j)\sqrt{\frac{\omega \mu_0}{2\sigma_{\mathrm{Al}}}}, \tag{6.11}$$

where μ_0 is the permeability of free space and where for σ_{Al} we take the conductance of aluminum 6061 at 4 K [79]; see Table 6.2.

For isotropic coherent radiation with wavelength λ, the power absorbed by the receiving antenna is

$$P_{\mathrm{rec}} = \frac{1}{2} S \lambda^2 e_{\mathrm{c,rec}}, \tag{6.12}$$

where the factor 1/2 accounts for random polarization of the radiation field. The rate

Table 6.3: **Transmit/receive experiment: comparison between naive model and measurement.**

f_J	$\Gamma_{J,\ theo}$	$\Gamma_{J,\ meas}$	$\Gamma_{J,\ meas}/\Gamma_{J,\ theo}$
190 GHz	1020 s^{-1}	103 s^{-1}	0.10
270 GHz	11400 s^{-1}	528 s^{-1}	0.05

of absorption of photons from the Josephson radiation field is then $\Gamma_J(f) = P_{rec}/hf$.

6.5.4 Summary and Comparison with Measurement

Collecting the various pieces, we arrive at the following expression for the expected rate of photon absorption at the receiver antenna, within our simple model:

$$\Gamma_{J,\ theo}(f) = \frac{e_{c,tr}\, e_{c,rec}}{16\eta} \frac{\lambda^2}{A_{enc}} \frac{I_0^2 R_n}{hf}. \tag{6.13}$$

In Table 6.2, we provide numerical values for the various quantities involved in this expression (the calculated coupling efficiencies $e_{c,tr}$ and $e_{c,rec}$ are presented in Fig. 5.2 of the main text).

The measured rate Γ_p of parity switches can be broken into two parts:

$$\Gamma_p(f) = \Gamma_0 + \Gamma_J(f). \tag{6.14}$$

Here, the baseline parity switching rate Γ_0 accounts for quasiparticle poisoning induced by broadband radiation from higher temperature stages of the cryostat, while $\Gamma_J(f)$ is the contribution from Josephson radiation emitted by the transmitter junction.

In Table 6.3 we compare the expected rate $\Gamma_{J,theo}$ of parity switches induced by Josephson oscillations to the measured rate $\Gamma_{J,meas}$ at the frequencies where the spectral response of the qubit peaks. We find that the measured rates at 190 GHz

(270 GHz) are a factor 10 (20) smaller than those expected from our naive calculation. This discrepancy could be due to additional photon losses in the materials of the enclosure, including Rogers PC board launchers. However, we believe the dominant source of photon loss is local trapping of photons emitted into the substrate of the transmitter junction, due to the near-continuous coverage of the transmitter chip by a superconducting Nb groundplane. Eventually, after many reflections (due to the large mismatch between the surface impedance of the aluminum of the sample enclosure and free-space impedance), these photons will be absorbed in the sample enclosure and exit the system.

6.6 Extended Xmon Dataset

We measured the rate of parity switches induced by Josephson radiation from a single transmitter junction for three different Xmon devices on the same receiver chip. The receiver chip geometry is shown in the inset of Fig. 6.4a. The receiver and transmitter chips are mounted face to face with a separation of 9.6 mm; in this inset, the position of the transmitter junction (as seen looking through the chips) is indicated by a yellow star. The three Xmons share similar island geometry and junction parameters (see Table 9.1 for details; one of the qubits has a slightly smaller island corresponding to a slightly higher fundamental antenna resonance frequency). In Fig. 6.4a, we plot the parity switching rates measured for these three devices as a function of Josephson frequency of the transmitter. We observe similar resonant structure in all devices, despite different separation and relative orientation with respect to the transmitter. This observation lends support to the assumption that multiple reflections in the shared aluminum enclosure will randomize the direction and polarization of the Josephson radiation.

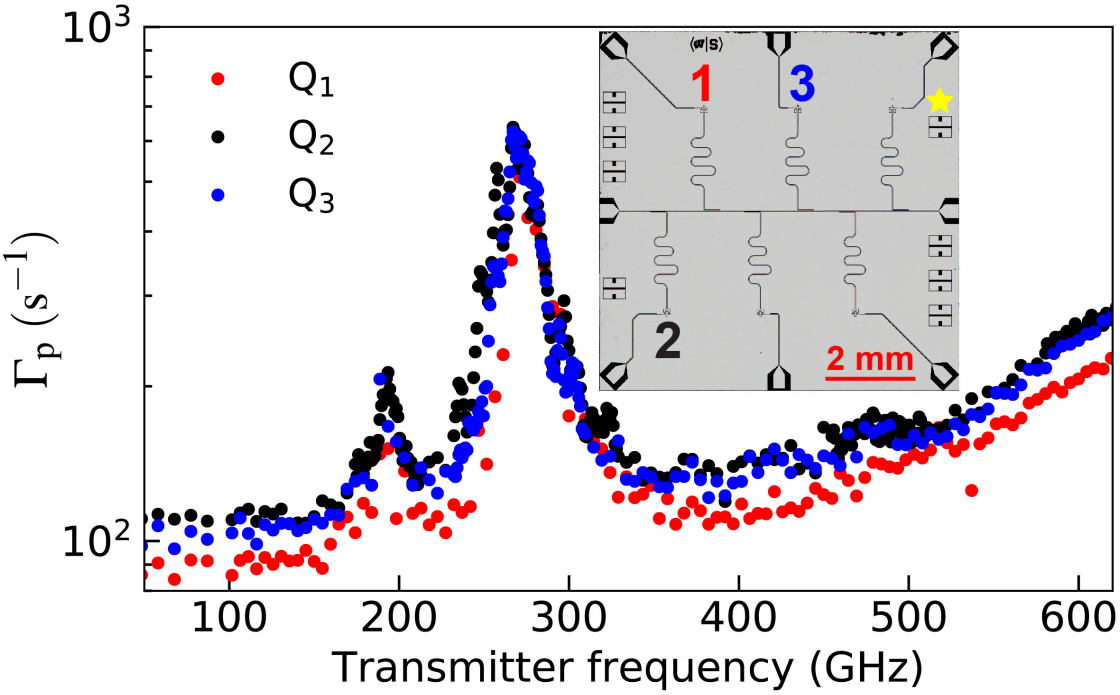

Figure 6.4: **Spectral response of three Xmon qubits.** Three qubits of similar design at different positions are measured in the same cooldown. They share the same transmitter (Fig. 5.2a). Extracted parity switching rates show similar response to the transmitter. Inset shows the positions of the three qubits on the receicer chip. The yellow star shows the relative location of the transmitting antenna on the other chip. The two chips are positioned face to face with 9.6 mm chip to chip spacing shown as in Fig. 5.1c.

In a separate experiment, we measure the equilibrium $|1\rangle$ state occupation of Xmon Q_2 as a function of transmitter frequency. Here we use a more strongly coupled transmitter with the same geometry as that shown in Fig. 5.2a, but with different junction parameters corresponding to a factor 7.9 higher critical current and a factor 1.6 greater coupling efficiency at 270 GHz. In Fig. 6.5, we plot P_1 versus transmitter frequency. While this measurement is far less sensitive than the Ramsey-based parity experiment, we see that the excess $|1\rangle$ state occupation displays similar resonant structure due to qubit transitions induced by absorption of pair-breaking photons.

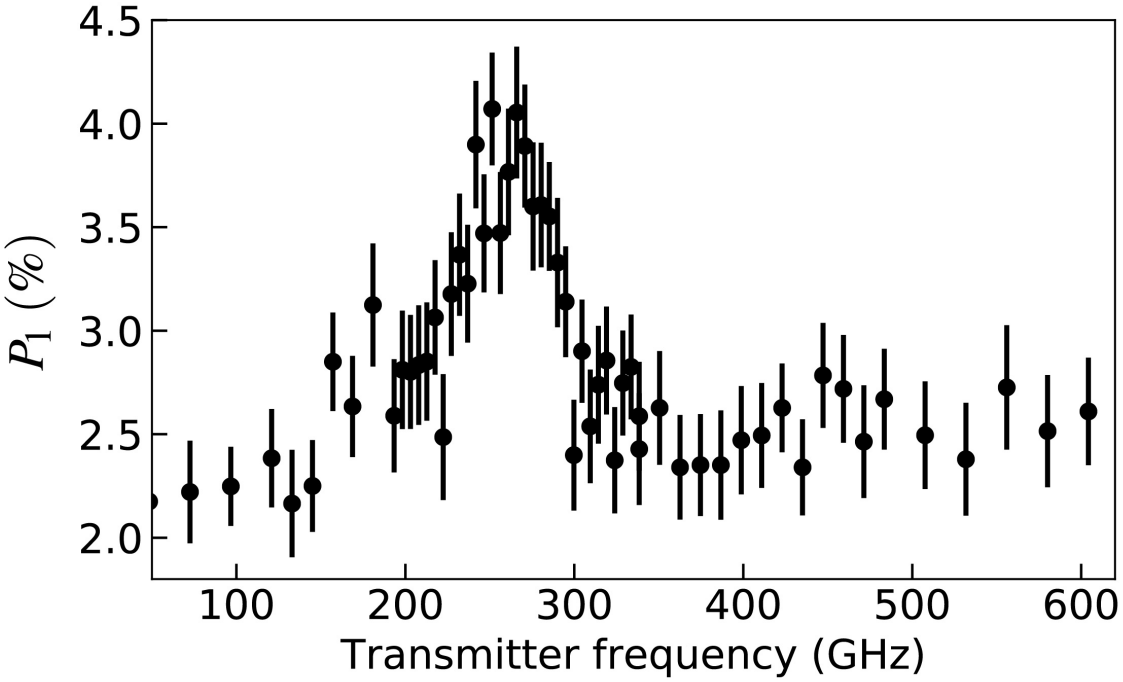

Figure 6.5: **Dependence of $|1\rangle$ occupation on transmitter frequency.** Occupation of the qubit $|1\rangle$ state is enhanced due to resonant absorption of pair-breaking photons. The peak at 270 GHz coincides with the peak in photon transfer efficiency from the transmitter junction to the Xmon qubit. Error bars represent the standard error of the mean at each point.

6.7 Correlation Between Qubit Transitions and Parity Switches

The absorption of a pair-breaking photon at the qubit junction can induce qubit state transitions; a detailed analysis of this physics has been performed by Houzet *et al.* [34]. We have separately characterized the rate of parity switches $\Gamma_{\mathrm{p,\ PAT}}$ and upward qubit transitions $\Gamma_{\uparrow,\ \mathrm{PAT}}$ induced by coherent mm-wave irradiation from the transmitter; see Fig. 5.4 in the main text. The coupling efficiency of the transmitter junction used in these experiments is shown in Fig. 6.6. From [34], the rate of transitions out of the qubit $|0\rangle$ state and the rate of parity switches induced by

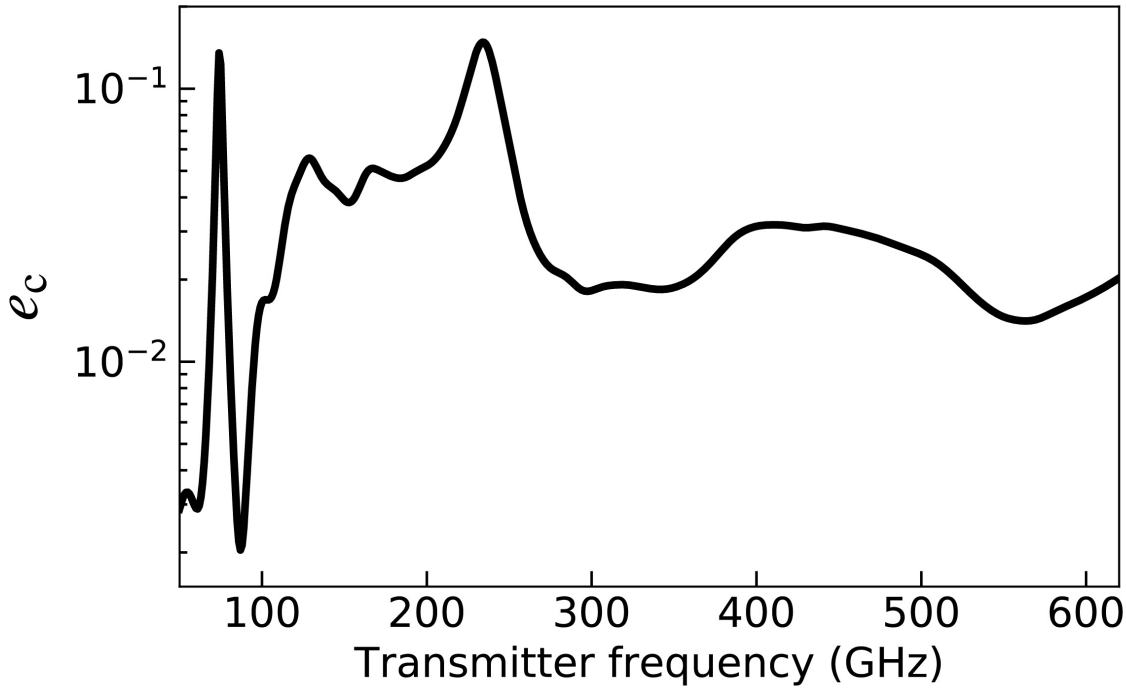

Figure 6.6: **Coupling efficiency of transmitter used in the experiments of Fig. 5.4.**

photon absorption are related as follows:

$$\Gamma_{\uparrow,\ \mathrm{PAT}} = \left(1 + \sqrt{\frac{8E_\mathrm{J}}{E_\mathrm{c}}}\frac{S_-}{S_+}\right)^{-1} \Gamma_{\mathrm{p},\ \mathrm{PAT}}, \tag{6.15}$$

where the structure factors are defined as

$$S_\pm(\hbar\omega/\Delta) = \int_1^{\hbar\omega/\Delta - 1} dx \frac{x(\hbar\omega/\Delta - x) \pm 1}{\sqrt{x^2-1}\sqrt{(\hbar\omega/\Delta - x)^2 - 1}}; \tag{6.16}$$

see Fig. 6.7a.

In Fig. 6.7b, we plot the ratio $\Gamma_{\uparrow,\ \mathrm{PAT}}/\Gamma_{\mathrm{p},\ \mathrm{PAT}}$ obtained from Eq. 6.15 versus energy of the pair-breaking photon. Here we take $E_\mathrm{J}/E_\mathrm{c} = 28$, as relevant for circmon device Q_2 studied in Fig. 5.4 of the main text. For high photon energy, we see that this ratio saturates to 6%. However, the measured ratio of upward

transitions to parity switches is 20%. The enhanced rate of spurious transitions out of the $|0\rangle$ state can be explained in terms of additional qubit transitions induced by diffusion of quasiparticles across the qubit junction following the primary poisoning event.

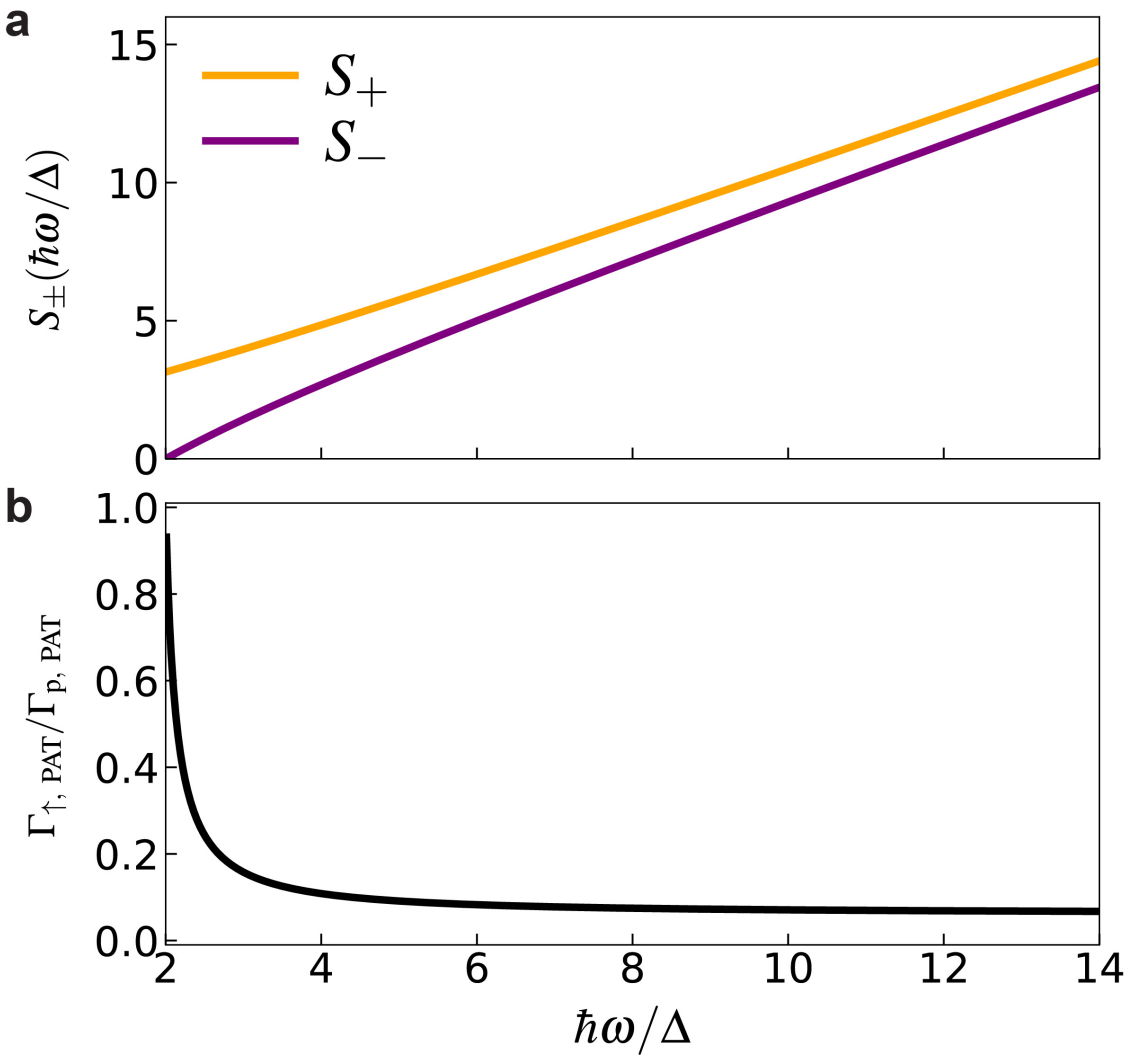

Figure 6.7: **a**, Structure factors for photon-assisted quasiparticle poisoning events. **b**, Ratio $\Gamma_{\uparrow,\,\mathrm{PAT}}/\Gamma_{\mathrm{p},\,\mathrm{PAT}}$ of spurious qubit upward transitions to quasiparticle poisoning events induced by photon absorption as a function of photon energy. Here, we take $E_\mathrm{J}/E_\mathrm{c} = 28$.

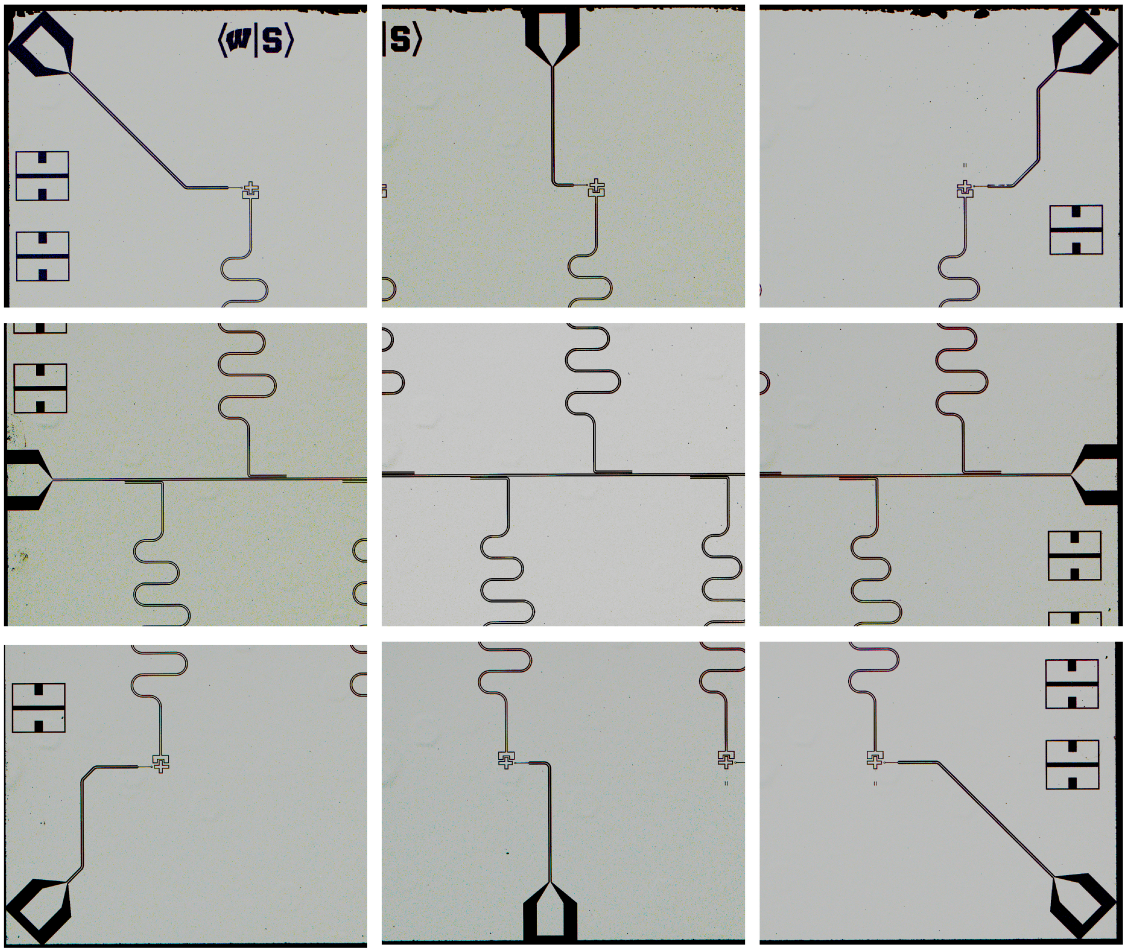

Figure 6.8: **Raw device images prior to stitching.**

6.8 Device Image Stitching

The full chip image shown in Extended Data Fig. 6.1 and 6.4 is made of nine separate microscope images stitched together (see Extended Data Fig. 6.8). Adobe Photoshop's Auto-Blend Layers command is used to combine the aligned images into one image. This tool adjusts the contrast and brightness to compensate the non-uniform exposure of each individual image to make the full chip image look smooth.

Chapter 7

Single Flux Quantum Circuit Characterization

In this section, we discuss how to characterize an SFQ driver and how to use the SFQ driver to control the qubit rotation.

7.1 SFQ Driver Characterization

When the SFQ driver is cooled down in a cryostat, the first critical step is to test if the driver is still alive. Due to the fact that SFQ pulses are of width of pico seconds, it is not trivial to monitor the real-time response in the time domain. Instead, the conventional method is measure the current-voltage (IV) characteristic measurement of the SFQ driver. The essential physics underlying the IV curve measurement is *Shapiro steps* [82]. When a Josephson junction is irradiated with radiation of angular frequency ω, the response of the supercurrent give rise to constant-voltage in the dc IV curve [13].

The setup is shown in Fig. 7.1. The circuit diagram of the SFQ driver unit is

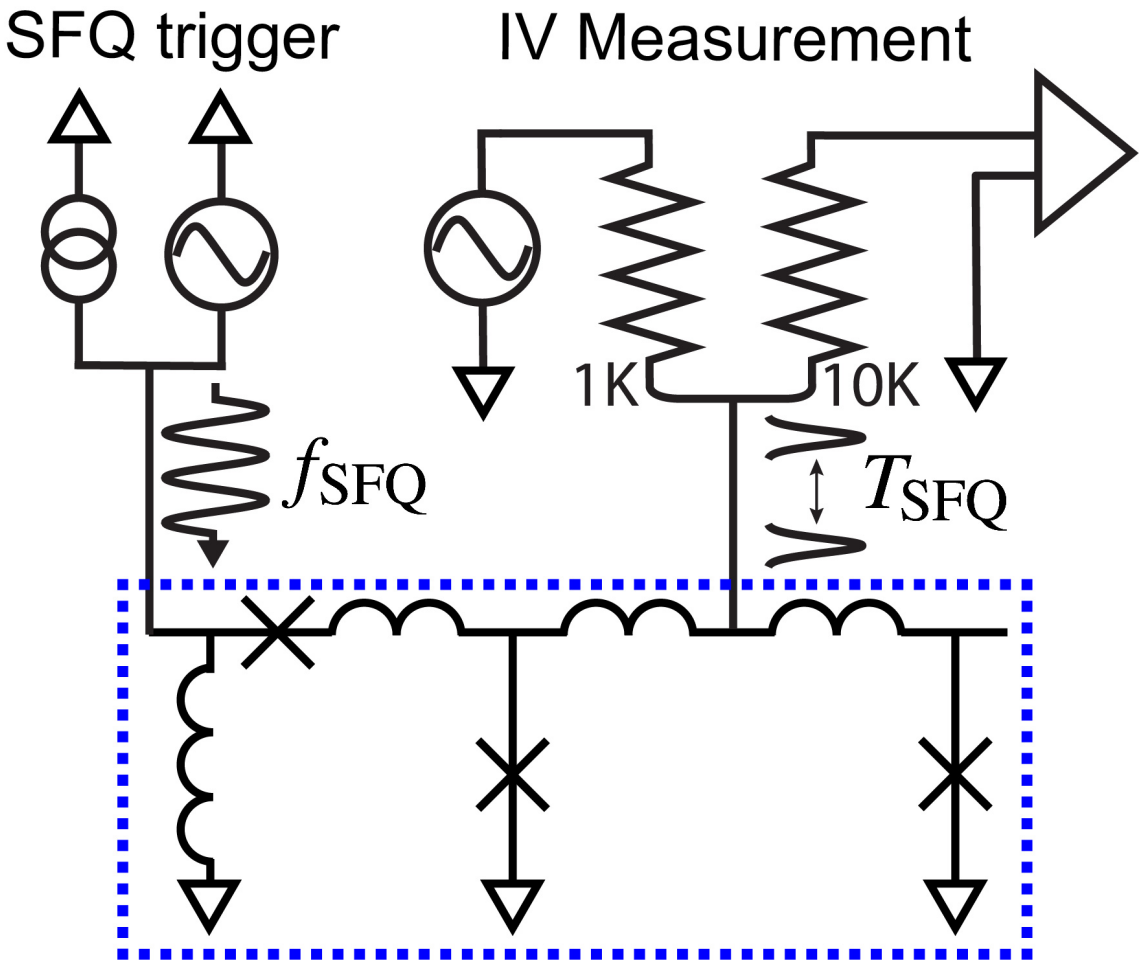

Figure 7.1: **Characterization of the SFQ driver.**

plotted in the blue dashed box. On the left port, a dc-offset rf signal with frequency f_{SFQ} is sent to the trigger port of the SFQ driver. The output port is connected to the IV measurement. If the driver is alive, trains of SFQ pulses will be generated with spacing $T_{\mathrm{SFQ}} = 1/f_{\mathrm{SFQ}}$ in time domain. An average voltage proportional to the trigger frequency can be measured

$$\Delta V = \frac{1}{T_{\mathrm{SFQ}}} \int V(t)dt \tag{7.1}$$

$$= f_{\mathrm{SFQ}}\Phi_0. \tag{7.2}$$

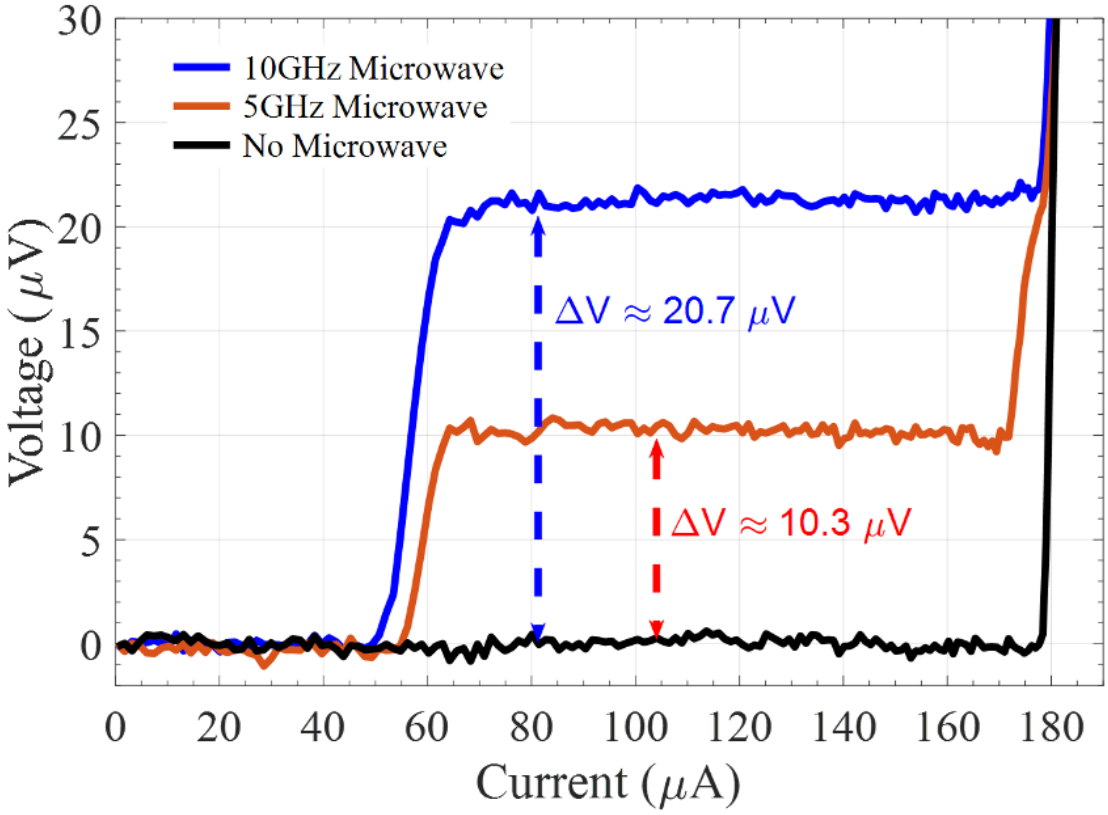

Figure 7.2: **IV curve measurement of the SFQ driver.**

A typical IV curve is shown in Fig. 7.2. As we can see, if there is no trigger applied (black curve), we just reveal a normal IV curve showing the critical current of the driver is around 180 μA. If a 5 GHz trigger is applied (red curve), we arrive at a Shapiro step $\sim$ 10.3 μV. When the trigger frequency is doubled (blue curve), the Shapiro step voltage will also be doubled.

7.2 Coupling Between the SFQ Driver and the Transmon Qubit

Following [83], we show how to control the transmon qubit with SFQ pulses. Let's start from a simple classical model of an LC resonator. As shown in Fig. 7.3a, the

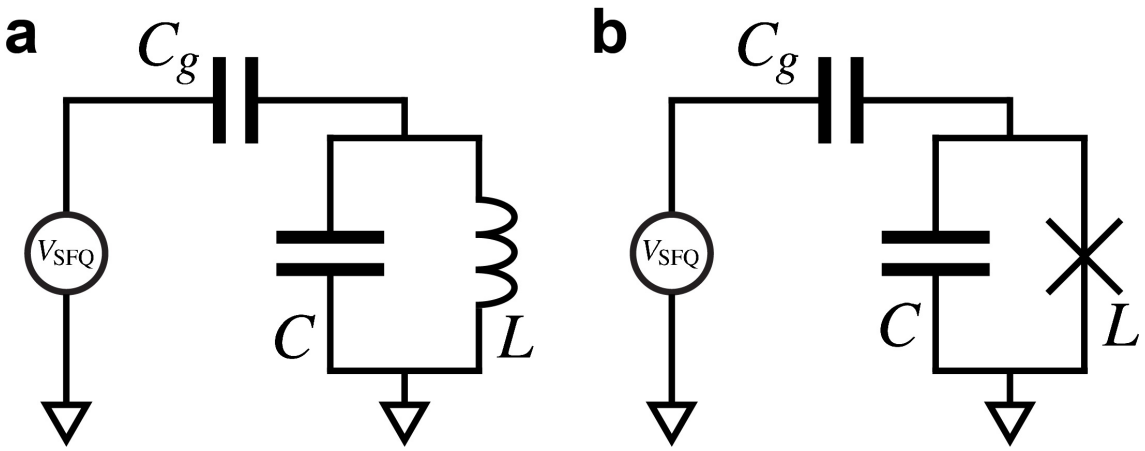

Figure 7.3: **Coherent drive of resonator and qubit from capacitively coupled SFQ voltage source.**

SFQ voltage drive source is capacitively coupled to the LC resonator via a coupling capacitance C_g. For the LC resonator, the inductance and capacitance are given by $L = L_r$ and $C = C_r$. The energy deposited into the resonator is given by

$$E = \frac{\omega_0^2 C_g^2}{2C_\Sigma} |\widetilde{V}_{\mathrm{SFQ}}(\omega_0)|^2, \tag{7.3}$$

where $C_\Sigma = C_g + C$, $\omega_0 = 1/\sqrt{LC_\Sigma}$, and where the tilde represents the Fourier transform

$$\widetilde{V}_{\mathrm{SFQ}}(\omega) = \int_{-\infty}^{\infty} V_{\mathrm{SFQ}}(t) e^{-i\omega t} dt. \tag{7.4}$$

The energy deposited into the resonator is proportional to the energy spectral density of the SFQ drive at the resonator frequency ω_0.

For the SFQ pulse, the state-of-the-art niobium-based technology, characteristic pulse amplitudes are of order of $\sim$mV and pulse widths of order $\sim$ps. Since the pulse widths are two order of magnitudes faster than the periods of microwave resonator, we can model the SFQ pulse as a Dirac delta function

$$V_{\mathrm{SFQ}} = \Phi_0 \delta(t). \tag{7.5}$$

In this case, the Fourier transform of the SFQ pulse can be simplified as

$$\widetilde{V}_{\mathrm{SFQ}}(\omega) = \Phi_0, \tag{7.6}$$

and Eq. 7.3 reduces to

$$E_1 = \frac{\omega_0^2 C_\Sigma^2 \Phi_0^2}{2C_\Sigma}, \tag{7.7}$$

where the subscript 1 indicates that we are referring to the response to a single SFQ pulse.

Since the widths of SFQ pulses are of ∼ps, a single SFQ pulse produces broadband excitation of bandwidth ∼THz. For this particular reason, one single SFQ pulse cannot be used to introduce coherent manipulation of quantum circuits, since it cannot simply address one transition among nearby transitions. However, if we drive the resonator with a train of SFQ pluses, the bandwidth can be ultra-narrow. Here, we consider applying resonant drive, where the spacing of SFQ pulses T is matched to the period of the resonator. In this case, the energy of n SFQ pulses is

$$E_n = \frac{\omega_0^2 C_\Sigma^2 \Phi_0^2}{2C_\Sigma} \frac{\sin^2(n\omega_0 T/2)}{\sin^2(\omega_0 T/2)}. \tag{7.8}$$

For typical parameters of circuit QED system, the resonator can be populated with a single excitation in time of ∼10 ps.

Now, with the classical drive of LC resonator, let us discuss the response of a quantum LC resonator to SFQ excitation. The time-dependent Hamlitonian is written as

$$H = \frac{|\hat{Q} - C_g V_{\mathrm{SFQ}}(t)|^2}{2C_\Sigma} + \frac{\hat{\Phi}}{2L}. \tag{7.9}$$

This Hamiltonian can be decomposed into two pieces, the unperturbed free Hamil-

tonian H_{free} and a time-dependent Hamiltonian H_{SFQ} from the SFQ excitation:

$$H_{\text{free}} = \frac{\hat{Q}^2}{2C_\Sigma} + \frac{\hat{\Phi}}{2L}, \tag{7.10}$$

$$H_{\text{SFQ}} = -\frac{C_g}{C_\Sigma} V_{\text{SFQ}}(t)\hat{Q}. \tag{7.11}$$

In terms of the conventional annihilation and creation operators, we have

$$H_{\text{free}} = \hbar\omega_0 \hat{a}^\dagger \hat{a} \tag{7.12}$$

$$H_{\text{SFQ}} = iC_g V_{\text{SFQ}}(t)\sqrt{\frac{\hbar\omega_0}{2C_\Sigma}}(\hat{a} - \hat{a}^\dagger). \tag{7.13}$$

We now consider application of resonant SFQ pulses to a truncated Transmon qubit (shown in Fig.7.3b). The Transmon can be seen as a two-level system. The Hamiltonian becomes

$$H_{\text{free}} = \frac{\hbar\omega_0}{2}(1 - \hat{\sigma}_z) \tag{7.14}$$

$$H_{\text{SFQ}} = C_g V_{\text{SFQ}}(t)\sqrt{\frac{\hbar\omega_0}{2C_\Sigma}}\hat{\sigma}_y. \tag{7.15}$$

From Eq. 7.15, the excitation of one SFQ pulse can be understood as a discrete rotation of the state vector in the Bloch sphere about the y axis by angle

$$\delta\theta = C_g \Phi_0 \sqrt{\frac{2\omega_{\text{qb}}}{\hbar C_\Sigma}}; \tag{7.16}$$

in between SFQ pulses, the qubit accumulates phase rotation at the speed of qubit period under the influence of H_{free}.

Chapter 8

Single Flux Quantum-Based Digital Control of Superconducting Qubits in a Multi-Chip Module

The single flux quantum (SFQ) digital superconducting logic family has been proposed for the scalable control of next-generation superconducting qubit arrays. In the initial implementation, SFQ-based gate fidelity was limited by quasiparticle (QP) poisoning induced by the dissipative on-chip SFQ driver circuit. In this work, we introduce a multi-chip module architecture to suppress phonon-mediated QP poisoning. Here, the SFQ elements and qubits are fabricated on separate chips that are joined with In bump bonds. We use interleaved randomized benchmarking to characterize the fidelity of SFQ-based gates, and we demonstrate an error per Clifford gate of 1.2(1)%, an order-of-magnitude reduction over the gate error achieved in the initial realization of SFQ-based qubit control. We use purity benchmarking to

quantify the contribution of incoherent error at 0.96(2)%; we attribute this error to photon-mediated QP poisoning mediated by the resonant mm-wave antenna modes of the qubit and SFQ-qubit coupler. We anticipate that a straightforward redesign of the SFQ driver circuit to limit the bandwidth of the SFQ pulses will eliminate this source of infidelity, allowing SFQ-based gates with fidelity approaching theoretical limits, namely 99.9% for resonant sequences and 99.99% for more complex pulse sequences involving variable pulse-to-pulse separation. Part of this chapter and Chapter 9 have been submitted for publication in journal PRX Quantum.

8.1 Introduction

Superconducting qubits have achieved both gate [84] and measurement [85, 86] fidelity at the threshold for fault-tolerant operation. [87]. Recent demonstrations of quantum supremacy [1] and of distance-three and distance-five surface codes [88, 89, 90] motivate efforts to scale to larger multiqubit arrays that are compatible with robust error correction. However, theoretical estimates suggest that a practical error-corrected quantum computer will require more than one million physical qubits, for physical hardware at the current level of fidelity [87]. While it is believed that current quantum–classical interface technology can be scaled by brute force to implement systems with around 1000 physical qubits, limited by the heat load and physical footprint of the control hardware [91], no clear path is known for further scaling up. There have been serious steps to address specific obstacles to scaling, including establishment of quantum links between separated cryogenic systems [92], optimization of room temperature hardware design for a more compact microwave unit [93], integration of cryogenic CMOS-based microwave pulse generators into qubit cryostats for proximal control [94, 95], utilization of low heat-load photonic

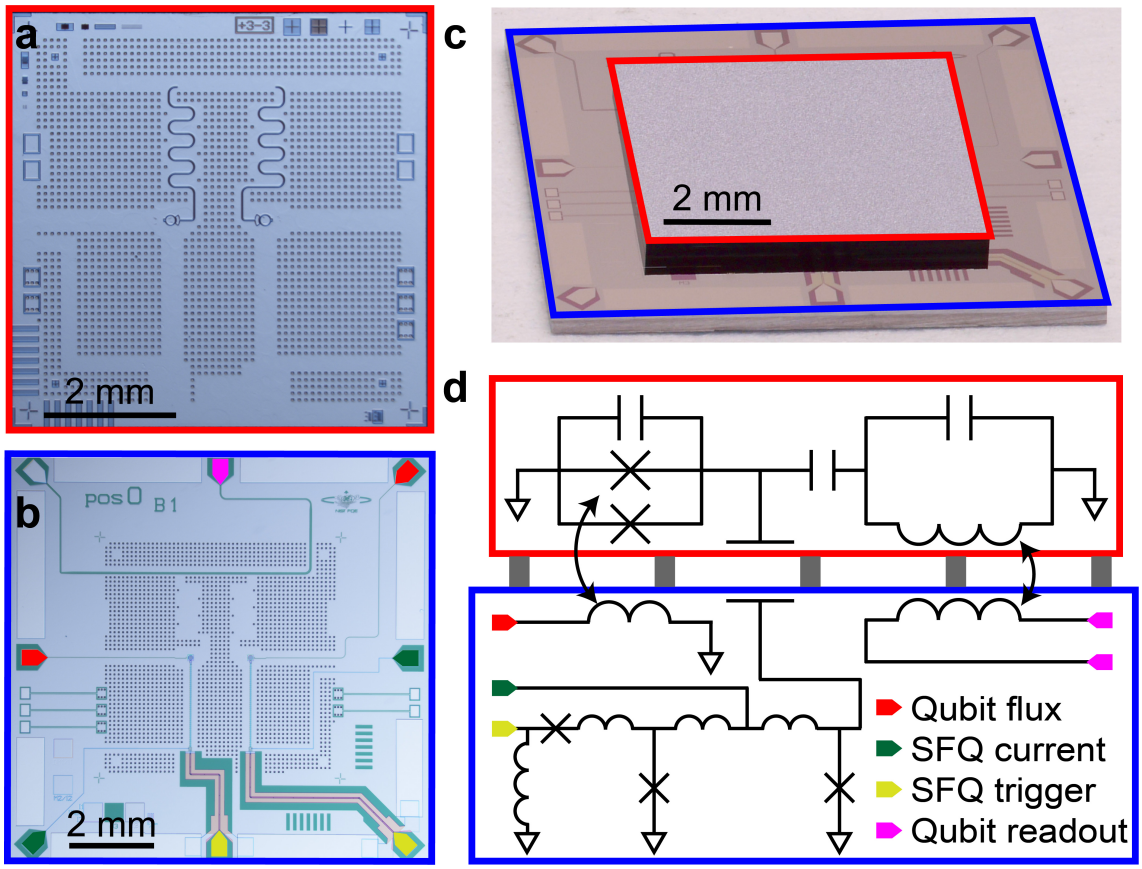

Figure 8.1: Quantum–classical multichip module (MCM). **a**, Micrograph of the qubit chip. Two flux-tunable transmons are fabricated on the chip, each with a local quarter-wave coplanar resonator for readout. **b**, Micrograph of the SFQ driver chip. Two dc/SFQ converters are integrated on the chip, along with the feedline for the readout resonators and flux-bias lines for the qubits. The indium bumps are visible as the regular grid pattern over the continuous ground plane. **c**, Photograph showing the assembled MCM stack; the qubit chip is outlined in red and the SFQ chip is outlined in blue. **d**, Circuit diagram for one qubit–SFQ pair; here, the quarter-wave readout mode is depicted using its lumped-element equivalent. Indium bump bonds between the groundplanes provide the only galvanic connection between the two chips; coupling between circuit elements across the chip-to-chip gap is achieved either capacitively or inductively. The colors used in the legend to identify specific circuit elements are matched to the false coloring of the bond pads in the image of **b**,.

links to route control and measurement signals within the cryostat [96], and development of compact, low heat-load microcoax cables [97]. However, an integrated systems engineering approach to scaling superconducting qubits is so far lacking.

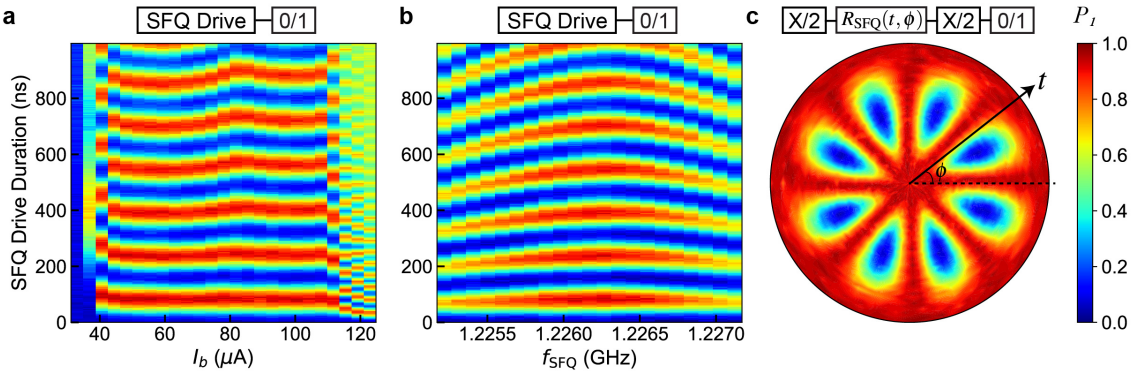

Figure 8.2: SFQ-based qubit operation at subharmonic drive frequency $f_{01}/4$. **a**, Rabi oscillations as a function of current bias I_b of the SFQ driver. **a**, Rabi chevron experiment at variable drive frequency in the vicinity of $f_{01}/4$. **a**, Generalized Rabi scan at $f_{01}/4$, with variable time t and phase ϕ for the Rabi drive.

Typically, qubit control is achieved with shaped microwave pulses derived from room-temperature digital-to-analog converters and microwave generators; the hardware overhead associated with microwave-based qubit control is one of the major obstacles to scaling to large system sizes. An alternative approach is based on the single flux quantum (SFQ) digital logic family [98, 99, 12]. Here, the qubit mode is irradiated with a train of quantized flux pulses, with pulse-to-pulse timing adjusted to induce a coherent rotation in the computational subspace and to minimize leakage [83]. This approach, in conjunction with digital qubit readout using the Josephson photomultiplier [100, 101, 86], forms the basis of a scalable quantum–classical interface for ultralarge qubit arrays [102]. An initial experiment to implement SFQ-based control of superconducting qubits yielded fidelity of 95% for $\pi/2$ and π rotations [46]; gate fidelity was limited by quasiparticle (QP) poisoning [22] associated with operation of the dissipative SFQ pulse generator, which was fabricated on the same chip as the qubit. In a more recent experiment, digital control of a 3D transmon qubit with an error per Clifford gate of 2.1(1)% was demonstrated using a Josephson pulse generator [103] located at the 3 K stage of the cryostat [104]. There have been sep-

arate theoretical proposals for high-fidelity SFQ-based control sequences involving variable pulse-to-pulse separation [105, 106], for SFQ-based entangling gates [107], and for a scalable multiqubit architecture based on SFQ control [108]. However, a key prerequisite to adoption of SFQ control for large-scale multiqubit arrays is realization of high-fidelity single-qubit rotations. It is critical to investigate all the potential error channels and to understand the fundamental limits to fidelity, chief among them generation of QPs by the dissipative SFQ pulse driver.

In this work, we adopt a multi-chip module (MCM) architecture to segregate the SFQ pulse driver and the qubit onto two separate chips. In so doing, we suppress both phonon-mediated QP poisoning and direct diffusion of QPs from the SFQ driver to the qubit. We demonstrate an order-of-magnitude reduction in SFQ-based gate infidelity compared to [46], with an average error per Clifford gate of 1.2(1)%. We find that infidelity is dominated by incoherent error associated with *photon*-mediated QP poisoning. We anticipate that straightforward design changes to the SFQ driver and appropriate QP mitigation on the qubit chip can lead to further reductions in gate infidelity, to the point where we are limited by leakage to errors of order 0.1% with naive resonant control and 0.01% for optimized control sequences [105, 106].

This manuscript is organized as follows. In Section 8.2, we present the quantum–classical MCM and describe basic SFQ-based single-qubit control. In Section 8.3, we describe randomized benchmarking (RB) and interleaved randomized benchmarking (IRB) to characterize the fidelity of $\pi/2$, π, and average Clifford rotations, and we perform detailed error budgeting of SFQ-based gates. In Section 8.4, we show that infidelity is dominated by a subtle form of QP poisoning associated with emission of pair-breaking photons from the SFQ driver. In Section 8.5, we present simulation results that validate our model for photon-assisted QP poisoning mediated via spu-

rious antenna modes of the qubit and SFQ-qubit coupler. Finally, in Section 8.6, we discuss straightforward modifications to the SFQ-qubit architecture to further suppress QP-induced gate infidelity. These improvements should allow us to access gate fidelity comparable to that achieved with state-of-the-art microwave-based gates, but with a compact, streamlined hardware footprint for the control system.

8.2 Quantum–Classical MCM and SFQ-Based Qubit Control

To suppress QP poisoning, the dominant source of infidelity in previous approaches to SFQ-based qubit control [46], we segregate the qubit and SFQ elements onto two separate chips that are bump-bonded with In to form the MCM stack shown in Fig. 8.1. The qubit chip shown in Fig. 8.1a incorporates two flux-tunable transmon qubits, each with its own local quarter-wave resonators for state measurement. The SFQ driver chip shown in Fig. 8.1b incorporates two dc-to-SFQ converters along with all control and readout lines for the qubits. The two chips are bonded by In bumps to form the MCM via the technique described in Sec. 9.1.3; see Fig. 8.1c. The MCM architecture suppresses QP poisoning of the qubit in two ways. First, the direct diffusion of QPs from the SFQ driver to the qubit is not possible, as the two elements reside on separate chips that are separated by low-gap In bump bonds: QPs that relax to the In gap edge will be unable to enter the Nb groundplane of the quantum chip [109]. Similarly, pair-breaking phonons that propagate to the In bump bonds are expected to scatter to the In gap edge through electron-phonon interaction, so that phonons will have insufficient energy to enter the Nb groundplane of the qubit chip; acoustic mismatch across the bump bonds will further inhibit phonon propagation from chip to chip. In Fig. 8.1d, we show a simplified circuit

diagram for one qubit–SFQ pair, with the qubit readout resonator depicted as its lumped element equivalent tank circuit. Each qubit–SFQ pair involves one flux bias line for the qubit, one current bias line for the SFQ driver, and one microwave drive line to trigger SFQ pulses. The qubit readout line is shared between the two qubit–SFQ pairs. Details of the experimental setup are given in Sec. 9.2.

The quantum–classical MCM is characterized in a closed-cycle dilution refrigerator at a base temperature of 20 mK. Preliminary optimization of SFQ-based qubit rotations is described in Fig. 8.2. To avoid direct drive of the qubit via crosstalk from the SFQ trigger line, we generate an SFQ pulse train at a subharmonic of the fundamental qubit frequency f_{01}. In the experiments described here, we drive the qubit at the frequency $f_{01}/4$. With the SFQ trigger tone applied, we sweep the current bias I_b of the SFQ pulse driver to determine an operating regime where the induced qubit Rabi frequency is insensitive to SFQ driver bias; results are shown in Fig. 8.2a. Over the optimal range of SFQ driver operation, we find a weak dependence of Rabi frequency on I_b; we discuss possible explanations for this dependence in Sec. 9.3. In Fig. 8.2b, we show the results of a Rabi chevron experiment used to fine tune the SFQ drive frequency. Finally, we perform the generalized Rabi experiment described in Fig. 8.2c in order to identify the duration and relative timing of SFQ pulse trains needed to execute qubit rotations about arbitrary control vectors oriented in the equatorial plane of the Bloch sphere.

8.3 Benchmarking of SFQ Gates

After demonstrating basic qubit control with SFQ pulse trains, we characterize the fidelity of SFQ-based gates. It is critical to find the set of parameters in the multi-dimensional SFQ operation space to optimize gate fidelity. In this work, the SFQ

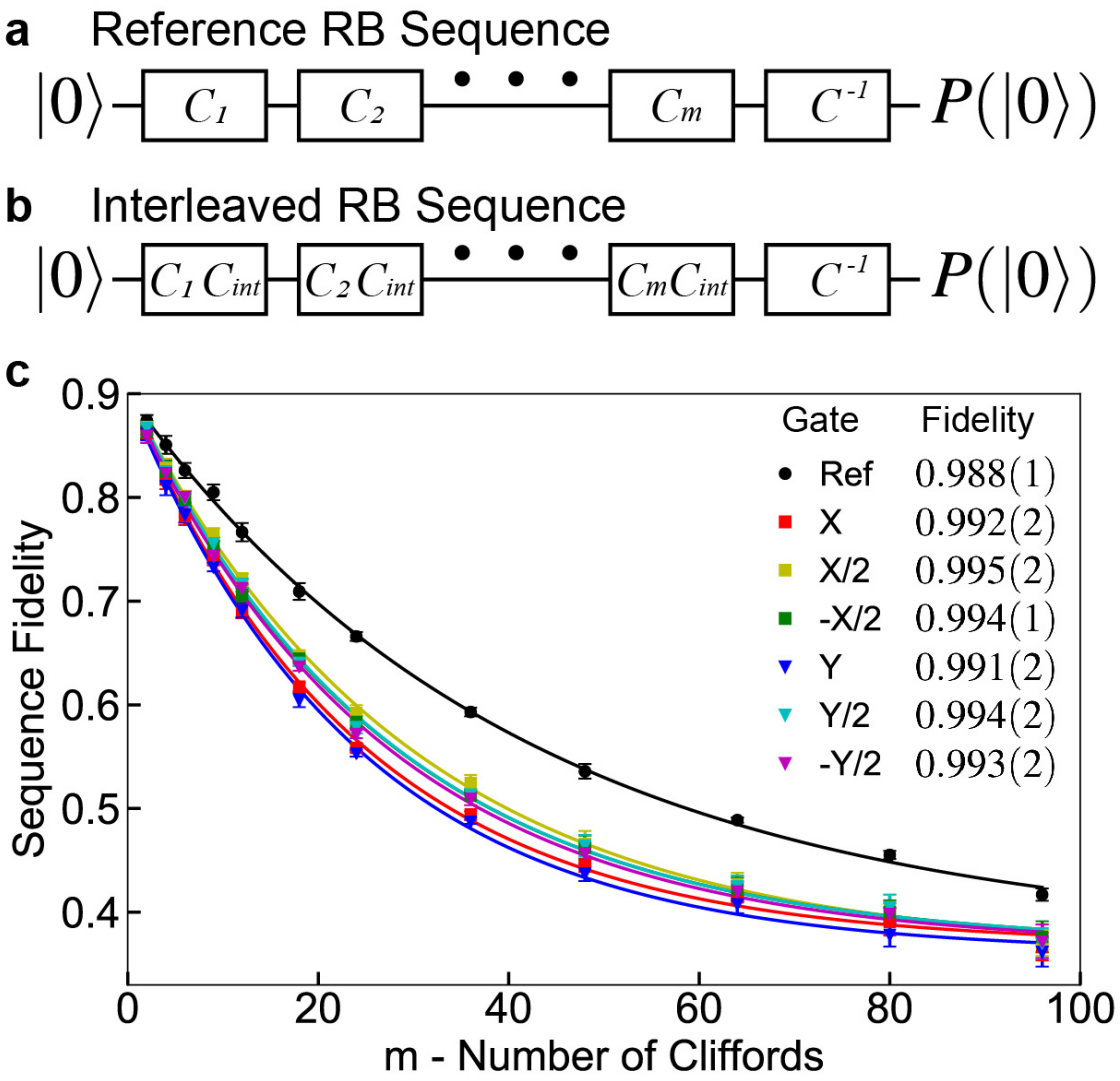

Figure 8.3: Randomized Benchmarking (RB) of SFQ-based gates with drive at frequency $f_{01}/4 = 1.2264$ GHz. Pulse sequences for **a** reference and **b** interleaved RB. **c**, Depolarizing curves for the reference RB sequence and six interleaved RB sequences. Each data point is the average of 150 random sequences across 6 hours. Inset shows the fidelities of the average Clifford gate [110] and the six interleaved gates.

control parameters include the bias current I_b, the trigger frequency f_{SFQ}, the phase difference between orthogonal rotations, the trigger amplitude, and related mixer calibration parameters of the trigger signal. Here, we follow a two-step optimization procedure involving error amplification to tune up individual gates followed by global

optimization using randomized benchmarking (RB) [111, 112]. Initially, we find the best operating parameters for each individual gate. We construct equivalent identity and π-pulse sequences by concatenating many instances of the individual gate, e.g., $S_1 = \mathrm{X}^{30}$, and $S_2 = \mathrm{X}^{31}$. We measure the difference of $|1\rangle$-state occupation following application of the two sequences $P_1(S_2) - P_1(S_1)$ while sweeping the SFQ drive parameters, and we adjust parameters to maximize the sequence contrast. We find that optimal parameters for the SFQ driver are not exactly the same across all SFQ-based gates. For global optimization of SFQ-based gates, including optimization of the time delay associated with orthogonal rotations on the Bloch sphere, we maximize the RB sequence fidelity following the ORBIT method developed in [113].

Following optimization of SFQ gate parameters, we use the technique of interleaved RB to access gate fidelity independent of state preparation and measurement error [114]. Here, we evaluate the fidelity of the set of gates $\{\mathrm{X}, \mathrm{Y}, \pm\mathrm{X}/2, \pm\mathrm{Y}/2\}$. In Fig. 8.3, we present RB data taken across 6 hours, highlighting the temporal stability of SFQ-based single-qubit control. A fit to the reference curve yields average Clifford gate fidelity of $\mathcal{F}_{\mathrm{Cliff}} = 0.988(1)$; from the reference gate sequence and the interleaved sequences, we extract the interleaved gate fidelities shown in Fig. 8.3c. As a check, we calculate the fidelity of an average Clifford gate from the extracted fidelities of the six interleaved gates. The appropriate weighted sum over the interleaved gates fidelities yields an average Clifford gate fidelity of 0.988(3), consistent with the measured RB value $\mathcal{F}_{\mathrm{Cliff}}$.

The measured error associated with SFQ-based control shows one order of magnitude reduction compared to the first-generation result of [46]. Accurate understanding of the source of the error is critical to further optimization of SFQ-based gates. As a starting point, we need to distinguish between coherent and incoherent error. The former involves pulse sequence miscalibration, while the latter is due to

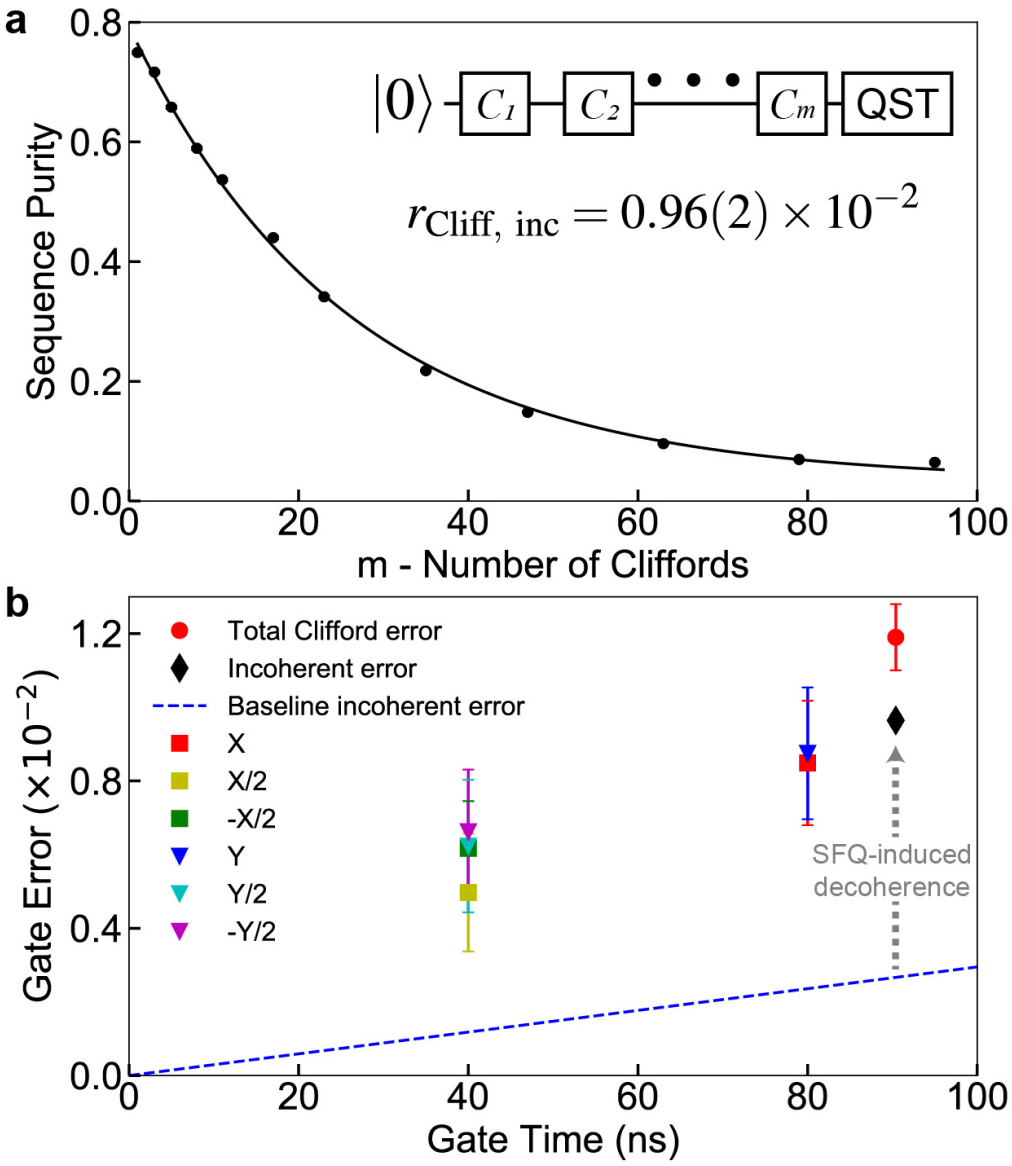

Figure 8.4: Characterization of incoherent error. **a**, Purity benchmarking of SFQ-based gates at pulse frequency $f_{01}/4 = 1.2264$ GHz. Inset shows the gate sequence for purity benchmarking. Here, quantum state tomography is applied at the end of the m randomized Cliffords. The incoherent error per Clifford $r_{\text{Cliff, inc}}$ is extracted from the purity of the final state. **b**, Gate error derived from the RB measurements of Fig. 8.3**c** versus gate duration. For the average Clifford gate (black diamond), incoherent errors constitute 80% of the total error (red circle). The blue dashed line shows the baseline incoherent error of 0.27×10^{-2} for the average Clifford gate extracted from the coherence times of the qubit measured with microwave-based gates in the absence of SFQ operation.

qubit dissipation via uncontrolled coupling to the environment.

Here, we use purity benchmarking [115] to extract the incoherent contribution to the error. The gate sequence is shown in Fig. 8.4a. We apply a random sequence of m Clifford gates followed by quantum state tomography to determine the purity of the qubit state. A fit to the purity curve yields an incoherent error for the average Clifford gate of $r_{\text{Cliff, inc}} = 0.96(2) \times 10^{-2}$. From RB, we find an error per Clifford gate of $r_{\text{Cliff}} = 1 - \mathcal{F}_{\text{Cliff}} = 1.2(1) \times 10^{-2}$. We see that 80% of the error is due to incoherent processes. In Fig. 8.4(b), we plot the error of the six interleaved gates characterized previously and of the average Clifford gate versus gate time. The average Clifford gate time is 90.4 ns, 2.26 times that of the $\pi/2$ gate. We see that gate error increases with gate duration. The dashed blue line in Fig. 8.4b shows the baseline incoherent error per gate $t_{\text{gate}}/T_{\text{error}}$ [116], where t_{gate} is the gate length and where $1/T_{\text{error}} = \frac{1}{3}(1/T_{2,\text{white}} + 1/T_1)$ is calculated from the qubit coherence times see Table 9.1 for details measured using conventional microwave-based sequences with the SFQ driver turned off [15]. Comparing this baseline error to the measured incoherent error for the average Clifford gate, we see that operation of the SFQ pulse driver induces additional incoherent error around 2.6 times that of the baseline. In the next section, we show that photon-assisted QP poisoning is the source of the additional incoherent error.

8.4 Dynamics of QP Poisoning

Nonequilibrium QPs are a dominant decoherence source for superconducting quantum devices [117, 43, 44, 26, 41], and suppression of QP poisoning associated with the dissipative SFQ pulse driver is the primary reason for adopting the MCM architecture described here. The analysis above indicates that SFQ gate infidelity is

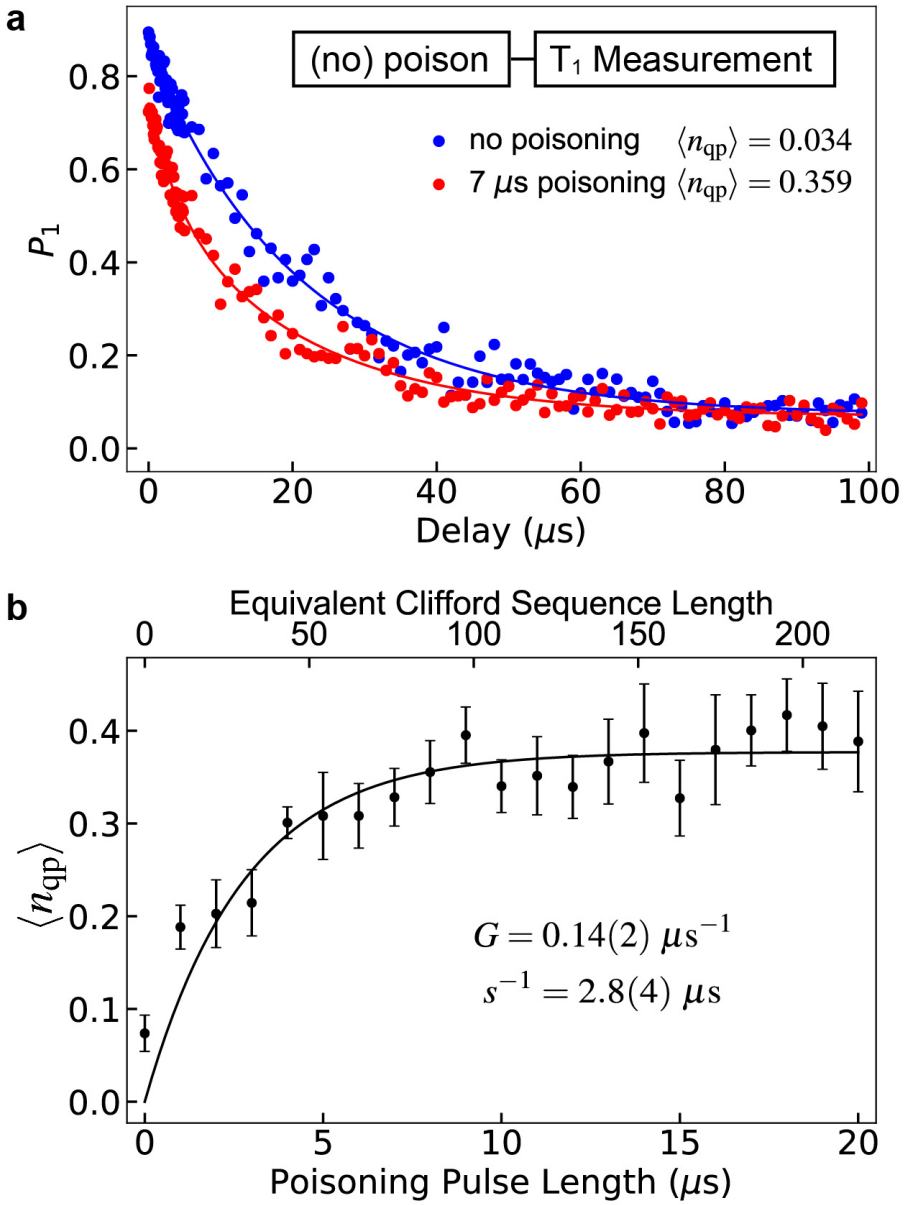

Figure 8.5: QP poisoning induced by operation of the SFQ pulse driver. **a**, Microwave-based energy relaxation curves of the qubit with and without prior application of an off-resonant SFQ pulse train at $f_{\mathrm{SFQ}} = 1.21$ GHz. The mean number $\langle n_{\mathrm{QP}} \rangle$ of QPs coupled to the qubit is extracted from a fit of Eq. 8.1 to the data. **b**, $\langle n_{\mathrm{QP}} \rangle$ vs. SFQ poisoning pulse length. Each point was extracted from eight T_1 traces of the type shown in **a**.

dominated by incoherent error and that operation of the SFQ pulse driver leads to significant suppression of qubit coherence. QP poisoning remains the most likely

mechanism for suppression of qubit coherence. To quantify the generation of QPs at the qubit chip from operation of the SFQ pulse driver, we perform microwave-based inversion recovery experiments following application of an off-resonant SFQ drive, and we fit the recovery signal to the form [40, 67]

$$P_1(t) = e^{\langle n_{\mathrm{QP}}\rangle(\exp(-t/T_{1,\mathrm{qp}})-1)-t/T_{1,\mathrm{R}}}, \tag{8.1}$$

where $P_1(t)$ is the $|1\rangle$-state occupation of the qubit, $\langle n_{\mathrm{QP}}\rangle$ is the mean number of QPs coupled to the qubit, $T_{1,\mathrm{qp}}$ is the qubit energy relaxation time per QP, and $T_{1,\mathrm{R}}$ is the energy relaxation time due to remaining relaxation channels. In Fig. 8.5a, we plot inversion recovery signals measured with (red points) and without (blue points) application of a 7 μs off-resonant SFQ poisoning pulse prior to the measurement. The solid traces are fits to the data from Eq. 8.1 to extract $\langle n_{\mathrm{QP}}\rangle$. In a separate experiment, we vary the poisoning pulse length prior to the T_1 measurement. Fits to the inversion recovery scans yield $T_{1,\mathrm{qp}} = 6.8(6)$ μs and $T_{1,\mathrm{R}} = 26(1)$ μs; in Fig. 8.5b, we plot $\langle n_{\mathrm{QP}}\rangle$ as a function of poisoning length. The data is well described by a model where the rate of QP removal is linear in QP density, as expected for both diffusion of QPs from the junction and QP trapping at defect sites. We express the time-dependent QP population as follows [63, 52]:

$$\langle n_{\mathrm{QP}}(t)\rangle = \frac{G}{s}(1 - e^{-st}), \tag{8.2}$$

where G is the QP generation rate and s is the QP removal rate. We find $G = 0.14(2)$ $\mu\mathrm{s}^{-1}$ and $s^{-1} = 2.8(4)$ μs. The generation rate corresponds to $3.7(5) \times 10^{-5}$ QPs coupled to the qubit per phase slip of the SFQ driver, a factor of 43 improvement compared to the QP poisoning seen in the first-generation SFQ control experiments of [46].

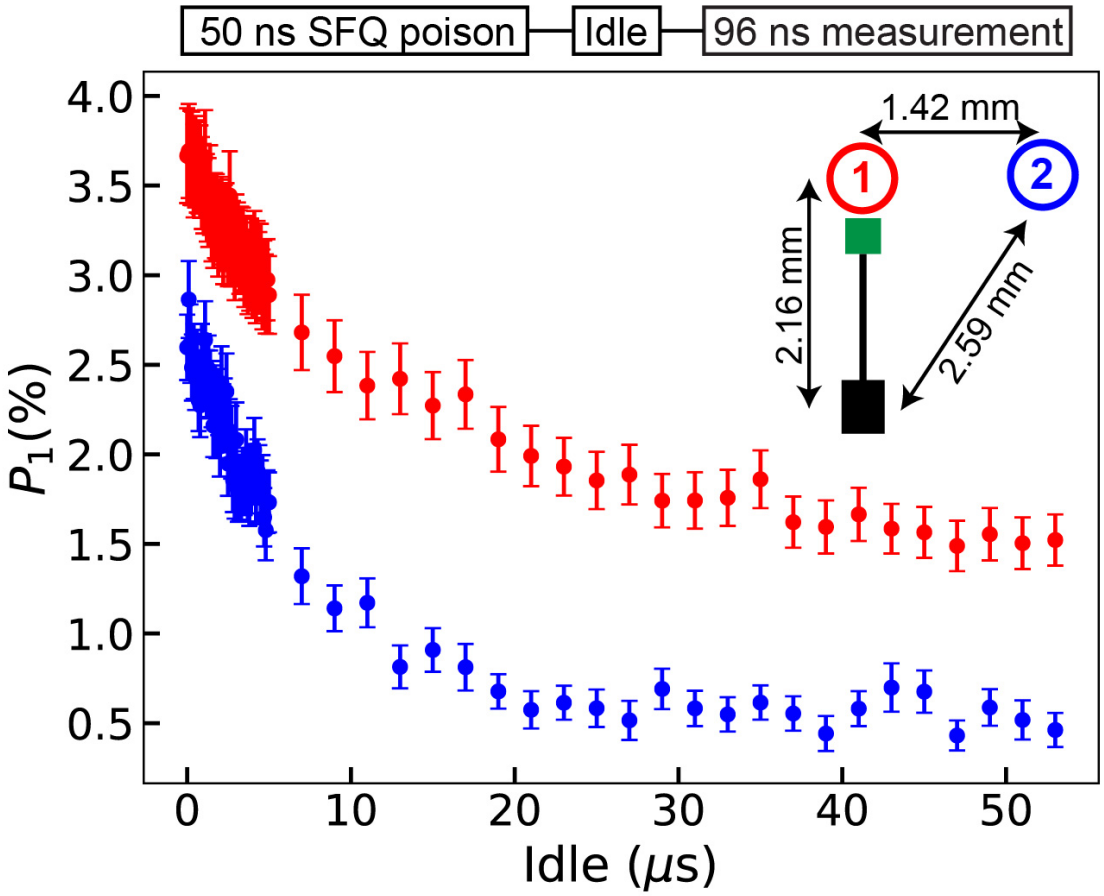

Figure 8.6: Dynamics of QP poisoning from the SFQ pulse driver. A variable idle time follows application of a brief SFQ poisoning pulse; subsequent fast qubit measurement is used to extract the qubit $|1\rangle$-state occupation P_1. Inset shows the relative positions of Q_1 (red), Q_2 (blue), the dc/SFQ converter (black rectangle) and the SFQ-qubit coupling capacitor (green square). For both qubits, P_1 decays monotonically with idle time. We observe no time lag between application of the poisoning pulse and the peaking of enhanced excess P_1, indicating that poisoning is mediated by pair-breaking photons, as opposed to pair-breaking phonons.

Our next task is to understand the physical mechanism for QP poisoning in the MCM architecture. There are two possibilities. In one scenario, QP poisoning is mediated by pair-breaking phonons that propagate from the classical chip to the quantum chip [62], despite the presence of the low-gap In bumps that are expected to promote phonon relaxation below the gap edge of the Nb groundplane of the quantum chip. Alternatively, QP poisoning could be dominated by pair-breaking

photons associated with the ultrahigh-bandwidth SFQ pulses. It is known that qubit structures are efficient absorbers of pair-breaking radiation in the mm-wave range [35, 37]; for picosecond SFQ pulses with bandwidth of order 100s of gigahertz, the electromagnetic transient could lead to emission of pair-breaking photons that are then absorbed at the qubit junction. We expect to be able to distinguish these two processes by examining the temporal dynamics of QP poisoning in our experiment: while the photon-assisted QP poisoning mechanism will lead to immediate suppression of qubit coherence, the phonon mechanism will involve a time delay of order 10s of μs between application of the SFQ pulse and the onset of enhanced QP relaxation associated with the propagation of phonons from the SFQ driver to the qubit [53].

We probe the dynamics of QP poisoning in the MCM by applying a short 50-ns burst of off-resonant SFQ pulses, using the two qubits on the MCM as QP sensors. We increment the relative delay between application of the poisoning pulse and qubit measurement; in order to access short timescales, we use a fast qubit measurement with duration of 96 ns. The geometry of the experiment is shown in the inset of Fig. 8.6. We find that the effect of QP poisoning is to increase P_1, where the baseline levels of qubits 1 and 2 are 1.6% and 0.5% respectively. This fact alone argues in favor of the photon-mediated mechanism, which drives upward qubit transitions far more efficiently than diffusion across the qubit junction of QPs that are resident in the junction leads [34]. We probe qubit population P_1 as a function of idle time following the poisoning pulse; results are shown in Fig. 8.6. We find a monotonic decrease in excess P_1 toward the baseline value following application of the poisoning pulse. In a similar experiment involving injection of pair-breaking phonons into the qubit substrate, Iaia *et al.* observed a QP-induced enhancement of qubit relaxation rate that peaks at a time $\sim$ 30 μs following application of the poisoning pulse, consistent with diffusive propagation of phonons from the injector junction to the

qubit over the ∼4-mm separation between the elements [53]. We take the much faster response of the qubit to the poisoning pulse observed in our experiments as further evidence that coupling of the SFQ driver to the qubit is mediated by photons as opposed to phonons.

8.5 Antenna Coupling of the SFQ Transient to the Qubit

It has recently been shown that absorption of pair-breaking photons is a dominant source of QP poisoning in Josephson devices [34, 36, 37, 18]. For typical geometries, the superconducting qubit structure forms a resonant antenna that provides an efficient power match from free space to the high-impedance Josephson junction at mm-wave frequencies [35]. Due to its short temporal duration of order ps, the bandwidth of a single SFQ pulse is of order 100s of gigahertz, sufficient to excite the mm-wave antenna mode of the qubit and generate QPs. In Fig. 8.7, we consider the antenna modes of the qubit and SFQ coupler structures used in our experiments. The experimental geometry is shown in Fig. 8.7 a-b; here, Nb metallization on the quantum and classical chips is shown in gray, and the white regions indicate where the Nb has been removed. The circular qubit and the SFQ-qubit capacitive coupler both act as resonant aperture antennas with efficient coupling to free space at mm-wave frequencies. Following the modeling described in [35], we plot the free-space coupling efficiency e_c of the bare qubit antenna mode as the black curve in Fig. 8.7c. The structure shows a clear resonance corresponding to a match between the qubit perimeter and one full wavelength of the radiated field. In the same figure, we plot the coupling efficiency of the qubit (red curve) and the SFQ coupler (blue curve) calculated for the full MCM structure. Both modes display a complicated

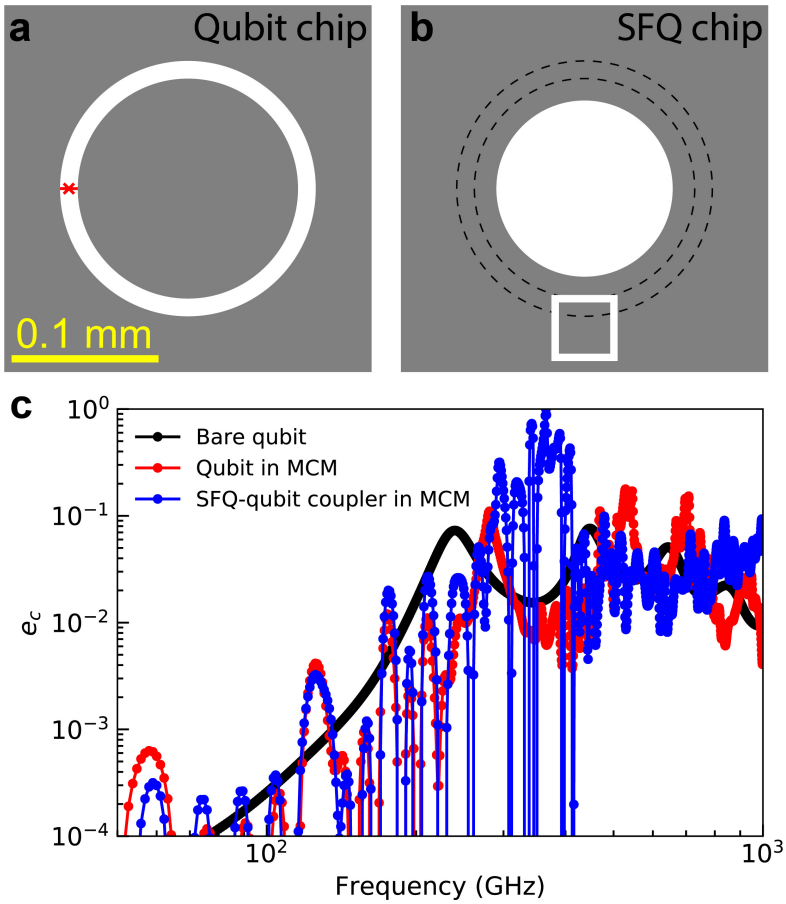

Figure 8.7: Antenna modeling of the qubit and the SFQ-qubit coupler. Schematic of **a** the qubit and **b** the region opposite the qubit on the classical SFQ driver chip. Here, gray represents Nb metallization on the two chips; in the white regions, the Nb has been etched away. The Nb has been removed in a circular region on the classical chip directly opposite the qubit island in order to reduce the capacitance between the qubit and the groundplane of the classical chip. In **a**, the position of the qubit junction is indicated by the red cross. In **b**, the concentric black dashed lines indicate the position of the gap between the qubit island and groundplane relative to structures on the SFQ driver chip. The patch capacitor that couples SFQ pulses to the qubit is shown at bottom; this SFQ-qubit coupler is fed from the bottom of the image by a microstrip line from the classical SFQ driver circuit. **c**, Numerically calculated free-space coupling efficiency e_c of the antenna modes of the qubit and of the SFQ-qubit coupler [35]. The black curve represents e_c of the qubit with the SFQ chip removed; the dominant feature at 250 GHz corresponds to the fundamental full-wave resonance of the aperture antenna formed by the qubit island embedded in the groundplane. The red and blue traces are simulation results for e_c of the qubit and SFQ coupler modes calculated in the full MCM architecture.

frequency-dependent coupling efficiency with peaks in the resonant response around 300 GHz. Similarity in the coupling efficiency of the qubit and SFQ coupler could be due to loading of both modes by the etched cavity in the groundplane of the SFQ driver chip; see Sec. 9.1.3 for more details.

After verifying that the SFQ-qubit pair can be considered as a coupled antenna system, we show that the ps-scale SFQ pulse indeed leads to emission of photons with energy sufficient to break Cooper pairs; see Sec. 9.6 for a detailed discussion.

From our analysis of QP poisoning presented in Fig. 8.5, a single SFQ pulse delivered to the qubit generates 1.1×10^{-4} QP at the qubit junction. We can ask the question: if all the energy that goes into QP generation is derived from SFQ-qubit antenna coupling, what is the efficiency of energy transfer from the driver to the qubit? We define an energy conversion factor α as follows:

$$\alpha E_{\mathrm{SFQ}} = 1.1 \times 10^{-4} \times E_{\mathrm{qp}}, \tag{8.3}$$

where E_{SFQ} is the available energy from one SFQ pulse and E_{qp} is the energy of one QP. We take the available energy per SFQ pulse to be equal to the phase slip energy, and for simplicity we assume that the generated QPs are concentrated at the gap edge of Al. We find

$$E_{\mathrm{SFQ}} = I_c \Phi_0, \tag{8.4}$$

$$E_{\mathrm{qp}} = h \times 50 \text{ GHz}, \tag{8.5}$$

where $I_c \sim 100$ μA is the critical current of the output junction of the SFQ driver. Solving the equations above, we find an experimental energy conversion efficiency $\alpha_{\mathrm{exp}} = 1.8 \times 10^{-8}$.

We can compare the experimentally extracted α with the result derived from

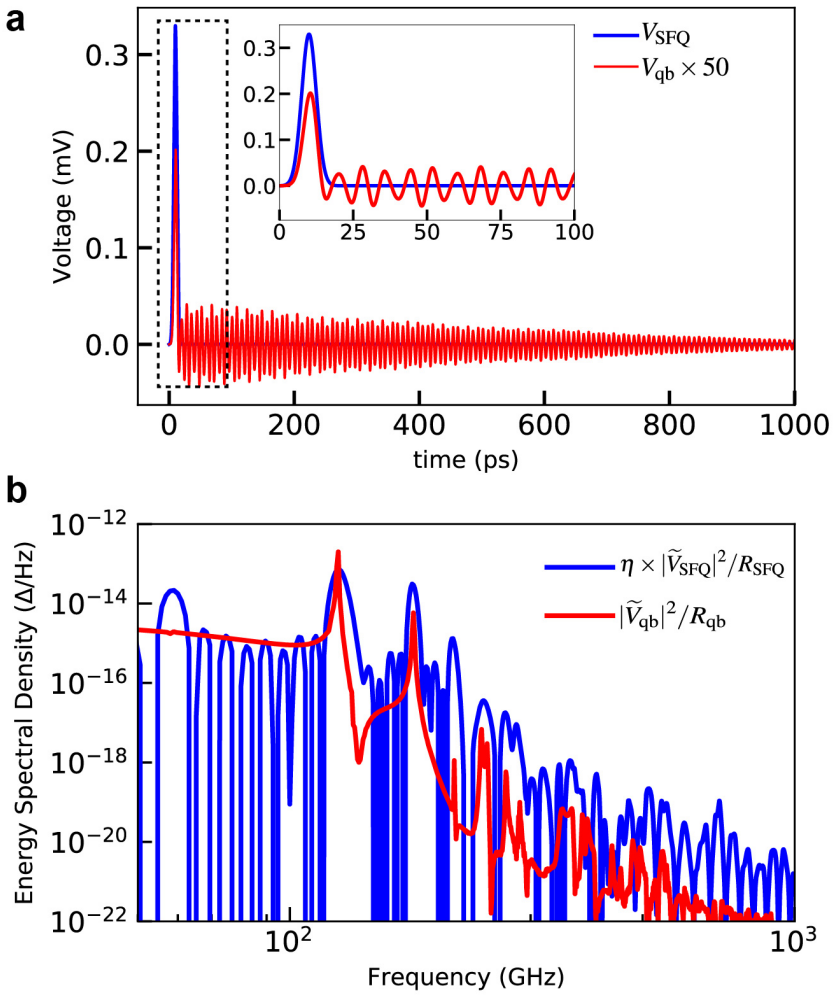

Figure 8.8: Temporal response of the qubit antenna mode to a single SFQ pulse. **a**, SFQ pulse and induced transient at the qubit. A single SFQ pulse V_{SFQ} with $\sigma = 2.5$ ps is delivered from the SFQ-qubit coupler (blue trace). Antenna coupling between the SFQ-qubit coupler and the qubit results in an induced voltage V_{qb} at the qubit port (red trace; voltage scaled by a factor of 50 for clarity). **b**, Energy spectral density of the qubit response expressed in units of Δ/Hz, where $\Delta = E_{\mathrm{qp}} = h \times 50$ GHz. The red trace is the energy spectral density calculated from the qubit transient in **a**; here, $\widetilde{V}_{\mathrm{qb}}$ is the Fourier transform of the induced voltage at the qubit, and R_{qb} is the normal state resistance of the qubit junction. The blue trace shows the product of the photon coupling efficiency η based on the frequency-domain antenna modeling and the energy spectral density of the SFQ pulse. The dominant Fourier component in the qubit response matches the product of the energy spectral density of the SFQ pulse and the photon coupling efficiency of the coupler-qubit system.

time-domain modeling of the coupled antenna system. We take $R_{\mathrm{SFQ}} = 1\ \Omega$ as the source impedance associated with the SFQ-qubit coupler, and we model the SFQ transient as a Gaussian pulse with width $\sigma = 2.5$ ps, derived from WRspice [118] simulation of our dc/SFQ converter. As shown in Fig. 8.8a, the SFQ pulse applied to the coupler (blue) induces an oscillatory voltage response at the qubit junction port (red, scaled by a factor 50), with a dominant frequency set by the product of the energy spectral density of the SFQ pulse and the photon coupling efficiency of the coupler-qubit system. In Fig. 8.8b, we show in red the energy spectral density of the response signal at the qubit port $|\widetilde{V}_{\mathrm{qb}}|^2/R_{\mathrm{qb}}$; here, $\widetilde{V}_{\mathrm{qb}}$ is the Fourier transform of the voltage induced at the qubit port and $R_{\mathrm{qb}} = 8.0\ \mathrm{k}\Omega$ is the normal state resistance of the junction. As in [37], we define the photon coupling efficiency η as:

$$\eta(f) = e_{c,\mathrm{qb}}\, e_{c,\mathrm{coupler}}, \tag{8.6}$$

where f is frequency and $e_{c,\mathrm{qb}}$ ($e_{c,\mathrm{coupler}}$) is the coupling efficiency of the qubit (coupler) calculated in Fig. 8.7c. In Fig. 8.8b, we plot in blue the available energy spectral density from the SFQ pulse $|\widetilde{V}_{\mathrm{SFQ}}|^2/R_{\mathrm{SFQ}}$ scaled by the coupling efficiency η. The close agreement with the spectrum calculated from the voltage transient at the qubit junction suggests that transport of pair-breaking energy between the SFQ coupler and the qubit is dominated by direct antenna coupling between the structures.

From our modeling, we calculate the total energy dissipated at the qubit port for photons with a frequency above 100 GHz, and we find a simulated energy conversion factor $\alpha_{\mathrm{sim}}(\sigma = 2.5\ \mathrm{ps}) = 3.8 \times 10^{-8}$, in reasonable agreement with the experimental value $\alpha_{\mathrm{exp}} = 1.8 \times 10^{-8}$. For the sake of completeness, we have also simulated antenna coupling to the qubit of SFQ pulses with varying widths. For SFQ pulse

widths $\sigma = 0.5, 1, 2$, and 5 ps, we find energy conversion efficiency $\alpha_{\text{sim}} = 1.3 \times 10^{-5}, 1.3 \times 10^{-6}, 9.7 \times 10^{-8}$, and 1.0×10^{-12}, respectively. It is clear that broader SFQ pulses, for which the energy is compressed into a narrower spectral band, lead to a suppression of antenna-mediated QP poisoning at the qubit. As the typical qubit oscillation period ∼200 ps is orders of magnitude longer than typical SFQ pulse widths, a straightforward redesign of the SFQ driver to suppress the spectral weight of the SFQ transient above 100 GHz provides an obvious path to eliminating photon-mediated QP poisoning. Deviation of the SFQ pulse from the ideal delta-function will cause misrotation of the qubit state vector on the Bloch sphere [104]; however, this is a coherent error that is readily addressed by appropriate gate calibration.

8.6 Conclusion

In this work, we have advanced the state of the art for SFQ-based digital control of superconducting qubits. By segregating qubits and classical control elements on separate chips in an MCM architecture, we suppress phonon-mediated QP poisoning and achieve an error per Clifford gate of 1.2(1)%. This gate infidelity represents a one-order-of-magnitude reduction compared to the first demonstration of SFQ-based qubit control [46], and a factor-of-two reduction in the infidelity achieved in recent work involving a 3D transmon controlled by a Josephson pulse generator located at the 3 K stage of the cryostat [104]. We find that residual gate infidelity is dominated by photon-assisted QP poisoning mediated via spurious mm-wave antenna modes of the qubit and SFQ-qubit coupler. To suppress QP generation at the qubit from the high-bandwidth SFQ pulse, we suggest a modest redesign of the SFQ driver circuit to yield SFQ pulses with broader characteristic temporal width, corresponding to a narrower pulse bandwidth in the frequency domain. Such a redesign will concentrate

the power emitted by the SFQ driver below the aluminum gap edge, so that QP generation is not possible. The qubit and the SFQ-qubit coupler could also be modified to suppress their antenna coupling to free space at frequencies just above the aluminum gap [35, 37, 36]. To protect the qubit from any residual nonequilibrium QPs, appropriate superconductor gap engineering [109, 119, 120, 58, 23] could be harnessed to promote the rapid outflow of QPs from the qubit junction and to prevent the inflow to the junction of QPs from remote parts of the qubit circuit. With these steps to mitigate the various forms of nonequilibium QP poisoning, SFQ gate fidelity of 99.9% is achievable using resonant SFQ pulse trains [83]. Ultimately, more complex control sequences involving nonuniform SFQ pulse spacing should enable single-qubit gate fidelity of 99.99%, on par with that achieved using microwave-based gates, but with a significant reduction in hardware footprint for the control system.

Chapter 9

Supplemental Information for "Single Flux Quantum-Based Digital Control of Superconducting Qubits in a Multi-Chip Module"

9.1 Fabrication of the Quantum-Classical MCM

9.1.1 Qubit

The qubit chip was fabricated on a high resistivity (> 10 kΩ-cm) 3-inch Si substrate with 100 crystal orientation. The native oxide of the silicon is stripped in dilute (2%) hydrofluoric acid for 60 seconds immediately prior to transfer of the wafer into the sputter deposition chamber used for growth of the 100-nm Nb base electrode.

We use an i-line projection lithography tool to define the qubit islands and readout resonators. We then etch the Nb using BCl_3/Cl_2 chemistry in an inductively coupled plasma reactive ion etch tool. We use an electron-beam writer to define the Dolan bridges for the qubit junctions; the $Al/AlO_x/Al$ junctions are then formed by double-angle evaporation and thermal oxidation in an electron-beam evaporator.

9.1.2 SFQ Driver

The driver circuits were fabricated at the NIST Boulder Microfabrication Facility. The substrates used were 3–inch Si wafers with 150 nm of thermal oxide. The fabrication of the drivers was based on the process for SFQ digital circuits described in [121] with the following changes:

1. Only three superconducting layers were used, requiring only one chemical–mechanical–planarization step before deposition of the second Nb layer;

2. The top Nb layer was used as the ground plane;

3. The barrier material used for the SIS junctions was amorphous Si, and external shunt resistors were needed to bring the damping of these SIS junctions near the critical regime with Stewart-McCumber parameter $\beta_c \sim 2$;

4. The critical current density of the junctions is 1 kA/cm^2 and the characteristic junction frequency is 240 GHz;

5. The shunt resistors were made of palladium/gold alloy films with sheet resistance of 2 Ω / $\square$ deposited by electron–beam evaporation and defined by a two–layer lift–off resist process.

9.1.3 MCM

The fabrication steps for the under-bump and indium bump layers deposited on each chip are similar to those described in [122] but with a target bump thickness of 5 μm. Additionally, hydrogen plasma cleaning before bonding is avoided to prevent potential contamination of Nb layers used both in the SFQ and qubit chips. The MCM is bonded in a commercial flip-chip bonder. Before bonding, the components are aligned to $\pm$ 1.0 μm. The coplanarity is adjusted to be less than 100 μradians. The bonding force used was 21.6 kN, which, given optical profilometer measurements of the bump thickness (4.6 $\pm$ 0.2 μm) and top contact area (260 μm^2) for the 2193 bumps on each chip, results in a calculated effective pressure of 3.9×10^{10} N/m^2 and an expected resulting chip gap of 6.4 $\pm$ 0.3 μm.

9.2 Wiring

The experimental setup and wiring are shown in Fig. 9.1.

9.3 Impact of SFQ Pulse Errors

In addition to incoherent error from QP poisoning, the instability of SFQ pulse delivery represents another potential error channel. In Fig.8.2a, we see that the Rabi frequency associated with resonant SFQ drive is not a constant over the full range of current bias; similar behavior was seen in [46, 104]. In Fig. 9.2a, we plot the extracted Rabi frequency versus bias current. We find relative variation in the Rabi frequency of order 5% over the bias current range considered. In the following, we examine the possibility that this variation is due to SFQ driver errors, namely, missed SFQ pulses or delivery of double pulses, and we estimate the resulting contribution to

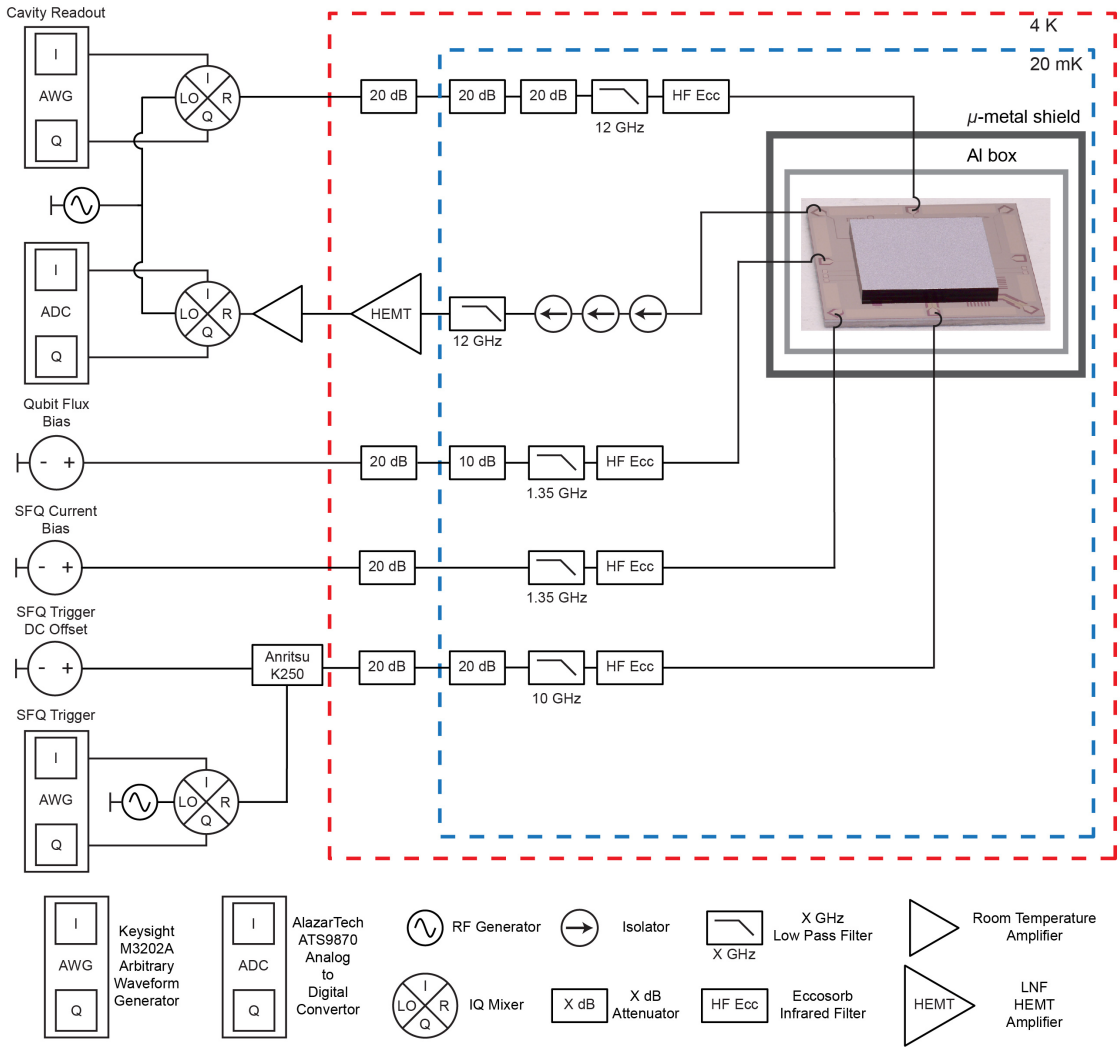

Figure 9.1: **Wiring diagram of the experiments.**

SFQ gate error. Pulse dropouts will result in systematic underrotation of the qubit state and a reduction in Rabi frequency, while double pulses will cause overrotation of the qubit and an increase in Rabi frequency.

We define the SFQ pulse probability P_{SFQ} in three regimes. For $P_{\mathrm{SFQ}} < 1$, one pulse is delivered per clock cycle with probability P_{SFQ}; the probability of a pulse dropout is $1 - P_{\mathrm{SFQ}}$. For $P_{\mathrm{SFQ}} = 1$, exactly one SFQ pulse is delivered per cycle of the trigger waveform. Finally, for $P_{\mathrm{SFQ}} > 1$, a double SFQ pulse is delivered with probability $P_{\mathrm{SFQ}} - 1$, while a single SFQ pulse is delivered with probability $2 - P_{\mathrm{SFQ}}$.

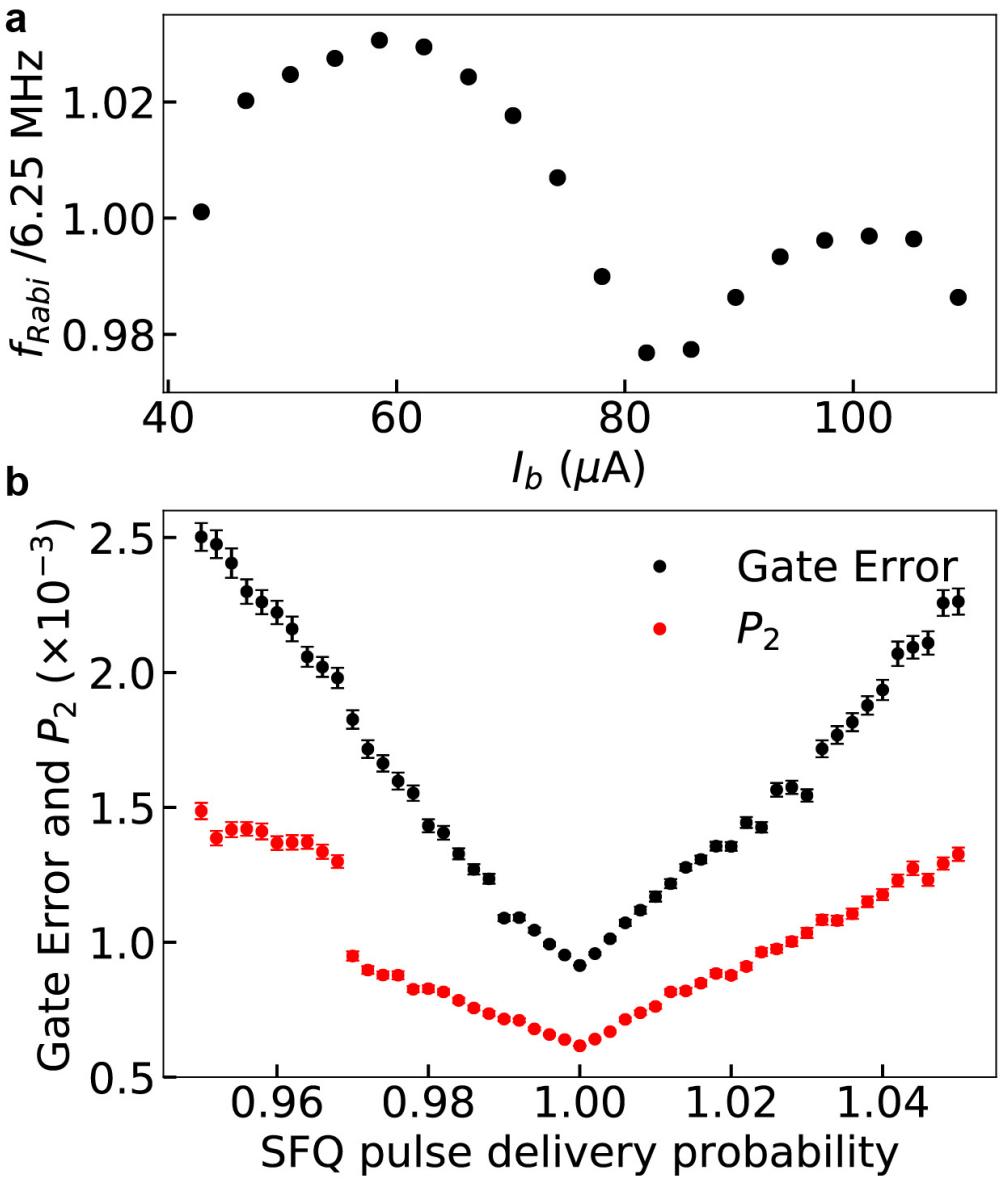

Figure 9.2: Stability of SFQ pulse delivery and its effect on qubit control. **a**, Scaled Rabi oscillation frequency f_{Rabi} extracted from Fig. 8.2a as a function of I_b. Over a bias current range from 40 to 120 μA, we find approximately $\pm$ 3% variation in f_{Rabi} around the value 6.25 MHz. A possible explanation for the variation in Rabi frequency is that the number of SFQ pulses delivered per cycle of the trigger waveform is either less than or greater than one. **b**, Simulated gate error and leakage to the $|2\rangle$ state for a $\pi/2$ gate implemented with an imperfect SFQ pulse driver. Gate error and leakage both increase in the presence of SFQ pulse dropouts and double pulses.

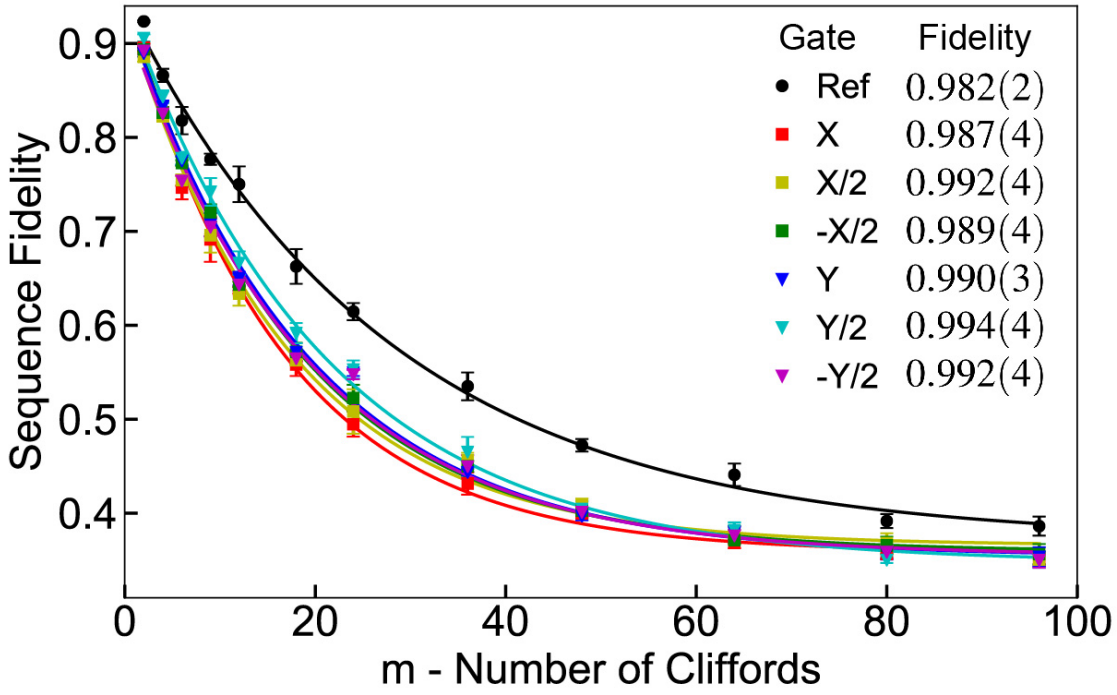

Figure 9.3: IRB of resonant SFQ-based gates implemented at drive frequency $f_{01}/2$.

Following [83], we perform Monte Carlo simulations of the gate error and leakage to the $|2\rangle$ state for a $Y/2$ gate realized with the parameters of the SFQ driver-qubit pair used in these experiments; simulation results are shown in Fig. 9.2b. We find increased gate error and leakage as the probability of pulse dropouts or double pulses increases. For pulse dropout or double pulse probability less than 3%, compatible with the variation in Rabi frequency over the bias current range from 40 μA to 120 μA, we put an upper bound on gate error of $\sim$ 0.2%. While instability of the SFQ driver does not currently limit gate fidelity, it is possible that SFQ pulse errors will be a dominant source of infidelity in SFQ gates once QP poisoning is fully suppressed.

9.4 SFQ-Qubit Parameters

In Table 9.1, we list the measured and extracted parameters of the SFQ-qubit pair used in these experiments.

Table 9.1: **Parameters of devices used in the experiments.** Resonator and qubit frequencies are measured by spectroscopy. Qubit baseline coherence times T_1 and $T_{2,\text{white}}$ are extracted from microwave-based inversion recovery and echo sequences. $T_{1,\text{qp}}$ is extracted from nonlinear fits to the inversion recovery signals shown in Fig. 8.5. The SFQ operation parameters, including trigger frequency, trigger power, trigger DC offset and current bias, are chosen to maximize SFQ-based qubit gate fidelity. The SFQ-qubit coupling capacitance is calculated following [83] from the measured Rabi frequency shown in Fig. 9.2a.

Description	Symbol	Value
Readout resonator frequency	f_{RO}	6.786 GHz
Qubit max operating frequency	f_{01}	4.906 GHz
Qubit energy relaxation time	T_1	26 μs
Qubit phase relaxation time	$T_{2,\text{white}}$	20 μs
Qubit energy relaxation time per QP	$T_{1,\text{qp}}$	6.8 μs
SFQ trigger frequency	$\omega_{\text{SFQ}}/2\pi$	1.226 GHz
SFQ trigger power		-45 dBm
SFQ trigger DC offset		90 μA
SFQ current bias	I_b	80 μA
SFQ-qubit coupling capacitance	C_{SFQ}	180 aF

9.5 Characterization of SFQ-Based Gates with Drive at $f_{01}/2$

We have also used IRB to characterize SFQ-based control at the first subharmonic $f_{01}/2$ of the qubit fundamental frequency; results are shown in Fig. 9.3. The average error per Clifford gate is 1.8(2)%, which is slightly higher than the result obtained at a drive frequency $f_{01}/4$. It is likely that the degraded fidelity at the higher drive

frequency is due to the higher rate of photon-assisted QP generation associated with the shorter interpulse spacing.

9.6 Frequency-Domain Analysis of SFQ Pulses

We consider an SFQ pulse with Gaussian envelope in the time domain:

$$V_{\mathrm{SFQ}}(t) = \frac{\Phi_0}{\sqrt{2\pi}\sigma} e^{\frac{-t^2}{2\sigma^2}}, \tag{9.1}$$

where Φ_0 is the magnetic flux quantum and σ is the standard deviation of the pulse in time. The Fourier transform of the SFQ pulse is given by

$$\widetilde{V}_{\mathrm{SFQ}}(f) = \Phi_0 e^{-\frac{f^2}{2\sigma_f^2}}, \tag{9.2}$$

where $\sigma_f = (2\pi\sigma)^{-1}$ is the standard deviation of the pulse in the frequency domain. For typical Nb-based SFQ devices [98], σ is around 1 ps. In Fig. 9.4, we plot $\widetilde{V}_{\mathrm{SFQ}}(f)$ for Gaussian SFQ pulses with four values of σ. For shorter pulses, the SFQ transient involves significant spectral weight at frequencies above the Al energy gap ($\sim$ 100 GHz). Pair-breaking photons emitted by the transient can couple resonantly to the qubit structure via the spurious mm-wave antenna modes of the device. To suppress this form of QP poisoning, it is possible to intentionally broaden the SFQ pulses by increasing the damping of the SFQ driver. As the qubit oscillation period is two orders of magnitude larger than the SFQ pulse width, broadening the SFQ pulse to, say, $\sigma = 5$ ps will have negligible effect on the coherent qubit rotation induced by the SFQ pulse.

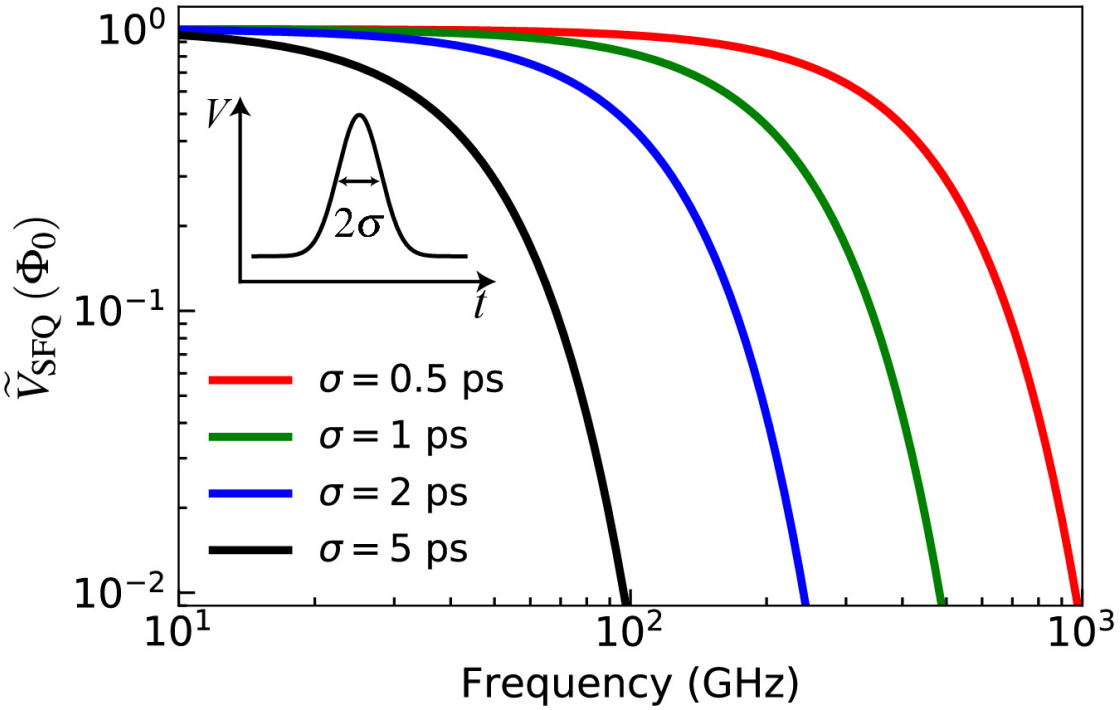

Figure 9.4: Fourier transform of Gaussian SFQ pulses with varying standard deviation σ from 0.5-5 ps. In the Fourier domain representation of the pulse, the standard deviation is $\sigma_f = (2\pi\sigma)^{-1}$. Narrower SFQ pulses in the time domain involve more spectral weight above the Al energy gap $2\Delta_{\mathrm{Al}}/h \sim 100$ GHz, where there is the possibility of photon-assisted QP generation.

Chapter 10

Conclusion

In this thesis, we have explored two topics of superconducting qubits: the quasiparticle poisoning of superconducting qubits through resonant absorption of pair-breaking photons and SFQ digital control of superconducting qubits in an MCM.

In the first project, we have presented experimental validation of a model for the antenna coupling of qubits to pair-breaking radiation. The validation was carried out through controlled irradiation of superconducting qubits with mm-wave photons derived from the ac Josephson effect. The model's detailed predictions regarding the absorption spectrum of the qubits were confirmed by mapping out their spectral response up to 500 GHz. Our findings demonstrate that resonant absorption of pair-breaking photons is the dominant contributor to qubit initialization errors in our devices, while the observed baseline parity switching rates are explained well by absorption of broadband thermal photons. These results provide a deeper understanding of the physical mechanism for quasiparticle poisoning, which could help develop new qubit designs that are robust against pair-breaking radiation.

Furthermore, our experiments have shown that the resonant transduction of pair-breaking photons to quasiparticles followed by qubit-based parity detection

could lead to a new class of quantum sensors for high-resolution spectroscopy in the frequency range from 100 GHz to 1 THz, where established detection techniques are limited. This has important implications for the detection of dark-matter axions or dark energy, as well as for high-resolution spectroscopy of the cosmic microwave background.

In conclusion, our validated model for photon-assisted quasiparticle poisoning through the spurious antenna modes of the transmon qubit provides a detailed understanding of the physical mechanism for quasiparticle poisoning and paves the way for the development of new qubit designs and measurement configurations that protect against absorption of pair-breaking radiation. Our results also suggest the possibility of using qubits as high-resolution detectors for a range of applications in the 100 GHz to 1 THz frequency range.

In our second project, we have proposed the SFQ digital superconducting logic family for the scalable control of next-generation superconducting qubit arrays. However, the initial implementation had limited SFQ-based gate fidelity due to quasiparticle (QP) poisoning induced by the dissipative on-chip SFQ driver circuit.

To address this issue, we have introduced a multi-chip module architecture that segregates SFQ elements and qubits onto separate chips, which are joined with In bump bonds. Through interleaved randomized benchmarking, we have characterized the fidelity of SFQ-based gates, and have achieved an error per Clifford gate of 1.2(1)%, representing an order-of-magnitude reduction over the gate error achieved in the initial realization of SFQ-based qubit control.

Using purity benchmarking, we have quantified the contribution of incoherent error at 0.96(2)%, which we attribute to photon-mediated QP poisoning mediated by the resonant mm-wave antenna modes of the qubit and SFQ-qubit coupler. To eliminate this source of infidelity, we anticipate that a straightforward redesign of the

SFQ driver circuit to limit the bandwidth of the SFQ pulses will be necessary, allowing SFQ-based gates with fidelity approaching theoretical limits, namely 99.9% for resonant sequences and 99.99% for more complex pulse sequences involving variable pulse-to-pulse separation.

Overall, our work has advanced the state of the art for SFQ-based digital control of superconducting qubits. By segregating qubits and classical control elements on separate chips in an MCM architecture, we have suppressed phonon-mediated QP poisoning and achieved a significant reduction in gate infidelity. To further improve gate fidelity, we propose modifications to the SFQ driver circuit, qubit, and SFQ-qubit coupler to suppress antenna coupling and promote the rapid outflow of QPs from the qubit junction. Ultimately, with these steps to mitigate the various forms of nonequilibium QP poisoning, SFQ gate fidelity of 99.9% is achievable using resonant SFQ pulse trains, while more complex control sequences involving nonuniform SFQ pulse spacing should enable single-qubit gate fidelity of 99.99%.

Bibliography

[1] Arute, F. *et al.* Quantum supremacy using a programmable superconducting processor. *Nature* **574**, 505–510 (2019).

[2] Loss, D. & DiVincenzo, D. P. Quantum computation with quantum dots. *Phys. Rev. A* **57** (1998).

[3] Weber, J. R. *et al.* Quantum computing with defects. *Proceedings of the National Academy of Sciences of the United States of America* **107**, 8513–8518 (2010).

[4] Leibfried, D., Blatt, R., Monroe, C. & Wineland, D. Quantum dynamics of single trapped ions. *Reviews of Modern Physics* **75**, 281–324 (2003).

[5] Saffman, M., Walker, T. G. & Mølmer, K. Quantum information with Rydberg atoms. *Reviews of Modern Physics* **82**, 2313–2363 (2010).

[6] Zhong, H. S. *et al.* Quantum computational advantage using photons. *Science* **370**, 1460–1463 (2020).

[7] Josephson, B. D. Possible new effects in superconductive tunnelling. *Phys. Lett.* **1**, 251–253 (1962).

[8] Ambegaokar, V. & Baratoff, A. Tunneling between superconductors. *Physical Review Letters* **11**, 104 (1963).

[9] Clarke, J. & Wilhelm, F. Superconducting quantum bits. *Nature* **453**, 1031–1042 (2008).

[10] Koch, J. *et al.* Charge-insensitive qubit design derived from the Cooper pair box. *Physical Review A* **76**, 1–19 (2007).

[11] Manucharyan, V. E., Koch, J., Glazman, L. I. & Devoret, M. H. Fluxonium: Single Cooper-Pair Circuit Free of Charge Offsets. *Science* **326**, 113–116 (2009).

[12] Soloviev, I. I. *et al.* Beyond Moore's technologies: Operation principles of a superconductor alternative. *Beilstein Journal of Nanotechnology* **8**, 2689–2710 (2017).

[13] Tinkham, M. *Introduction to Superconductivity* (McGraw-Hill, New York, 1996).

[14] Blais, A., Grimsmo, A. L., Girvin, S. M. & Wallraff, A. Circuit quantum electrodynamics. *Reviews of Modern Physics* **93**, 25005 (2021).

[15] Chen, Z. *Metrology of Quantum Control and Measurement in Superconducting Qubits*. Ph.D. thesis (2018).

[16] Barends, R. *et al.* Superconducting quantum circuits at the surface code threshold for fault tolerance. *Nature* **508**, 500–503 (2014).

[17] Hutchings, M. D. *et al.* Tunable superconudcting qubits with flux-independent coherence arXiv:1702.02253 (2017).

[18] Diamond, S. *et al.* Distinguishing Parity-Switching Mechanisms in a Superconducting Qubit. *PRX Quantum* **3** (2022).

[19] Chen, Y. *et al.* Qubit architecture with high coherence and fast tunable coupling. *Physical Review Letters* **113**, 1–5 (2014).

[20] Devoret, M., Girvin, S. & Schoelkopf, R. Circuit-QED: How strong can the coupling between a Josephson junction atom and a transmission line resonator be? *Annalen der Physik (Leipzig)* **16**, 767–779 (2007).

[21] Blais, A., Huang, R. S., Wallraff, A., Girvin, S. M. & Schoelkopf, R. J. Cavity quantum electrodynamics for superconducting electrical circuits: An architecture for quantum computation. *Physical Review A - Atomic, Molecular, and Optical Physics* **69**, 1–14 (2004).

[22] Glazman, L. I. & Catelani, G. Bogoliubov quasiparticles in superconducting qubits Superconductivity in an isolated metallic island Electron pairing and condensate. *SciPost Phys. Lect.Notes* **31**, 1–40 (2021).

[23] Catelani, G. & Pekola, J. P. Using materials for quasiparticle engineering. *Materials for Quantum Technology* **2**, 013001 (2022).

[24] Catelani, G. *et al.* Quasiparticle relaxation of superconducting qubits in the presence of flux. *Physical Review Letters* **106**, 4–7 (2011).

[25] Vepsäläinen, A. P. *et al.* Impact of ionizing radiation on superconducting qubit coherence. *Nature* **584**, 551–556 (2020).

[26] Wilen, C. *et al.* Correlated charge noise and relaxation errors in superconducting qubits. *Nature* **594**, 369–373 (2021).

[27] McEwen, M. *et al.* Resolving catastrophic error bursts from cosmic rays in large arrays of superconducting qubits. *Nature Physics* **18**, 107–111 (2021).

[28] Aumentado, J., Keller, M. W., Martinis, J. M. & Devoret, M. H. Nonequilibrium quasiparticles and $2e$ periodicity in single-Cooper-pair transistors. *Phys. Rev. Lett.* **92**, 066802 (2004).

[29] Shaw, M. D., Lutchyn, R. M., Delsing, P. & Echternach, P. M. Kinetics of nonequilibrium quasiparticle tunneling in superconducting charge qubits. *Physical Review B - Condensed Matter and Materials Physics* **78** (2008).

[30] Martinis, J. M., Ansmann, M. & Aumentado, J. Energy decay in superconducting Josephson-junction qubits from nonequilibrium quasiparticle excitations. *Phys. Rev. Lett.* **103**, 097002 (2009).

[31] Vool, U. *et al.* Non-Poissonian quantum jumps of a fluxonium qubit due to quasiparticle excitations. *Phys. Rev. Lett.* **113**, 247001 (2014).

[32] Wang, C. *et al.* Measurement and control of quasiparticle dynamics in a superconducting qubit. *Nat. Commun.* **5**, 5836 (2014).

[33] De Visser, P. J., Baselmans, J. J., Bueno, J., Llombart, N. & Klapwijk, T. M. Fluctuations in the electron system of a superconductor exposed to a photon flux. *Nature Communications* **5**, 3130 (2014).

[34] Houzet, M., Serniak, K., Catelani, G., Devoret, M. H. & Glazman, L. I. Photon-assisted charge-parity jumps in a superconducting qubit. *Physical Review Letters* **123**, 107704 (2019).

[35] Rafferty, O. *et al.* Spurious Antenna Modes of the Transmon Qubit (2021).

[36] Pan, X. *et al.* Engineering superconducting qubits to reduce quasiparticles and charge noise. *Nature Communications* **13:7196** (2022).

[37] Liu, C.-H. *et al.* Quasiparticle Poisoning of Superconducting Qubits from Resonant Absorption of Pair-breaking Photons 1–13 (2022).

[38] Anthony-Petersen, R. *et al.* A Stress Induced Source of Phonon Bursts and Quasiparticle Poisoning 1–13 (2022).

[39] Day, P., LeDuc, H., Mazin, B., Anastasios, V. & Zmuidzinas, J. A broadband superconducting detector suitable for use in large arrays. *Nature* **425**, 817–821 (2003).

[40] Pop, I. M. *et al.* Coherent suppression of electromagnetic dissipation due to superconducting quasiparticles. *Nature* **508**, 369–372 (2014).

[41] Siddiqi, I. Engineering high-coherence superconducting qubits. *Nature Reviews Materials* (2021).

[42] Catelani, G. & Basko, D. M. Non-equilibrium quasiparticles in superconducting circuits: Photons vs. Phonons. *SciPost Physics* **6**, 1–21 (2019).

[43] Serniak, K. *et al.* Hot Nonequilibrium Quasiparticles in Transmon Qubits. *Physical Review Letters* **121**, 157701 (2018).

[44] Grünhaupt, L. *et al.* Loss Mechanisms and Quasiparticle Dynamics in Superconducting Microwave Resonators Made of Thin-Film Granular Aluminum. *Physical Review Letters* **121**, 117001 (2018).

[45] Lenander, M. *et al.* Measurement of energy decay in superconducting qubits from nonequilibrium quasiparticles. *Phys. Rev. B* **84**, 024501 (2011).

[46] Leonard, E. *et al.* Digital Coherent Control of a Superconducting Qubit. *Physical Review Applied* **11**, 1–13 (2019).

[47] Ristè, D. *et al.* Millisecond charge-parity fluctuations and induced decoherence in a superconducting transmon qubit. *Nature Communications* **4**, 1–6 (2013).

[48] Tennant, D. M. *et al.* Low-Frequency Correlated Charge-Noise Measurements Across Multiple Energy Transitions in a Tantalum Transmon. *PRX Quantum* **3**, 1 (2022).

[49] Thorbeck, T., Eddins, A., Lauer, I., McClure, D. T. & Carroll, M. TLS Dynamics in a Superconducting Qubit Due to Background Ionizing Radiation 1–14 (2022).

[50] Serniak, K. *et al.* Direct Dispersive Monitoring of Charge Parity in Offset-Charge-Sensitive Transmons. *Physical Review Applied* **12** (2019).

[51] Cardani, L. *et al.* Reducing the impact of radioactivity on quantum circuits in a deep-underground facility. *Nature Communications* **12**, 1–15 (2021).

[52] Vepsäläinen, A. P. *et al.* Impact of ionizing radiation on superconducting qubit coherence. *Nature* **584**, 551–556 (2020).

[53] Iaia, V. *et al.* Phonon downconversion to suppress correlated errors in superconducting qubits. *Nature Communications* **13** (2022).

[54] Danilin, S. *et al.* Engineering the microwave to infrared noise photon flux for superconducting quantum systems. *EPJ Quantum Technology* **9**, 1–22 (2022).

[55] Rehammar, R. & Gasparinetti, S. Low-pass filter with ultra-wide stopband for quantum computing applications 1–6 (2022).

[56] Karatsu, K. *et al.* Mitigation of cosmic ray effect on microwave kinetic inductance detector arrays. *Applied Physics Letters* **114** (2019).

[57] Henriques, F. *et al.* Phonon traps reduce the quasiparticle density in superconducting circuits. *Applied Physics Letters* **115**, 1–14 (2019).

[58] Bargerbos, A. *et al.* Mitigation of quasiparticle loss in superconducting qubits by phonon scattering. *arXiv:2207.12754* **1** (2022).

[59] Liu, C.-H. *et al.* Single Flux Quantum-Based Digital Control of Superconducting Qubits in a Multi-Chip Module. *Arxiv* **2301** (2023).

[60] Sun, L. *et al.* Measurements of quasiparticle tunneling dynamics in a band-gap-engineered transmon qubit. *Physical Review Letters* **108**, 1–5 (2012).

[61] Barends, R. *et al.* Loss and decoherence due to stray infrared light in superconducting quantum circuits **113507**, 1–4 (2011).

[62] Patel, U., Pechenezhskiy, I. V., Plourde, B. L., Vavilov, M. G. & McDermott, R. Phonon-mediated quasiparticle poisoning of superconducting microwave resonators. *Physical Review B* **96**, 1–5 (2017).

[63] Wang, C. *et al.* Measurement and control of quasiparticle dynamics in a superconducting qubit. *Nature Communications* **5**, 1–7 (2014).

[64] Mannila, E. T. *et al.* A superconductor free of quasiparticles for seconds. *Nature Physics* **18**, 6–10 (2021).

[65] Van Zanten, D. M. *et al.* Single Quantum Level Electron Turnstile. *Physical Review Letters* **116** (2016).

[66] Echternach, P. M., Pepper, B. J., Reck, T. & Bradford, C. M. Single photon detection of 1.5 THz radiation with the quantum capacitance detector. *Nature Astronomy* **2**, 90–97 (2018).

[67] Gustavsson, S. *et al.* Suppressing relaxation in superconducting qubits by quasiparticle pumping. *Science* **354**, 1573–1577 (2016).

[68] Barends, R. *et al.* Contribution of dielectrics to frequency and noise of NbTiN superconducting resonators. *Appl. Phys. Lett.* **92**, 223502 (2008).

[69] Córcoles, A. D. *et al.* Protecting superconducting qubits from external sources of loss and heat **1**, 1–4 (2011).

[70] Balanis, C. A. *Antenna Theory: Analysis and Design* (Wiley, 2016).

[71] Cassidy, M. C. *et al.* Demonstration of an ac Josephson junction laser. *Science* **355**, 939–942 (2017).

[72] Pan, X. *et al.* Engineering superconducting qubits to reduce quasiparticles and charge noise. *Nature Communications* **13:7196** (2022).

[73] Wang, Z. *et al.* Quantum Microwave Radiometry with a Superconducting Qubit. *Physical Review Letters* **126**, 180501 (2021).

[74] Dixit, A. V. *et al.* Searching for Dark Matter with a Superconducting Qubit. *Physical Review Letters* **126**, 141302 (2021).

[75] Braine, T. *et al.* Extended Search for the Invisible Axion with the Axion Dark Matter Experiment. *Physical Review Letters* **124**, 101303 (2020).

[76] Ghosh, S., Ruddy, E. P., Jewell, M. J., Leder, A. F. & Maruyama, R. H. Searching for dark photons with existing haloscope data. *Physical Review D* **104**, 92016 (2021).

[77] Wellstood, F. C., Urbina, C. & Clarke, J. Hot-electron effects in metals. *Physical Review B* **49**, 5942–5955 (1994).

[78] Kautz, R. L., Zimmerli, G. & Martinis, J. Self-heating in the Coulomb-blockade electrometer. *Journal of Applied Physics* **73**, 2386–2396 (1993).

[79] Clark, A. F., Childs, G. E. & Wallace, G. H. Electrical resistivity of some engineering alloys at low temperatures. *Cryogenics* **10**, 295–305 (1970).

[80] Ambegaokar, V., Eckern, U. & Schön, G. Quantum dynamics of tunneling between superconductors. *Phys. Rev. Lett.* **48**, 1745 (1982).

[81] Kaplan, S. B. *et al.* Quasiparticle and phonon lifetimes in superconductors. *Physical Review B* **14**, 4854–4873 (1976).

[82] Shapiro, S. Josephson currents in Superconducting tunneling: The effect of microwaves and other observations. *Physical Review Letters* **11**, 80–82 (1963).

[83] McDermott, R. & Vavilov, M. G. Accurate Qubit Control with Single Flux Quantum Pulses. *Physical Review Applied* **2**, 1–10 (2014).

[84] Barends, R. *et al.* Superconducting quantum circuits at the surface code threshold for fault tolerance. *Nature* **508**, 500–503 (2014).

[85] Walter, T. *et al.* Rapid High-Fidelity Single-Shot Dispersive Readout of Superconducting Qubits. *Physical Review Applied* **7**, 1–11 (2017).

[86] Opremcak, A. *et al.* High-Fidelity Measurement of a Superconducting Qubit Using an On-Chip Microwave Photon Counter. *Physical Review X* **11**, 11027 (2021).

[87] Fowler, A. G., Mariantoni, M., Martinis, J. & Cleland, A. N. Surface codes: Towards practical large-scale quantum computation. *Physical Review A - Atomic, Molecular, and Optical Physics* **86** (2012).

[88] Zhao, Y. *et al.* Realization of an Error-Correcting Surface Code with Superconducting Qubits. *Physical Review Letters* **129**, 30501 (2021).

[89] Krinner, S. *et al.* Realizing repeated quantum error correction in a distance-three surface code. *Nature* **605**, 669–674 (2022).

[90] Acharya, R. *et al.* Suppressing quantum errors by scaling a surface code logical qubit 1–44 (2022).

[91] Krinner, S. *et al.* Engineering cryogenic setups for 100-qubit scale superconducting circuit systems. *EPJ Quantum Technology* **6** (2019).

[92] Magnard, P. *et al.* Microwave Quantum Link between Superconducting Circuits Housed in Spatially Separated Cryogenic Systems. *Physical Review Letters* **125**, 260502 (2020).

[93] Stefanazzi, L. *et al.* The QICK (Quantum Instrumentation Control Kit): Readout and control for qubits and detectors. *Review of Scientific Instruments* **93** (2022).

[94] Bardin, J. C. *et al.* Design and Characterization of a 28-nm Bulk-CMOS Cryogenic Quantum Controller Dissipating Less Than 2 mW at 3 K. *IEEE Journal of Solid-State Circuits* **54**, 3043–3060 (2019).

[95] Van DIjk, J. P. G. *et al.* A Scalable Cryo-CMOS Controller for the Wideband Frequency-Multiplexed Control of Spin Qubits and Transmons. *IEEE Journal of Solid-State Circuits* **55**, 2930–2946 (2020).

[96] Lecocq, F. *et al.* Control and readout of a superconducting qubit using a photonic link. *Nature* **591**, 575–579 (2021).

[97] Smith, J. P. *et al.* Flexible coaxial ribbon cable for high-density superconducting microwave device arrays. *IEEE Transactions on Applied Superconductivity* **31**, 3–7 (2021).

[98] Likharev, K. K. & Semenov, V. K. RSFQ Logic/Memory Family: A New Josephson-Junction Technology for Sub-Terahertz-Clock-Frequency Digital Systems. *IEEE Transactions on Applied Superconductivity* **1**, 3–28 (1991).

[99] Mukhanov, O. A. Energy-Efficient single flux quantum technology. *IEEE Transactions on Applied Superconductivity* **21**, 760–769 (2011).

[100] Opremcak, A. *et al.* Measurement of a Superconducting Qubit with a Microwave Photon Counter. *Science* **1242**, 1239–1242 (2018).

[101] Howington, C. *et al.* Interfacing Superconducting Qubits with Cryogenic Logic: Readout. *IEEE Transactions on Applied Superconductivity* **29** (2019).

[102] McDermott, R. *et al.* Quantum-classical interface based on single flux quantum digital logic. *Quantum Science and Technology* **3**, 1–14 (2018).

[103] Sirois, A. J., Castellanos-Beltran, M., Fox, A. E., Benz, S. P. & Hopkins, P. F. Josephson Microwave Sources Applied to Quantum Information Systems. *IEEE Transactions on Quantum Engineering* **1**, 1–7 (2021).

[104] Howe, L. *et al.* Digital Control of a Superconducting Qubit Using a Josephson Pulse Generator at 3 K. *PRX Quantum* **3**, 1 (2022).

[105] Liebermann, P. J. & Wilhelm, F. K. Optimal Qubit Control Using Single-Flux Quantum Pulses. *Physical Review Applied* **6**, 2–6 (2016).

[106] Li, K., McDermott, R. & Vavilov, M. G. Hardware-Efficient Qubit Control with Single-Flux-Quantum Pulse Sequences. *Physical Review Applied* **12**, 1 (2019).

[107] Jokar, M. R., Rines, R. & Chong, F. T. Practical implications of SFQ-based two-qubit gates. *Proceedings - 2021 IEEE International Conference on Quantum Computing and Engineering, QCE 2021* 402–412 (2021).

[108] Jokar, M. R. *et al.* DigiQ: A Scalable Digital Controller for Quantum Computers Using SFQ Logic **1**, 400–414 (2022).

[109] Riwar, R. P. & Catelani, G. Efficient quasiparticle traps with low dissipation through gap engineering. *Physical Review B* **100**, 144514 (2019).

[110] Gottesman, D. A Theory of Fault-Tolerant Quantum Computation. *Physical Review A* **57**, 30 (1997).

[111] Knill, E. *et al.* Randomized benchmarking of quantum gates. *Physical Review A - Atomic, Molecular, and Optical Physics* **77**, 1–7 (2008).

[112] Chow, J. M. *et al.* Optimized driving of superconducting artificial atoms for improved single-qubit gates. *Physical Review A - Atomic, Molecular, and Optical Physics* **82**, 2–5 (2010).

[113] Kelly, J. *et al.* Optimal quantum control using randomized benchmarking. *Physical Review Letters* **112**, 1–5 (2014).

[114] Magesan, E. *et al.* Efficient measurement of quantum gate error by interleaved randomized benchmarking. *Physical Review Letters* **109**, 1–5 (2012).

[115] Wallman, J., Granade, C., Harper, R. & Flammia, S. T. Estimating the coherence of noise. *New Journal of Physics* **17**, 0–13 (2015).

[116] O'Malley, P. J. *et al.* Qubit Metrology of Ultralow Phase Noise Using Randomized Benchmarking. *Physical Review Applied* **3**, 1–11 (2015).

[117] Catelani, G., Nigg, S. E., Girvin, S. M., Schoelkopf, R. J. & Glazman, L. I. Decoherence of superconducting qubits caused by quasiparticle tunneling. *Physical Review B - Condensed Matter and Materials Physics* **86**, 1–17 (2012).

[118] WRspice is part of the free open-source XicTools software package for integrated circuit design from Whiteley Research Inc, available at http://wrcad.com.

[119] Kalashnikov, K. *et al.* Bifluxon: Fluxon-Parity-Protected Superconducting Qubit. *PRX Quantum* **1**, 1 (2020).

[120] Martinis, J. Saving superconducting quantum processors from decay and correlated errors generated by gamma and cosmic rays. *npj Quantum Information* **7** (2021).

[121] Olaya, D. *et al.* Planarized Process for Single-Flux-Quantum Circuits with Self-Shunted Nb/NbxSi1-x/Nb Josephson Junctions. *IEEE Transactions on Applied Superconductivity* **29** (2019).

[122] Lucas, T. J. *et al.* Indium Bump Process for Low-Temperature Detectors and Readout. *Journal of Low Temperature Physics* 1–6 (2022).